National Library
of Canada

Canadian Theses Service

Ottawa, Canada
K1A 0N4

Bibliothèque nationale
du Canada

Services des thèses canadiennes

CANADIAN THESES

THÈSES CANADIENNES

NOTICE

The quality of this microfiche is heavily dependent upon the quality of the original thesis submitted for microfilming. Every effort has been made to ensure the highest quality of reproduction possible.

If pages are missing, contact the university which granted the degree.

Some pages may have indistinct print especially if the original pages were typed with a poor typewriter ribbon or if the university sent us an inferior photocopy.

Previously copyrighted materials (journal articles, published tests, etc.) are not filmed.

Reproduction in full or in part of this film is governed by the Canadian Copyright Act, R.S.C. 1970, c. C-30.

AVIS

La qualité de cette microfiche dépend grandement de la qualité de la thèse soumise au microfilmage. Nous avons tout fait pour assurer une qualité supérieure de reproduction.

S'il manque des pages, veuillez communiquer avec l'université qui a conféré le grade.

La qualité d'impression de certaines pages peut laisser à désirer, surtout si les pages originales ont été dactylographiées à l'aide d'un ruban usé ou si l'université nous a fait parvenir une photocopie de qualité inférieure.

Les documents qui font déjà l'objet d'un droit d'auteur (articles de revue, examens publiés, etc.) ne sont pas microfilmés.

La reproduction, même partielle, de ce microfilm est soumise à la Loi canadienne sur le droit d'auteur, SRC 1970, c. C-30.

THIS DISSERTATION
HAS BEEN MICROFILMED
EXACTLY AS RECEIVED

LA THÈSE A ÉTÉ
MICROFILMÉE TELLE QUE
NOUS L'AVONS REÇUE

Canada

NL-339 (r.86/06)

THE UNIVERSITY OF ALBERTA

TIME RESOLVED HIGH PRESSURE CHEMICAL IONIZATION MASS SPECTROMETRY WITH A DIRECT INSERTION PROBE

by

MICHAEL GEORGE IKONOMOU

A THESIS SUBMITTED TO
THE FACULTY OF GRADUATE STUDIES AND RESEARCH
IN PARTIAL FULFILMENT OF THE REQUIREMENTS FOR THE
DEGREE OF MASTER OF SCIENCE

DEPARTMENT OF CHEMISTRY

EDMONTON, ALBERTA
SPRING 1987

Permission has been granted to the National Library of Canada to microfilm this thesis and to lend or sell copies of the film.

The author (copyright owner) has reserved other publication rights, and neither the thesis nor extensive extracts from it may be printed or otherwise reproduced without his/her written permission.

L'autorisation a été accordée à la Bibliothèque nationale du Canada de microfilmer cette thèse et de prêter ou de vendre des exemplaires du film.

L'auteur (titulaire du droit d'auteur) se réserve les autres droits de publication; ni la thèse ni de longs extraits de celle-ci ne doivent être imprimés ou autrement reproduits sans son autorisation écrite.

ISBN 0-315-37758-5

THE UNIVERSITY OF ALBERTA

RELEASE FORM

NAME OF AUTHOR MICHAEL GEORGE IKONOMOU

TITLE OF THESIS TIME RESOLVED HIGH PRESSURE CHEMICAL IONIZATION MASS SPECTROMETRY WITH A DIRECT INSERTION PROBE

DEGREE FOR WHICH THESIS WAS PRESENTED M.Sc.

YEAR THIS DEGREE WAS GRANTED 1987

Permission is hereby granted to THE UNIVERSITY OF ALBERTA LIBRARY to reproduce single copies of this thesis and to lend or sell such copies for private, scholarly, or scientific purposes only.

The author reserves other publication rights, and neither the thesis nor extensive extracts from it may be printed or otherwise reproduced without the author's written permission.

MIkonomou

(Signed)

PROFITOU ILIA 18
ERYTHRES, ATTIKIS
GREECE

DATE: October 28, 1986

THE UNIVERSITY OF ALBERTA

FACULTY OF GRADUATE STUDIES AND RESEARCH

The undersigned certify that they have read, and recommended to the Faculty of Graduate Studies and Research, for acceptance, a thesis entitled TIME RESOLVED HIGH PRESSURE CHEMICAL IONIZATION MASS SPECTROMETRY WITH A DIRECT INSERTION PROBE submitted by MICHAEL GEORGE IKONOMOU in partial fulfilment of the requirements for the degree of MASTER OF SCIENCE.

P. Kebarle

P. KEBARLE, SUPERVISOR

Frederick F. Cantwell

F.F. CANTWELL

Byron Kratochvil

B. KRATOCHVIL

J. GRAY

DATE: October 28, 1986

This thesis is dedicated to Eleni (Nitsa) and Georgios, my parents, for their love, support, and encouragement throughout my student years.

ABSTRACT

A commercial mass spectrometer was modified for pulsed high pressure chemical ionization, PHPCI, studies. The mass spectrometer was fitted with a high pressure ion source, a pulsed electron gun, a chemical ionization direct insertion probe, CIDIP, and could be operated with ion source pressures up to 10 Torr. The pulsed high pressure mass spectrometer, PHPMS, provided time resolved ion analysis, i.e. the relative concentration of the ions in the HPCI source can be monitored as a function of time, which allows one to study the mechanisms involved in analytical chemical ionization. The long range aim of the present research was to explore and demonstrate the capabilities of the PHPMS technique for analytical CI work.

The performance of the HPCI source, fitted with a "new" electron gun design, was tested in the pulsing mode, by studying the water clustering equilibrium reaction, $(H_2O)_{n-1}H_3O^+ + H_2O \rightleftharpoons (H_2O)_nH_3O^+$, for n=2 to 4. The results obtained were in good agreement with those in the literature. Experiments were made to find the optimum operating conditions for the DIP and to estimate the analyte concentration in the ion source by utilizing thermodynamic and kinetic data. HPCI mass spectra for a number of low volatility amino acids and monosacharides were obtained employing the DIP. The performance of the DIP for time resolved studies was tested by studying the gas phase basicity of glycine. The results obtained were in good agreement with data in the literature.

The thermodynamic and kinetic parameters associated with the protonation of ferrocene in the gas phase, employing time resolved analysis, were investigated. The proton affinity of ferrocene was found to be 204.9 ± 2.0 kcal mol^{-1}. Exothermic proton transfer to ferrocene from ring protonated bases was found to be slow, whereas, oxygen protonated bases had higher rate constants. The analytical applications of these findings are discussed. It is argued that there is a relation between the exothermic slow protonation reactions (of compounds like ferrocene) and low sensitivity (for the same compounds) in atmospheric pressure chemical ionization, APCI.

ACKNOWLEDGEMENT

I would like to express my sincere gratitude to Professor P. Kebarle for his helpful advice and encouragement throughtout the duration of this work.

I wish to acknowledge the assistance and valuable discussions with my friend Dr. J. Sunner throughout the course of this study.

The author would like to thank the staff of the Chemistry Department Electronics and Machine Shop for their assistance in the design, construction, and maintenance of the apparatus.

Thanks are extended to Basiliki (Vicky) Protopappas for her much appreciated help in typing and drafting the manuscript.

The financial assistance provided by the University of Alberta and the National Research Council of Canada is acknowledged.

TABLE OF CONTENTS

CHAPTER PAGE

1 INTRODUCTION 1

1.1 CHEMICAL IONIZATION MASS SPECTROMETRY (CIMS) 1

1.2 METHANE AS REAGENT GAS IN POSITIVE CI 4

1.3 THE IMPORTANCE OF THERMODYNAMIC DATA IN ANALYTICAL CI 6

1.4 INSTRUMENTAL ASPECTS OF CIMS 8

1.5 THE PRESENT WORK 10

2 EXPERIMENTAL 13

2.1 REQUIREMENTS AND DESIGN OF THE PRESENT INSTRUMENT 13

2.2 OVERALL DESCRIPTION OF THE APPARATUS 14

A. THE EXISTING INSTRUMENT AND THE REQUIRED MODIFICATIONS 16

B. PUMPING SYSTEM ASSESSMENT UNDER HIGH PRESSURE CHEMICAL IONIZATION (HPCI) CONDITIONS 20

2.3 THE GAS HANDLING SYSTEM 22

2.4 THE CONVENTIONAL HPCI SOURCE 27

A. DESCRIPTION OF THE BASIC COMPONENTS 27

B. TEMPERATURE CONTROL AND MEASUREMENT 32

C. SAMPLE INTRODUCTION 33

2.5 THE HPCI SOURCE AND THE DIRECT INSERTION PROBE SAMPLE INTRODUCTION SYSTEM 37

A. DESCRIPTION OF THE BASIC COMPONENTS 39

B. THE DIRECT CI SAMPLE INTRODUCTION PROBE 48

C. SUPPRESSION OF DISCHARGES AT THE INTERFACE COMPONENT REGION 53

D. SUMMARY OF ROUTINE SOLID SAMPLE INTRODUCTION PROCEDURE 55

2.6 THE ELECTRON GUN ASSEMBLY 57

A. ARRANGEMENT OF ELECTRODES 57

B. PULSING OF THE ELECTRON BEAM 62

C. ELECTRON BEAM DEFLECTION DUE TO STRAY MAGNETIC FIELDS 64

2.7 ION ACCELERATION FROM THE ION SOURCE TO THE MASS ANALYZER 65

2.8 MASS ANALYSIS AND THE MASS READOUT SYSTEM 67

2.9 ION DETECTION AND DATA COLLECTION 74

2.10 SAMPLE IONIZATION UNDER PULSED HPCI CONDITIONS 77

2.11 TEMPORAL BEHAVIOR OF IONS AND TREATMENT OF DATA 79

A. TEMPORAL BEHAVIOR OF IONS 79

B. NORMALIZATION OF THE DATA 82

3 ASSESSMENT OF THE INSTRUMENT'S OPERATION 85

3.1 PHYSICAL CONDITIONS OF THE HPCI SOURCE 85

3.2 PERFORMANCE OF THE HPCI SOURCE WITH THE CONVENTIONAL SAMPLE INTRODUCTION SYSTEM UNDER PULSED ELECTRON BEAM ENVIRONMENTS 86

A. INTRODUCTION 86

B. EXPERIMENTAL 87

C. RESULTS AND DISCUSSION 89

3.3 PERFORMANCE OF THE DIRECT SOLID SAMPLE INTRODUCTION SYSTEM OPERATING IN LINE WITH THE HPCI SOURCE 94

A. HPCI MASS SPECTRA OF GLYCINE, LEUCINE, AND D-(+)-GALACTOSE 94

B. EVALUATION OF ANALYTE CONCENTRATION IN THE HPCI SOURCE USING THERMOCHEMICAL DATA. DIMERIZATION OF GLYCINE 100

C. EXPERIMENTAL DETERMINATIONS OF THE PROTON AFFINITY OF GLYCINE IN THE GAS PHASE. THE SIGNIFICANCE OF THE DUAL BULB GHS IN THE PRESENT STUDY............110

4 THERMODYNAMICS AND KINETICS ASSOCIATED WITH THE PROTONATION OF FERROCENE IN THE GAS PHASE..........117

4.1 INTRODUCTION..................................117

4.2 EXPERIMENTAL..................................120

4.3 EQUILIBRIUM MEASUREMENTS LEADING TO GAS PHASE BASICITY AND PROTON AFFINITY OF FERROCENE..................................123

A. TREATMENT OF EXPERIMENTAL DATA FOR EVALUATING K_{eq}, ΔG^o, ΔH^o, AND ΔS^o FOR THE PROTON TRANSFER REACTION: $BH^+ + (C_5H_5)_2Fe \rightleftharpoons (C_5H_5)_2FeH^+ + B$........128

B. FORMATION OF $(C_5H_5)_2Fe^+$ AND ITS EFFECT ON CHEMICAL EQUILIBRIUM MEASUREMENTS..............................134

C. COMPARISONS OF GAS PHASE BASICITIES AT DIFFERENT TEMPERATURES....................142

D. THE GAS PHASE BASICITY LADDER. EVALUATION OF THE GAS PHASE BASICITY AT 500 K, AND PROTON AFFINITY OF FERROCENE...146

4.3.1 DISCUSSION RELATED TO THE ENTROPY CHANGE UPON PROTONATION OF FERROCENE.................150

4.4 KINETICS AND RATE CONSTANTS ASSOCIATED WITH THE PROTONATION OF FERROCENE..................152

4.4.1 TREATMENT OF EXPERIMENTAL DATA FOR EVALUATING THE FORWARD RATE CONSTANT FOR THE REACTION:

$BH^+ + (C_5H_5)_2Fe \rightleftharpoons (C_5H_5)_2FeH^+ + B$...........154

A. METHOD I IRREVERSIBLE PROTON TRANSFER TO FERROCENE FROM REFERENCE BASE B..........154

B. METHOD II REVERSIBLE FIRST ORDER PROTON TRANSFER.....................................166

C. METHOD III REFERENCE BASE DIMERIZATION AND ITS EFFECT ON THE RATE CONSTANT FOR THE PROTONATION OF FERROCENE. ANALOG COMPUTER ANALYSIS OF EXPERIMENTAL DATA....170

D. METHOD IV EVALUATION OF k_F LEADING TO PROTONATION OF FERROCENE USING K_{eq} AND k_R 176

4.4.2 DISCUSSION OF RESULTS. THE KINETICS OF PROTON TRANSFER REACTIONS TO FERROCENE........177

LIST OF TABLES

PAGE

Table 2.1 Typical Operating Voltages for the Electron Gun Assembly.. 60

Table 2.2 Typical Operating Voltages for Ion Accelerating Electrodes.. 68

Table 3.1 Thermodynamic Data for Ion-Molecule Reactions of Glycine and Aniline.........................109

Table 4.1 Thermochemical Data Resulting from the Protonation of Ferrocene Equilibrium Measurements........135

Table 4.2 Literature and Adjusted GB Values for $C_6H_5COHCH_3$, C_4H_5N, DMF, and 3-ClPy.......................145

Table 4.3 Rate Constants for the Proton Transfer Reaction (Involving Different Bases, B): $BH^+ + (C_5H_5)_2Fe \rightleftharpoons (C_5H_5)_2FeH^+ + B$.......................155

LIST OF FIGURES

PAGE

Figure 2.1. Block Diagram of the Pulsed HPCI Mass Spectrometer........ 15

Figure 2.2. Cross Sectional View of the Mass Spectrometer........ 18

Figure 2.3. The Gas Handling System........ 24

Figure 2.4. HPCI Source with Electron Gun Assembly........ 28

Figure 2.5. Cross Sectional View of the Direct Insertion Probe Sample Introduction System Coupled to the CI Source Housing, and of the Chemical Ionization Sample Introduction Probe........ 40

Figure 2.6. Photographs of the Insertion Lock Components, HPCI Source Housing and Electron Gun Assembly........ 42

Figure 2.7. Cross Sectional View of the CI Direct Insertion Probe........ 49

Figure 2.8. Cross Sectional View of the Electron Gun Assembly........ 28

Figure 2.9. Cross Sectional View of the Ion Accelerating and Focussing Electrode........ 66

Figure 2.10. Diagram of the Hall Probe Mounting Arrangement and the Mass Readout System........ 72

Figure 2.11. Time Depenence of the Ion Intensities of $(H_2O)_nH_3O^+$ for n=2 to 4........ 80

Figure 3.1. Equilibrium Constants (K_{eq}) as a Function of Water Pressure at Different Source Temperatures for the Reaction:
$(H_2O)_2H_3O^+ + H_2O \rightleftharpoons (H_2O)_3H_3O^+$ 90

Figure 3.2. van't Hoff Plots for Reactions,
$(H_2O)_{n-1}H_3O^+ + H_2O \rightleftharpoons (H_2O)_nH_3O^+$ with n=1,2,3 91

Figure 3.3. Van't Hoff Plot Resulting from Least Squares Analysis of the Experimentally Obtained Data for the Clustering Equilibrium Reaction:
$(H_2O)_2H_3O^+ + H_2O \rightleftharpoons (H_2O)_3H_3O^+$ 93

Figure 3.4. (a) HPCI Mass Spectra of Glycine, (G), and Leucine, (L), with CH_4 being the Reagent Gas 95

Figure 3.5. Alterations in the HPCI Mass Spectrum of Glycine, (G), as a Function of T_p 97

Figure 3.6. HPCI Mass Spectrum of D-(+)-Galactose, (G), with a Methane/Toluene (T) Mixture being the Reagent Gas 98

Figure 3.7. HPCI Mass Spectrum of Glycine, (G), with a Methane/Toluene (T) Mixture being the Reagent Gas 102

Figure 3.8. Time Dependence of Ion Itensities of TH^+, GH^+, G_2H^+ Resulting from a Methane/Toluene/Glycine Gas Mixture 103

Figure 3.9. Equilibrium Constant K_{eq} for the Reaction: $GH^+ + G \rightleftharpoons G_2H^+$ as a Function of T_p 106

Figure 3.10. Van't Hoff Plot for the Clustering Equilibrium: $GH^+ + G \rightleftharpoons G_2H^+$ 108

Figure 3.11. HPCI Mass Spectrum of Glycine, (G), with a Methane/Aniline (A) Mixture being the Reagent Gas....................112

Figure 3.12. Plot of the Logarithmic Ion Intensities Versus Time After the Ionization Pulse in a Mixture of Methane/Analine/Glycine....................113

Figure 3.13. van't Hoff Plots for the Equilibrium Reactions: (a) $AH^+ + G \rightleftharpoons AGH^+$, (b) $AH^+ + A \rightleftharpoons A_2H^+$, and (c) $AH^+ + G \rightleftharpoons GH^+ + A$....................114

Figure 4.1. HPCI Mass Spectrum of a Methane/Acetophenone/Ferrocene Gas Mixture....................124

Figure 4.2. HPCI Mass Spectrum of a Methane/Pyrrole/Ferrocene Gas Mixture....................125

Figure 4.3. HPCI Mass Spectrum of a [illegible]thane/DMF/Ferrocene Gas Mixture....................126

Figure 4.4. HPCI Mass Spectrum of a Methane/Water/3-ClPy/Ferrocene Gas Mixture....................127

Figure 4.5. Time Dependence of Logarithmic and Normalized Ion Intensities with Achievement of Equilibrium from the Acetophenone/Ferrocene System....................129

Figure 4.6. Equilibrium Constant as a Function of Ferrocene Pressure at 500 K for the Acetophenone/Ferrocene System....................132

Figure 4.7. Equilibrium Constant K_{eq} as a Function of Ion Source Pressures at 490 and 550 K for the Acetophenone/Ferrocene System....................133

Figure 4.8. Equilibrium Constant K_{eq} as a Function of Ferrocene Pressure at 500 K for the DMF/Ferrocene System...136

Figure 4.9. van't Hoff Plots for the Proton Transfer Reactions (Involving Different Bases, B):
$BH^+ + (C_5H_5)_2Fe \rightleftharpoons (C_5H_5)_2FeH^+ + B$.......................137

Figure 4.10. Time Dependence of Ion Currents with Achievement of Equilibrium from the 3-ClPy/Ferrocene System...141

Figure 4.11. Gas-Phase Basicity Ladder Based on Measurements of Equilibrium Constants K for Equilibria (Involving Different Bases,B):
$BH^+ + (C_5H_5)_2Fe \rightleftharpoons (C_5H_5)_2FeH^+ + B$, at 500 K..............148

Figure 4.12. Time Dependence of the Normalized Ion Intensities Resulting from the Benzene/Ferrocene System. Data from Four Different Experiments............157

Figure 4.13. Logarithmic Plot of Normalized Ion Intensity of Protonated Benzene Versus Time for the Four Differect experiments shown in Figure 4.19..........161

Figure 4.14. Plots of Reaction Frequency ν_F Versus Ferrocene Pressure Resulting from the Reaction (Involving Different Bases,B):
$BH^+ + (C_5H_5)_2Fe \longrightarrow (C_5H_5)_2FeH^+ + B$........................162

Figure 4.15. Plot of ν_F vs. Ferrocene Pressure Resulting from the Reaction (Involving Different Bases, B):
$BH^+ + (C_5H_5)_2Fe \longrightarrow (C_5H_5)_2FeH^+ + B$........................163

Figure 4.16. Arrhenius-Type Plots Illustrating the Temperature Dependence of K_F Associated with the Proton Transfer Reaction (Involving Different Bases, B): $BH^+ + (C_5H_5)_2Fe \longrightarrow (C_5H_5)_2FeH^+ + B$ 165

Figure 4.17. Time Dependence of Ion Currents with Rather Slow Achievement of Equilibrium from the Acetophenone/Ferrocene System 167

Figure 4.18. Logarithmic Plot of Normalized Ion Intensities of $(I^t(BH^+)-I^e(BH^+))$ vs. Time for the Data Presented in Figure 4.17 169

Figure 4.19. Time Dependence of Normalized Ion Intensities Resulting from the Acetone/Ferrocene System 172

Figure 4.20. Time Dependence of Normalized Ion Intensities Resulting from an Analog Computer Analysis of the Data in Figure 4.19 173

Figure 4.21. Rate Constants of Reactions (Involving Different Bases, B): $BH^+ + (C_5H_5)_2Fe \longrightarrow (C_5H_5)_2FeH^+ + B$, Plotted Against the Difference of Gas Phase Basicity, GB, Between Ferrocene and Reference Base B, at 500 K 178

Figure 4.22. Reaction Coordinate Diagram 181

LIST OF ABBREVIATIONS

PHPMS	Pulsed High Pressure Mass Spectrometer
PHPCI	Pulsed High Pressure Chemical Ionization
APCI	Atmospheric Pressure Chemical Ionization
CIMS	Chemical Ionization Mass Spectrometry
CIDIP	Chemical Ionization Direct Insertion Probe
DIP	Direct Insertion Probe
CI	Chemical Ionization
EI	Electron Impact Ionization
FI	Field Ionization/Desorption
PI	Photonionization
FA	Flowing Afterglow
ICRMS	Ion Cyclotron Resonance Mass Spectrometry
FT-ICR	Fourier Transform Ion Cyclotron Resonance
NRC	National Research Corporation
GHS	Gas Handling System
amu	Atomic Mass Units
CEM	Channeltron Electron Multiplier
GB	Gas Phase Basicity
PA	Proton Affinity
DMF	Dimethylformamide
3-ClPy	Trichloropyridine
HMB	Hexamethylbenzene
BEN	Benzene
TOL	Toluene
XYL	Xylene
ANI	Anisole

ppt	Parts per trillion
o.d.	Outside diameter
i.d.	Inside diameter
CPS	Counts per second
T_{IS}	Ion source temperature
Tp	Probe temperature
P_{IS}	Ion source pressure

CHAPTER 1

INTRODUCTION

1.1 Chemical Ionization Mass Spectrometry (CIMS).

The chemical ionization technique was introduced with a number of papers by Munson and Field (1-8) beginning in 1966. Since its initial introduction, CIMS has developed into a powerful and versatile tool for the mass spectrometric identification and quantitation of organic molecules and, consequently, has found extensive application in many branches of chemistry and biochemistry, and in the medical and environmental fields.

In chemical ionization the method of ion production is different from that used in electron impact ionization (EI), field ionization/desorption (FI), or photonionization (PI) mass spectrometry, and the decomposing species and consequent CI mass spectra are very different from the spectra produced by the other techniques. Chemical ionization, as the name implies, uses ion-molecule chemistry to ionize the compounds of interest rather than the direct primary ionization used in EI, FI, and PI mass spectrometry.

The basic CI technique requires a large amount of reagent gas and small amount of the sample to be analyzed. The pressure of reagent gas in the ion source is of the order of 0.5 to 1.0 Torr, while that of the analyte is of the order 10^{-3} to 10^{-5} Torr. Because of the very large excess of the reagent gas, ions from the reagent gas are essentially the only ones produced by electron impact ionization. The subsequent reactions of these ions with analyte molecules produce the CI spectra of the analyte samples. The most typical chemical ionization reactions are proton transfer, 1.1, charge transfer, 1.2, and adduct formation, 1.3 (9).

$$BH^+ + M \rightleftharpoons B + MH^+ \qquad 1.1$$

$$B^+ + M \rightleftharpoons B + M^+ \qquad 1.2$$

$$B^+ + M \rightleftharpoons (BM)^+ \qquad 1.3$$

The reagent ions (BH^+ and B^+ in examples 1.1-1.3) are the results of electron impact ionization and subsequent ion-molecule reactions of the reagent gas while M is the analyte.

The sensitivity of the CI technique usually is at least as high as the direct electron impact ionization (9,10) in the absence of a reagent gas. The ion current produced in CI, and hence, the sensitivity of the method is directly dependent on the rate constants k for the chemical ionization reactions. Many ion-molecule reactions used as chemical ionization reactions are highly efficient and have rate constants in the range of 1 to 4×10^{-9} cm^3 $molec.^{-1} sec^{-1}$ (9). However, inefficient ionization reactions with small rate constants also occur. Such low rate constants will lead to lower sensitivities for the analyte detection. In particular, endothermic ionization reactions will have an activation energy at least equal to exothermicity and will be correspondingly inefficient.

In CI mass spectra, in contrast to EI, there is generally considerably less fragmentation and this is attributed to the lower excitation imparted to the analyte ions by the chemical ionization reactions e.g. reactions 1.1 to 1.3. An additional factor is the relatively high reagent gas pressure, which assis~~ts in~~ the thermalization of the chemical ionization reaction products (11). The advantage of having nearly all the ionization products concentrated in one or a few peaks can be very significant in trace analysis. With electron impact, some classes of compounds lead to a very low intensity molecular ion peak, which may be lost in the noise.

The ionization efficiency of the analyte molecules in CI sources increases with an increase in the source pressure. This is because the residence time of the reagent and analyte ions in the ion source is much longer at high pressures.. However, extracting the ions from a high pressure source is not a trivial task. Ion extraction efficiency usually decreases with increasing source pressure. Nevertheless, when the high ionization efficiency of the CI technique is coupled with an efficient procedure for ion extraction, the detectibility of the technique increases by about two orders of magnitude over EI mass spectrometry. This detectability enhancement is even greater when the pressure of the ion source of the mass spectrometer is raised to atmospheric pressure (atmospheric pressure chemical ionization, APCI). It is this technique which enables detection of trace compounds at parts per trillion (ppt) by volume.

The versatility and the usefulness of the CI technique is basically attributed to the large variety of reagent gases and, consequently, reagent ions that can be used to effect ionization. With proper selection of reagent gas information about the molecular weight, structure, and quantitation of the analyte molecule can be obtained. Modern reviews on the CI technique and its capabilities can be found in references (9, 12-16).

1.2 Methane as a Reagent Gas in Positive CI.

The most common reagent gas for CI studies has been methane because it was the first reagent gas tried (1), and because it generally gives information about molecular weight and molecular structure from $(M+1)^+$ and fragment ions.

The principal primary ions created by electron impact with methane, in the positive ion mode, are $CH_4^{+\cdot}$, CH_3^+, and $CH_2^{+\cdot}$. $CH_4^{+\cdot}$ and CH_3^+ are by far the most abundant of these ions. They are formed with an approximate ratio of 55:45, and constitute about 90% of the total ionization.

These ions, at the relativity high methane pressure used, react rapidly with methane via reactions 1.4 to 1.8.

$$CH_4^{+\cdot} + CH_4 \longrightarrow CH_5^{+} + CH_3^{\cdot} \qquad 1.4$$

$$CH_3^{+} + CH_4 \longrightarrow C_2H_5^{+} + H_2 \qquad 1.5$$

$$CH_2^{+\cdot} + CH_4 \longrightarrow C_2H_4^{+\cdot} + H_2 \qquad 1.6$$

$$\longrightarrow C_2H_3^{+} + H_2 + H^{\cdot} \qquad 1.7$$

$$C_2H_3^{+} + CH_4 \longrightarrow C_3H_5^{+} + H_2 \qquad 1.8$$

At 1 Torr ion source pressure the relative abundance of the major ions are CH_5^{+} (48%), $C_2H_5^{+}$ (41%), and $C_3H_5^{+}$ (6%), (17). There are also minor yields of $C_2H_4^{+}$ and $C_3H_7^{+}$. The highest abundance ions, CH_5^{+} and $C_2H_5^{+}$, do not react further with methane, and represent the major reagent ions in methane positive CIMS. Both can act as protonating agents as illustrated by reactions 1.9 and 1.10.

$$CH_5^{+} + M \rightleftharpoons CH_4 + MH^{+} \qquad 1.9$$

$$C_2H_5^{+} + M \rightleftharpoons C_2H_4 + MH^{+} \qquad 1.10$$

In addition to these reactions, $C_2H_5^{+}$ can engage in hydride abstraction reaction, 1.11, with suitable analytes, or adduct formation, 1.12.

$$C_2H_5^{+} + M \rightleftharpoons C_2H_6 + (M-H)^{+} \qquad 1.11$$

$$C_2H_5^{+} + M \rightleftharpoons (C_2H_5.M)^{+} \qquad 1.12$$

The CI technique, being based on ion-molecule i.e. chemical reactions, relies on an understanding of ion-molecule chemistry. Thus, for proton transfer 1.1 to occur at an observable rate the proton affinity of the analyte M, PA(M), must be larger than that of B, i.e. PA(M) > PA(B), so that reaction 1.1 is exothermic. Similarly, the hydride abstraction 1.11 will occur only if the hydride of $C_2H_5^+$ is higher in PA than that of $(M-H)^+$, and very stable adduct formation 1.12 will occur if M is an unsaturated compound so that a bond, as illustrated for M=propylene, in equation 1.13, is formed.

$$C_2H_5^+ + C_3H_6 \rightleftharpoons CH_3\text{-}CH_2\text{-}CH_2\text{-}C^+H\text{-}CH_3 \qquad 1.13$$

1.3 The Importance of Thermochemical Data in Analytical CI.

Systematic studies on ion-molecule reactions started in the early fifties by Stevenson and Schissler (18,19), Tal'rose and Lyubimova (20), and Field, Franklin, and Lampe (21,22). Since then a number of researchers have been involved in the area and the study of the products, distribution, rates, and equilibria of gas-phase ionic reactions has become a major field of scientific activity with application in many diverse fields. The large body of kinetic and thermodynamic data derived from the fundamental studies constitutes the foundation upon which the chemistry of the chemical ionization technique is based.

The usefulness of an ion-molecule reaction in a chemical ionization system depends, in part, on the identity of the reaction products, and, in part, on the rate of the reaction. Studies of the effects of temperature and pressure on ion-molecule reaction rates (11) have provided valuable information for analytical CI work. For instance, the relative yield of fragment versus quasi-molecular ions (MH^+) has shown strong dependence on ion source temperature (7). Also, the nature of the chemical ionization reagent can also be affected by the ion source temperature : For example, low temperature will increase the rate of formation of cluster ions $(H_2O)_nH^+$ and $(NH_3)_nH^+$ in water and ammonia CIMS, respectively. Cluster ions will, in turn, be more moderate proton transfer reagents than the corresponding monomeric ions.

Measurements of proton transfer equilibria in the gas phase have yielded an extensive compilation of gas basicity and proton affinity data (23), which have found direct applications in analytical mass spectrometry. These data, apart from making it possible to separate and identify the intrinsic structural effects and the solvent effects on the acid base properties of the molecules, are also very valuable in understanding the mechanism of protonation of molecules in the gas phase, particularly in CI where proper selection of reagent molecules has direct influence on the specificity and sensitivity of the technique.

1.4 Instrumental Aspects of CIMS.

Most of the chemical ionization studies have been carried out in ion sources capable of operating within the pressure range 0.5-2.0 Torr and with the reagent gas present in at least one-thousandfold excess. With most instruments, the ion source is only slightly modified from the EI arrangement. Thus, ionization under EI and/or CI conditions can be obtained. However, in such sources, diffusional loss of ions to the walls and removal of ions from the source by necessary extraction fields, limits the ion source residence time to no more than approximately 10 μsec (9). Residence time of an ion in the ion source is an important parameter in studying the various ion-molecule processes that occur in CI.

Much of the basic ion-molecule chemistry required for a good understanding of the reactions occurring in analytical CI was developed with use of more specialized mass spectrometric apparatus, since the routine analytical CI instruments are not well suited for such work.

With removal of the repeller voltage from the ion source of the analytical CI instrument, one obtains field free conditions, where the energies of the ions depend solely on the temperature of the ion source. If the reactant ions are not excited when they enter into reactive collision with neutrals, the reactions are truly thermal. Also, by increasing the pressure in the ion source, the residence time of ions is much longer because the diffusion of ions to the wall is slowed down by an increased number of collisions with neutral molecules. The rate of ion-molecule reactions is also faster because of the increase in concentration of the reacting neutrals. With sufficiently high pressure and long ion retention time in the ion source, it is possible to observe the thermal equilibrium for certain ion-molecule reactions and to determine the thermal equilibrium constants. Determinations of rate constants for ion molecule reactions, of proton affinities, hydride affinities, etc. of various compounds, adduct stabilities, etc. have been obtained mostly with four different techniques: Pulsed electron high pressure mass spectrometry, PHPMS (24), flowing afterglow, FA (25,26), pulsed ion cyclotron resonance, ICRMS (27), and Fourier transform ICR, FT-ICR (28). The pulsed electron high pressure technique was developed by Kebarle and co-workers (29-31). Similar apparatus was also used, later, by Field and co-workers (32), Meot-Ner (33), and others (34).

None of the four techniques has been used for determinations of low volatility organic compounds. Yet, basic data involving such compounds are required, not only for analytical CI work but also in other areas of chemistry. Work with low volatility compounds is difficult since heating of the apparatus and special sample introduction techniques are required in order to obtain a sufficient pressure of the analyte in the mass spectrometer ion source. In routine CI analytical work a number of techniques (35-44) have been proposed for the introduction of low volatility and thermally labile analytes. With all techniques, nonvolatile or low volatility samples are introduced into the ion source of the mass spectrometer, via a direct insertion probe, DIP. The DIP is basically a long rod with a small cavity at its tip, or with a direct exposure tip. The solid sample is placed in the cavity or coated at the flat surface tip, and then the probe is inserted through a vacuum lock into the vacuum housing of the mass spectrometer. The DIP is pushed in until it reaches a port into the ionization chamber. Then the sample is heated so that vapours of the sample enter the ion source.

A DIP had not been used in PHPMS measurements and one of the major purposes of the present research was to develop such a DIP and demonstrate, if possible, its utility for basic measurements involving nonvolatile compounds. The special requirements that must be met in the design of the DIP for the PHPMS apparatus are described in a later section (Chapter 2, section 2.5).

1.5 The Present Work.

The PHPMS provides time resolved ion analysis, i.e. the relative concentration of the ion in the high pressure ion source can be observed as a function of time, after ionization has been obtained with a short electron pulse. The ability to obtain time resolved mass spectra is a decisive feature of the method, since it permits measurements of ion-molecule reaction kinetics, and measurement of ion-molecule reaction equilibria. While time resolved mass analysis has proven its ability to provide basic data, the method might also have direct analytical CI utility. The use of PHPMS as an analytical technique has not been explored and it was thought that such apparatus, when equipped with a direct insertion probe, might also be useful for the exploration and eventual demonstration of the capabilities of the PHPMS technique for analytical work. This was the second long range aim of the present research.

The material in the thesis is organized as follows. The experimental part (Chapter 2) deals with the rebuilding of a mass spectrometer to acquire pulsed electron high pressure operation and the design construction and adaptation of a direct insertion probe to this instrument. This Chapter, intentionally, gives a detailed account, since it is expected that research with the created instrumentation would be continued by future graduate students and these will profit from the detailed descriptions. The performance of the equipment is described and assessed in Chapter 3. Chapter 3 also describes an analytical application of the DIP on the PHPMS. Examined are the HPCI spectra of glycine, leucine, and D-(+)-galactose. Amino acids and sugars are quite involatile and CI spectra can be obtained only with a DIP.

An actual research project is outlined in Chapter 4. This work deals with the kinetics of proton transfer to ferrocene and the exact proton affinity of ferrocene. The findings have bearing not only for the CI analysis of ferrocenes, cobaltocenes, and nickelocenes but also to general gas phase ion-molecule kinetics and gas phase basicity orders.

CHAPTER 2

EXPERIMENTAL

2.1 Requirements and Design of the Present Instrument

This instrument was designed with a number of requirements in mind. One of these was a thermostatically controlled chemical ionization ion source that could operate at high and accurately known pressure. The source was to operate with reagent gas pressures in the order of 1 to 15 Torr and sample pressures of the order of 10^{-3} to 10^{-4} Torr. Since the ion source was to operate at such high pressures, a high capacity differential pumping system had to be constructed to handle the large flow rates of reagent gas from the ion source. High capacity pumping was necessary: first, not to degrade the performance of the mass analyzer and second, to ensure that ions diffusing out of the ion source will not undergo further collisions with neutrals prior to mass analysis and detection. The vacuum outside the ion source had to be at least 10^{-4} Torr so that the mean free path of an ion is much longer than the distance between the ion source and the detector.

As a source of ionization a high energy electron beam was to be used, energetic enough to penetrate the gaseous sample in the high pressure chemical ionization ion source (HPCIS) and effect primary ionization. Pulsing of the electron beam was also desired, to enable a study of the reactive changes of the ions as a function of time. The electron gun was to operate in both pulsing and continual ionization modes. Finally, a solid sample inlet system with a vacuum lock directly coupled to the HPCIS was to be constructed so that it would allow direct introduction of analytes of low volatility into the HPCIS. The inlet system including a solid sample CI probe, was to be differentially pumped prior to sample introduction in order to meet the pressure conditions of the HPCIS.

2.2 Overall Description of the Apparatus

The hardware of a high pressure mass spectrometer can be thought of as consisting of four major components: the electron gun which generates high energy electrons; the ion source in which ion molecule reactions take place; the mass analyzer where ions are separated according to their mass to charge ratio and the detection system where the intensity of each ion beam is measured quantitatively. All four components are enclosed in a vacuum chamber. A block diagram of the components mentioned above plus other electronic and sampling parts of the pulsed high pressure mass spectrometer used, is shown in Figure 2.1.

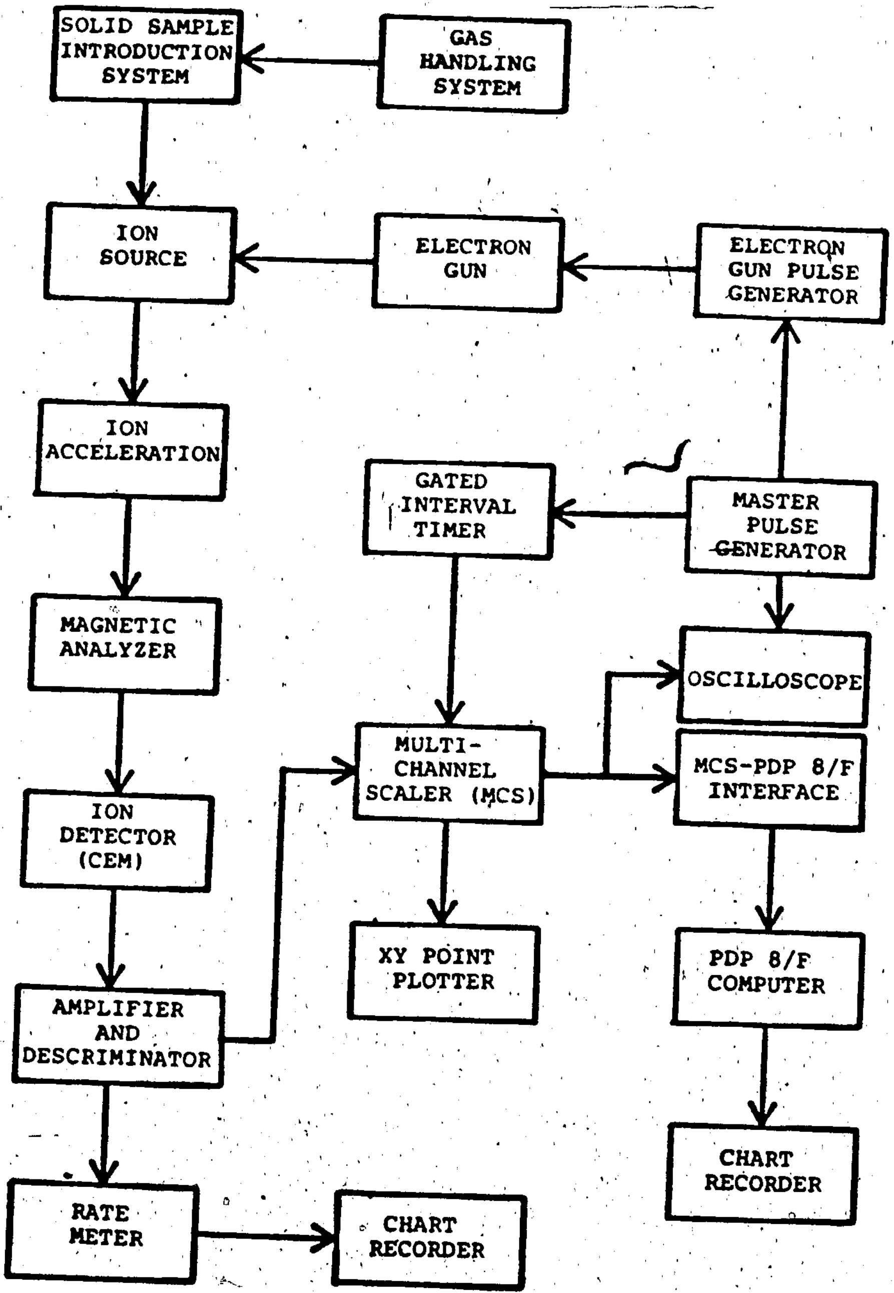
SOLID SAMPLE INTRODUCTION SYSTEM
GAS HANDLING SYSTEM
ION SOURCE
ELECTRON GUN
ELECTRON GUN PULSE GENERATOR
ION ACCELERATION
GATED INTERVAL TIMER
MASTER PULSE GENERATOR
MAGNETIC ANALYZER
OSCILLOSCOPE
MULTI-CHANNEL SCALER (MCS)
MCS-PDP 8/F INTERFACE
ION DETECTOR (CEM)
XY POINT PLOTTER
PDP 8/F COMPUTER
AMPLIFIER AND DESCRIMINATOR
CHART RECORDER
RATE METER
CHART RECORDER

Figure 2.1. Block Diagram of the Pulsed HPCI Mass Spectrometer.

A. The Existing Instrument and the Required Modifications

A commercial ATLAS MAT CH4 mass spectrometer was available as the basic piece of instrumentation. The CH4 is a conventional 60^{o}, 20 cm radius sector magnetic deflection mass spectrometer. This instrument had been modified from its original electron impact ionization arrangement by Kebarle _et_. _al_.(45) for flash photolysis studies . The modification involved a larger main vacuum chamber and additional high capacity pumping system to tolerate the large flow rates of gases outside the ion source. The high capacity pumping system consisted of a 2400 $L*sec^{-1}$ 6 inch oil vapour diffusion pump (National Research Corporation HS6-0162) fitted with a 6 inch NRC water cooled baffle, and two 80 $L*sec^{-1}$ 2 inch mercury vapour diffusion pumps (Speedivac 2M3B) one to pump the analyzer and detection section and the other for additional pumping of the main vacuum chamber. Kebarle _et_. _al_. (45) estimated the pumping speed of the above arrangement to be 500 $L*sec^{-1}$ at the ion source.

This pumping system, as described later in this Chapter (section 2.3), was found to give adequate pumping speed to tolerate the large flow rates of the reagent gases diffusing out of the high pressure chemical ionization ion source. The two minor improvements performed to this system were: first, the charge fluid of the two mercury Speedivac pumps were replaced by polyphenyl ether oil (Speedivac 5) and second, all three diffusion pumps were now roughed by a 375 L*min^{-1} mechanical forepump (Welch Duo-Seal Pump #1397) for better system performance. This high capacity roughing showed improvement in pressures, as read on the analyzer and ion source gauges, during normal operation. The major modifications performed on this instrument for the present study were those of the ion source, electron gun, sample introduction system, mass readout system, and the detector. Also, electron pulsing circuits and other electronic components (apart from what was available from the main frame of the ATLAS MAT CH4 spectrometer) were provided.

A schematic diagram of the mass spectrometer as it appeared in its final stage is shown in Figure 2.2. The basic components of this instrument were designed by the author and machined by the Chemistry Department machine shop at the University of Alberta. All the individual components of this apparatus are discussed in following sections of this Chapter.

Briefly, the overall functions of the assemblies shown in Figure 2.2 are as follows. After a suitable gas mixture is introduced to the ion source, [9], via the insertion lock assembly, [10], ionization is achieved by irradiating the mixture with a collimated beam of electrons emitted from a hot filament, [6]. Some of the resulting ions diffuse toward the small ion exit slit and escape to the evacuated region, [1]. They are then accelerated by an electric

Figure 2,2. Cross sectional View of the Mass Spectrometer.

1. Main vacuum chamber
2. HPCI source supporting flange
3. Vacuum chamber port leading to 6" oil diffusion pump
4. Vacuum chamber port leading to analyzer diffusion pump
5. Ionization gauge
6. Filament
7. Electron accelerating and focusing electrodes
8. Magnetic field shielding cylinder
9. HPCI source assembly
10. Insertion lock assembly for sample introduction
11. Electrostatic shield
12. Ion accelerating and focusing electrodes
13. ATLAS MAT CH4 analyzer tube and magnet
14. Secondary ion focusing electrodes
15. Channeltron electron multiplier

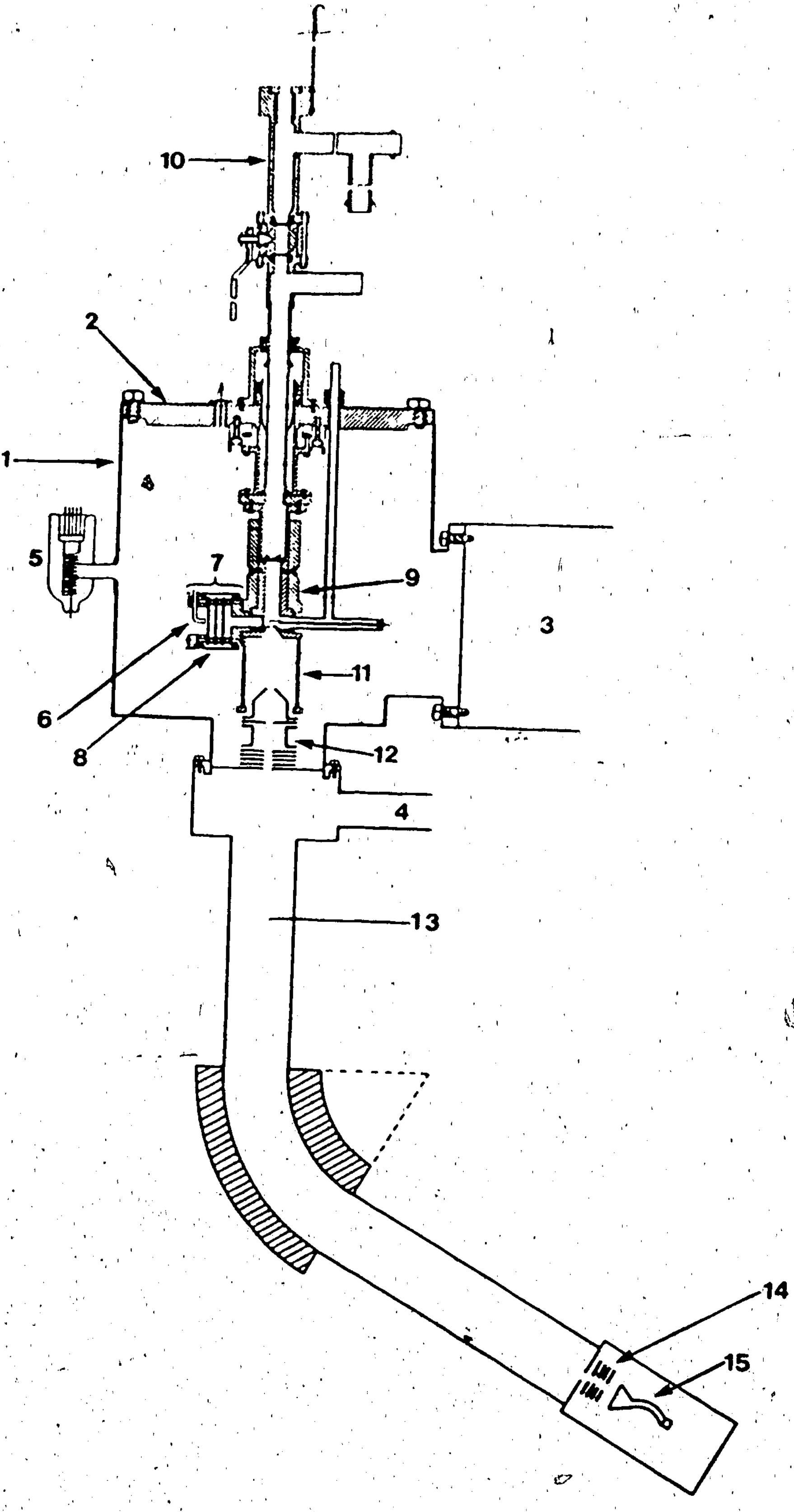

field, induced by the ion acceleration electrodes [12], to the mass analyzing region, [13], and mass analyzed. The mass analyzed ion beam is then further collimated by a second set of electrodes, [14], prior to striking the detector, [15]. The system is constantly pumped during normal operation, via ports [3] and [4] and the pressure is monitored by an ionization gauge, [5].

B. Pumping System Assessment Under HPCI Conditions

The only leakage of gas from the HPCI source to the main vacuum chamber is through the electron entrance and ion exit slits. These two apertures had to be very small for a number of reasons. First, to ensure that the HPCI source can retain a pressure of several Torr while the pressure in the external vacuum chamber is kept at minimum. Second, the pressure in the main vacuum chamber had to be maintained at minimum to reduce the possibility of ions, which escape from the HPCI source, colliding with neutrals on their path to mass analysis. Third, the flow from the HPCI source to the main vacuum chamber was to be kept at the molecular level for a specific set of slits with the pumping speed of the system being 500 L*sec^{-1}. The importance of requiring molecular flow out of these orifices is discussed in detail in references (55, 68-71).

The conductance F_1 of an aperture under molecular flow conditions is given by equation 2.1 (see Dushman (46,p.91)),

$$F_1 = (1/4)\ \bar{v}*A \qquad (2.1)$$

where $\bar{v}$ is the average velocity of the molecules in cm*sec^{-1} and A is the cross-sectional area of the aperture in cm^2. The average velocity of the molecule can be calculated from equation 2.2, where M is the molecular weight of the

$$\bar{v} = (8*R*T/M*\pi) \qquad (2.2)$$

molecule, R is the ideal gas constant in ergs K^{-1} mole^{-1}, and T is the temperature in K. At 450 K, the average velocity of the CH_4 is 7.7x10^4 cmsec^{-1}. The two apertures on the HPCI source had areas of (0.012 mm x 1.5 mm) for the electron entrance slit and (0.015mm x 1.5mm) for the ion exit slit. Using equation 2.1, the combined calculated conductance of both leaks is 7.8 cm^{3}sec^{-1}. The experimental value of 8 cm^{3}sec^{-1} was obtained by measuring the time dependence of the pressure drop in a known volume reservoir when gas was bled from the reservoir to the ion source, while the system was pumped at its highest capacity. This indicates that the flow out of the ion source was essentially molecular.

The required pumping speed S at the ion source and for a source pressure of 4.0 Torr can be calculated by use of equation 2.3. Here, F_1 is the total conductance of the

$$F_1*P_s = P_{vc}*S \qquad (2.3)$$

leaks, P_s is the ion source pressure, P_{vc} is the expected pressure in the vacuum chamber (outside the ion source), and S is the pumping speed outside the ion source. With F_1 = 7.8 cm^3sec^{-1} and S = 500 $Lsec^{-1}$, and an ion source pressure of 4.0 Torr according to equation 2.3 a pressure of 7×10^{-5} Torr will result in the vacuum chamber. During normal operation, with 4.0 Torr of CH_4 passing through the ion source, the ion source gauge located close to the ion source registered about 1×10^{-4} Torr which is in close agreement with the above calculated value. Under these conditions a Penning gauge located at the top of the differentially pumped analyzer tube registered ca 3×10^{-5} Torr for 4 Torr ion source pressure. Pressures between 25 and 35 mTorr were indicated in the thermocouple gauge located on the tube unit at the top of the rotary pump, which was used for roughing all three diffusion pumps of the system. Ultimate vacuum in the apparatus, in the absence of the CI gas load was typically between 6×10^{-8} and 2×10^{-7} Torr, after overnight pumping, depending on the history of the system.

2.3 The Gas Handling System

Mixtures of gases and/or volatile liquids, which were used as CI reagents and/or analytes in the present work, were prepared in a specially designed handling system. With this thermostatically controlled system, the partial pressures of the reactant molecules were measured and controlled prior to mass analysis.

The gas handling system is shown in Figure 2.3. The construction materials were Pyrex glass and stainless steel valves. Seven Granville-Phillips ultra high vacuum all-metal valves with silver gasket seals were mounted to the framework of the plant. A glass manifold, two 5 L glass bulbs, gas inlet and outlet lines, and vacuum lines were connected to the valves through 14 mm o.d. Pyrex tubings. The entire system was surrounded by a box made of 1" thick hard asbestos material, Marinite 36A. The box was thermostatically controlled by four heaters (GE 1000 watt rod elements bent into suitable shapes) located at the bottom and on the sides of the box. The heaters were placed behind a metal sheet which acted as a shield to provide more uniform corrective heating and reduce the possibility of thermal decomposition of the sample by direct radiation from the heaters. The gas handling system was usually kept at a temperature of about 120°C but it could be heated up to 200°C to ensure complete vaporization of nonvolatile samples and also to bake out impurities with overnight pumping.

The gas handling system could be pumped by either of two pumping systems. A rough pump was used to remove large amounts of gas and pump the system down to 20 mTorr as measured by a Pirani type gauge and recorded on a Granville-Philips, model 275, analog read out controller. The "clean"

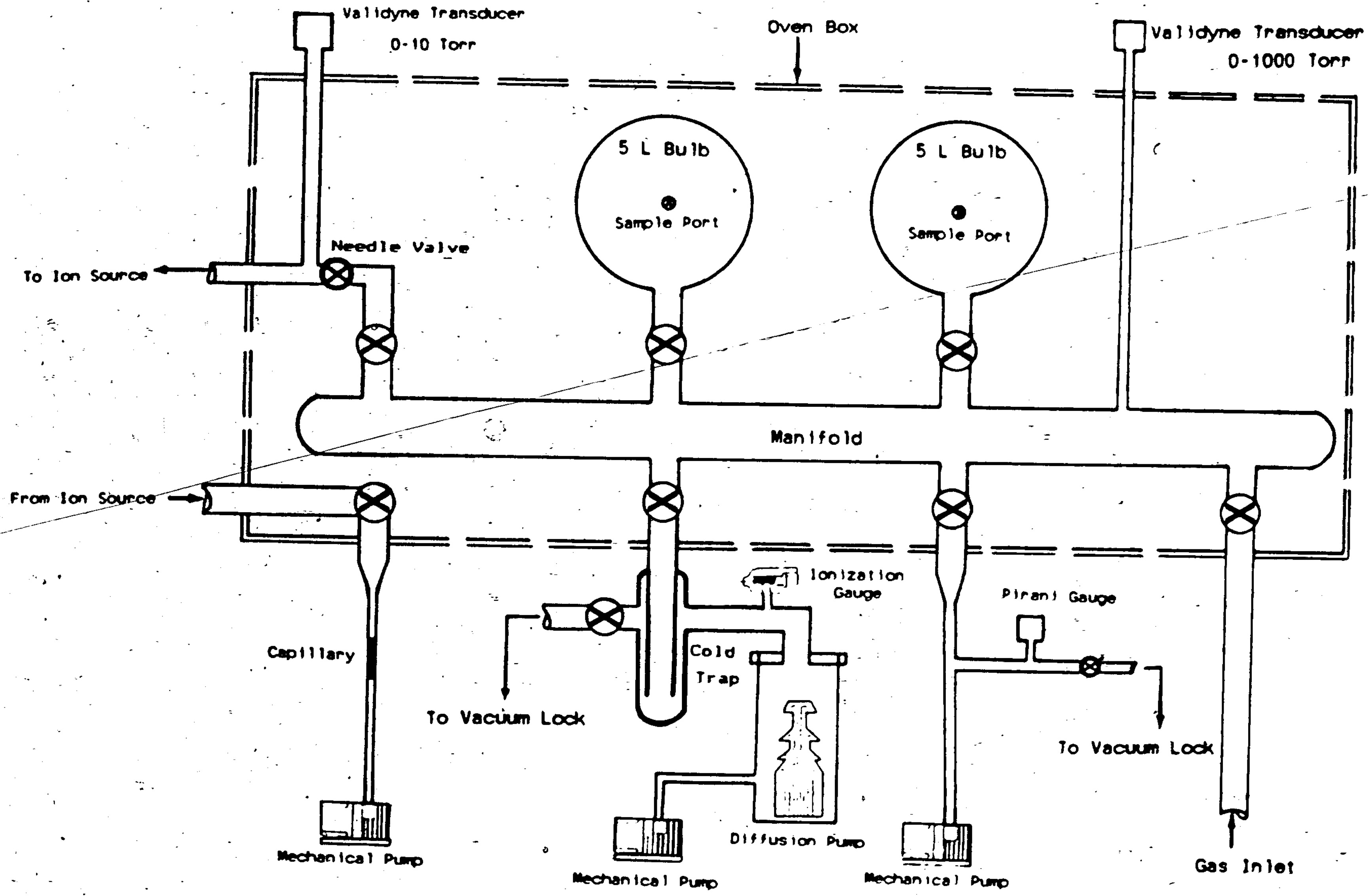
Validyne Transducer
0-10 Torr
Oven Box
Validyne Transducer
0-1000 Torr
5 L Bulb
Sample Port
5 L Bulb
Sample Port
Needle Valve
To Ion Source
Manifold
From Ion Source
Ionization Gauge
Pirani Gauge
Capillary
Cold Trap
To Vacuum Lock
To Vacuum Lock
Diffusion Pump
Mechanical Pump
Mechanical Pump
Mechanical Pump
Gas Inlet

Figure 2.3. The Gas Handling System (G.H.S.)

pump, which consisted of a liquid nitrogen cold trap coupled to an oil diffusion pump (Edwards # E-02) backed by a mechanical pump, was used to remove the last traces of gas.

Pressures as low as 8×10^{-7} Torr were recorded on a Veeco ionization gauge, located on top of the cold trap, after overnight pumping. Since the "clean" pump did not have to pass large quantities of gas, it had very low back streaming and thus the impurity levels in the system could be kept very low. This pumping arrangement served also the pumping requirements of the direct insertion probe sample introduction system , see section 2.5 of this Chapter.

The pressure in the system when gas mixtures were prepared was measured by a Validyne variable reluctance pressure transducer directly coupled to the manifold of the gas handling system. This transducer is constructed of a magnetically permeable stainless steel diaphragm designed with low volumetric diaphragm displacement for good dynamic range, high overload capacity (internal cavity walls provide effective overload stops), and high output signal with low susceptibility to electrical noise. A Validyne (model CD223) dual-channel digital transducer indicator was used to operate the Validyne variable reluctance transducer. This system could read pressures from 0.1 to 1000 Torr with an accuracy of 0.25% at full scale. Calibration of this system was checked periodically against 10^{-6} Torr pressure for the zero setting and against a mercury manometer for atmospheric pressure setting.

The 5 litre bulbs were used to prepare gas mixtures. Each bulb has an injection port consisting of two rubber septums separated by a dead space. The septa were changed frequently to prevent leakage and disintegration due to the elevated temperature. Access to the injection ports was obtained by a small sliding door located on the front and one of the sides of the box. Gaseous samples were introduced into the bulb through the gas inlet and the manifold while liquid samples (including volatile solids dissolved in an appropriate solvent) were introduced with a syringe through the injection port. These sample mixtures were allowed to mix thoroughly and were stored in the bulbs prior to introduction in the mass spectrometer. The requirement for the large 5 L reservoirs is essential so that the percentage of the sample used during a given series of measurements is small. Therefore one can assume that the sample conditions remain constant during analysis. The partial pressure of the analyte in the 5 L bulb, for the ammount injected, was calculated by using the ideal gas law equation.

During construction of the gas handling system one of the 5L bulbs was calibrated by weighing the amount of water it could hold. The volumes of the other parts of the system were estimated by monitoring the expansion of gas from the calibrated 5 L bulb. The calibration of this dual-bulb system was required so that the partial pressures of the gases in the mixture could be accurately known.

2.4 The Conventional HPCI Source

The design of the HPCI source was very similar to that used in other high pressure mass spectrometers in our laboratory (47) with the only difference being that of the position and design of the electron gun. On previous designs, the electron gun was mounted on a separate flange at right angles to the flange supporting the HPCI source. In order to avoid extra machining (extra flanges on the vacuum chamber) and also to test another possible version of electron gun design it was decided to mount the whole electron gun assembly directly to the side of the ion source. A schematic representation of the HPCI source, with the electron gun assembly attached to it, is shown in Figure 2.4. This conventional HPCI source arrangement was chosen initially so as to check the performance of the electron gun and all other functions of the mass spectrometer (ion focusing, ion separation, ion detection, and pumping). Major modifications were performed later on, on this source design in order to interface to it a specially designed solid sample inlet system.

A. Description of the Basic Components.

The HPCI source shown in Figure 2.4 was machined from a non-magnetic stainless steel tube 4 1/4 inch long with an inner diameter of one-half inch. One end of this tube was

Figure 2.4 HPCI Source with Electron Gun Assembly

1. Reaction zone of the HPCI source
2. The electron gun assembly
3. Electron entrance slit
4. Electron trap
5. Repeller
6. Ion exit slit
7. High conductance grid for electric field shielding
8. Cylindrical stainless steel support
9. Mica electrical insulator
10. Heating mantle
11. Base heaters
12. Heat shield
13. Gas sample inlet and outlet lines
14. Inlet and outlet line heater
15. Heat shield
16. Main vacuum chamber flange

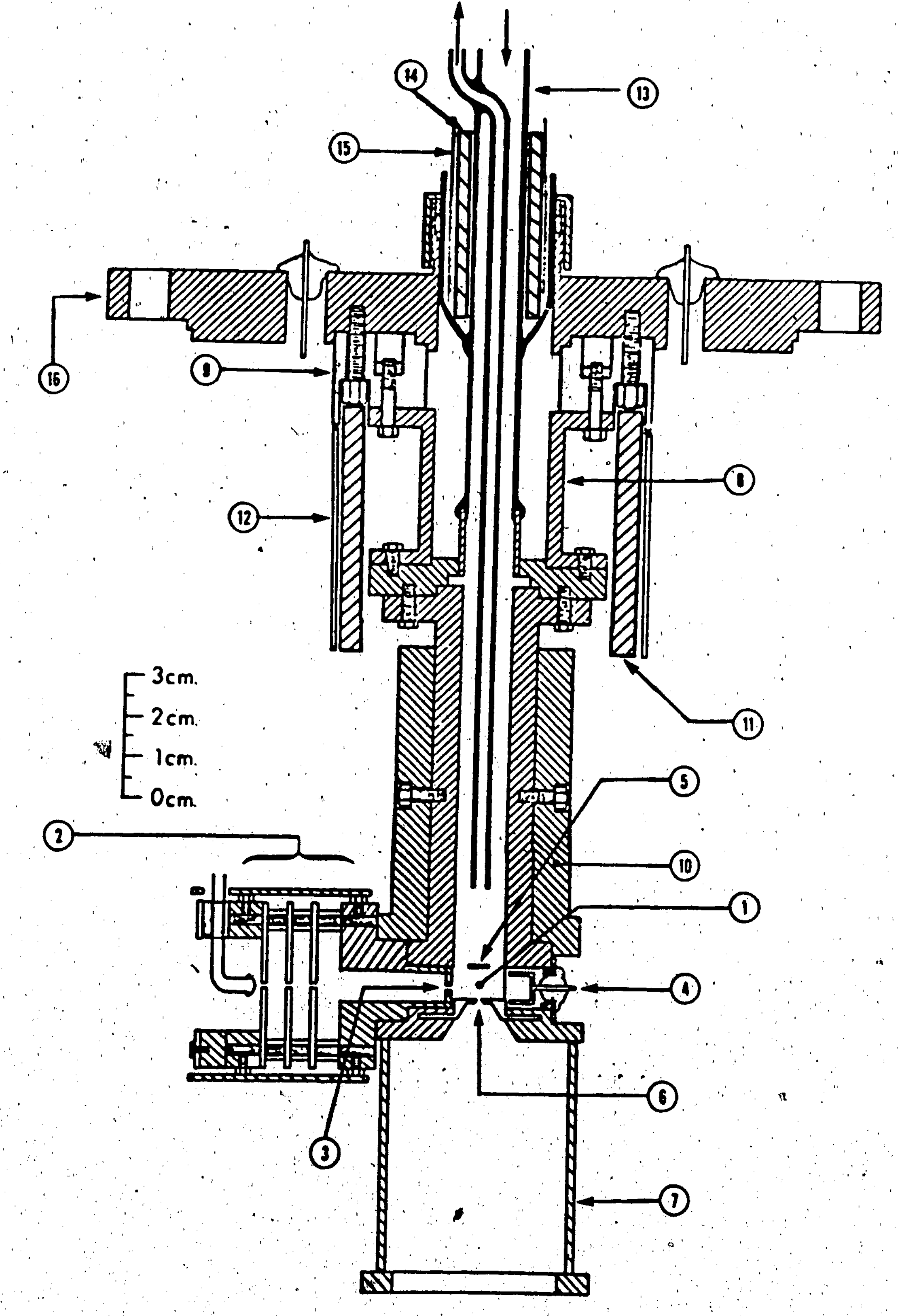

3cm.
2cm.
1cm.
0cm.

machined to couple to the base of the extension assembly mounted on the main flange. Three holes, were bored on the other end of the tube perpendicular to the main axis. The three holes which were at right angles to each other were sealed, by three small demountable flanges. A small "hat shaped" flange carried the electron entrance slit, [3], and also served as a support for the electron gun assembly. Opposite to this, was mounted the flange carrying the electron trap, [4], and at right angles to the trap was mounted the third flange supporting the repeller plate, [5]. The ions escaped through a slit, [6], which was supported by a cone shaped flange at the top of the HPCI source. The reaction zone, [1], where chemical ionization takes place is located at the top of the source and has a volume of about 2 cm^3. The plane of the electron beam was about 5 mm above the ion exit slit. Both electron entrance and ion exit slits were constructed by welding, under a microscope, two small pieces of stainless steel razor blades onto the hole at the top of the respective demountable slit flanges. All flanges were sealed with gold wire (0.015 inch thick) gaskets. Typical dimensions of the electron entrance slit and the ion exit slit were 0.12 mm x 1.5 mm and 0.015 mm x 1.5 mm respectively.

The electrostatic shield, [7], provided a boundary for the electric field between the ion source and the ion acceleration tower. The shield was a cylindrical cage, covered with a fine wire mesh of high flow conductance.

Eight longitudinal stainless steel rods held rigid by the base at the top end of the source, and by a ring at the other end supported the wire mesh. High conductance was necessary so that the pumping efficiency within the cage was not impaired.

The HPCI source was mounted on the vacuum chamber port flange by a cylindrical steel support, [8], and a cylindrical block machined out of mica, [9], to electrically insulate the HPCI source from the rest of the system. The steel support was slotted to decrease heat conduction.

Main heating of the HPCI source was provided by a stainless steel heating mantle, [10]. The heating mantle was composed of two half circular blocks with eight vertical (0.25 inch wide) grooves, in which heaters were embedded. The heaters used were 0.25 inch * 2.5 inch, 200 watt Hotwatt cartridge heaters model 8017. The two half circular blocks were screwed directly onto the ion source tube.

An additional set of six Hotwatt cartridge heaters (base heater), [11], together with a heat shield, [12], was installed around the cylindrical stainless steel support (between the HPCI source tube and the main flange). These heaters were held in place through groves bored into the mica insulation block, and were used to eliminate the presence of any cold spots along the gas path to the ion source, in other words, to ensure that the gas before it reaches the reaction zone attains the temperature of the HPCI source.

Finally, all electrical connections to the HPCI-source, and to the electron gun assembly were made through glass to metal electrical feedthroughs, which were soft-soldered on specially designed adaptors welded onto the main flange carrying the HPCI source. High voltage to the ion source was supplied by a Hewlett Packard (Harrison 6525A, low ripple) DC regulated power supply.

B. Temperature Control and Measurement

The temperature of the HPCI source was controlled by manual setting of the heating mantle and base heater voltages. The heater voltages were supplied from individual auto transformers (Variac) followed by Hammond isolation transformers. The use of isolation transformers was necessary since the heaters were to float at HPCI source voltages (1.0 to 3.0 KV). Typically, some three amperes at fifty volts on the heating mantle heaters would produce a temperature of 500 K at the reaction zone of the HPCI source. A constant temperature could be reached in about one hour, after a change in the setting of the Variac, by allowing the temperature to reach a steady state. It had been found (48) that allowing the HPCI source to reach a steady state gave a much more constant temperature than could be obtained by an automatic temperature controller.

The temperature at the reaction zone of the HPCI source was monitored by an iron-constantan (J-type) thermocouple.

A small hole was drilled and tapped into the metal tube housing of the HPCI source. This hole was at a level in between the electron entrance slit and the ion exit slit. In order to ensure intimate contact between the thermocouple and the source housing the following arrangement was selected. A hole was drilled through the center of a screw. The thermocouple was inserted into the hole and silver-soldered at the tip of the screw. The screw was then screwed tightly into the tapped hole at the metal block housing the source. A second thermocouple, constructed the same way as the one above, was installed at the middle of the cylindrical stainless steel support. The temperature at this location was kept close to that of the reaction zone.

Both thermocouples were read with a Newport (model 268-JCI) twelve channel digital pyrometer. This is a J-type sensor pyrometer with a resolution of 1.0°C and an accuracy of ± 1.6°C at 25°C. Since both thermocouples were floated at the HPCI source voltage care was taken to electrically insulate the pyrometer and all the thermocouple connections.

C. Sample Introduction

As mentioned previously, gas samples were prepared and stored in the 5 L bulbs of the gas handling system. These gas samples were brought to the HPCI source through Pyrex glass tubing, [13]. The flow of the sample from the bulb/manifold assembly to the HPCI source was controlled by a Granville-Phillips valve followed by a Nupro all metal needle valve (see Figure 2.3). The gas, from the gas handling system, entered the HPCI source in a slow flow through a 14 mm i.d. pyrex tubing and was pumped out of the HPCI source through the outlet line by a mechanical pump controlled by an intermediate capillary (capillary pumping). This pumping was necessary to ensure the presence of a fresh and uniform sample in the HPCI source at all times during an experiment, and to avoid concentration build up of the heavier species in the gas mixture at the ionization zone.

The concentric sample inlet/outlet tubes were mounted to the base of the HPCI source assembly through a small Kovar seal which was silver-soldered onto an adapter flange. Around the concentric tubes was another glass tube which was also silver-soldered to the base of the assembly through a stainless steel bellow to allow flexibility. The outer glass tube was sealed onto the main flange by a Viton "o"-ring. It was used to hold "pencil" heaters, [14], directly against the inlet/outlet lines. Five 90 watt Hotwatt heaters were used to ensure that no condensation occurred in the glass tubing and for bake-out purposes. A thin sheet of stainless steel heat shield, [15], was wrapped around the heaters in order to achieve more uniform heating. Also, the glass tubes connecting the gas handling system to the HPCI source were wrapped in heating tape, again for purposes of degassing and to prevent condensation.

The total pressure in the HPCI source was monitored by a Validyne variable reluctance transducer (pressure range 0.001 to 15.000 Torr). The transducer was connected on the outlet line of the HPCI source, before the Phillips valve which was used to connect the outlet line to the exhaust pump via the capillary tube. Operation and control of this transducer was identical to the one discussed in section 2.3 of this Chapter. System calibration was necessary to obtain a known relationship between input pressure and output reading. Since transducer temperature had a big effect on output readings, thermostatic control was necessary. It was operated at temperatures below 80°C because at higher temperatures this pressure measuring system could not be zeroed. This can be considered as a disadvantage in a case where the temperature of condensation of a particular reacting gas is greater than 80°C.

With this sample introduction system, the flow rate from the gas handling system (GHS) to the HPCI source had to be a clearly defined function for quantitative results to be obtained. For this reason, the capillary pumping conditions, the conductance of the pyrex tubes connecting the GHS to the HPCI source, and the conductance of the leaks were chosen so as to ensure viscous flow from the high pressure side (GHS) to the low pressure side (HPCI source) when the pressure in the flow system and the HPCI source was between 1.5 and 10 Torr.

The advantage of having a viscous flow is that the composition of the vapour in the ionization chamber is the same of that of the sample in the 5 L bulb (49, pp.125), i.e. to avoid fractionation of the minor components. This is a serious problem when the sample gas flow through the ionization chamber is molecular, under which conditions the different components in the gas mixture would not have the same velocity, i.e. lighter gases escape faster from the high pressure side which causes concentration build up of the heavier components in the ionization zone.
A confirmation of the lack of fractionation was obtained by observing the small change (5%) in equilibrium constant value for the aniline monomer/dimer equilibrium (Chapter 3), after 85% of the gas mixture had flowed out of the 5 L storage bulb.

Furthermore, another thing that had to be checked was the possibility of pressure gradient along the tubes associated with the sample introduction gas flow. The pressure gradient between the manifold, the HPCI source, and the transducer was negligible because the size of the connecting glass tubes was large, (14 mm i.d.). The pressure gradient can be calculated from the Poiseuille's law (46, pg. 84):

$$n_m = (\pi a^4((P_2)^2 - (P_1)^2))/(16*\eta*l*R*T) \qquad (2.4)$$

where n_m is the rate of gas flow (moles/sec) through a tube of length l and radius a, R is the gas constant, T is the temperature, and η is the viscosity of the gas. P_2 and P_1 are the inlet and outlet pressures of the tubes to the HPCI source. To measure the flow, a bubble flow meter was installed on the exhaust of the mechanical pump that controlled the flow through the HPCI source. When the pressure of methane was about 4.0 Torr, the flow rate was about 28 cc atm min^{-1}. The length of the tube from the manifold of the gas handling system to the ion source was about 1 m, with a radius of 0.7 cm. The viscosity of methane is 1.09×10^{-4} poise at 20°C (50). From equation 2.4 it may be calculated that the pressure difference between the manifold and the HPCI source is less than 0.5%. Therefore, the pressure reading of the Validyne transducer is an accurate representation of the pressure in the HPCI source.

2.5 The HPCI Source and the Direct Insertion Probe Sample Introduction System.

The sample introduction and inlet system GHS associated with the conventional HPCI source discribed in section 2.4C has been utilized extensively over the years in Dr. Kebarle's group and has been proven satisfactory for handling gaseous and high volatility compounds. However, it has limitations in quantitative studies, where involatile, thermally labile samples are involved.

Solid compounds had to be dissolved in appropriate solvents prior to their syringe injection into the GHS. Depending on the reaction system studied, proper selection of the solvent had to be made to ensure the solvent vapor would not interfere with the reaction system studied. Nevertheless, in some cases interferences from the solvent ions are unavoidable.

Furthermore, when low volatility analytes and especially compounds which are strongly adsorbed on surfaces were injected into the storage bulbs it was found that the gas mixture flowing through the ion source had a changing composition. After the flow through the ion source was initiated the concentration of the "sticky" compound was low and increased gradually with time. With some compounds the concentration reached a steady state only after one hour or longer. Also, once the system was exposed to such compounds, long term pumping was required afterwards to fully remove all remaining traces, and such traces often interfered in the reaction systems that were studied next.

One of the objectives of the present project was to devise a sample introduction system that would provide a simple and rapid introduction of nonvolatile low vapor pressure compounds to the reaction zone of the ion source.

The design of this direct insertion probe introduction system involved a vacuum insertion lock assembly similar to those available with commercial mass spectrometers, a heated or cooled chemical ionization sample introduction probe similar to the one designed by Hogg (36), a pumping system to accomodate the insertion lock (see figure 2.3), and adapter flanges to couple the insertion lock to the HPCI source housing. Most of the system's components were machined out of nonmagnetic stainless steel, but for some parts the use of quartz was necessary (see section 2.5A,B,and C of this Chapter).

Figure 2.5 gives a schematic representation of the direct insertion probe sample introduction system coupled to the HPCI source and of the CI sample introduction probe. Also, a set of photographs showing the major components of the system is given in Figure 2.6. All the individual components of this system are discussed in parts A,B,and C of this section.

A. Description of the Basic Components.

The vacuum insertion lock assembly shown in Figure 2.5 consisted of the two independent stages of vacuum lock, [4], and [7],--separated by a Whitey 0.50 inch i.d. ball valve, [6], an interface component, [11], a supporting tower, [10], and a shaft support, [12].

The first stage vacuum lock, [4], together with the shaft support,[2], served for support and allignment of the sample probe. The pumping port I,, [5],via an isolation

Figure 2.5 Cross Section View of the Direct Insertion Probe Sample Introduction System Coupled to the HPCI Source Housing, and of the Chemical Ionization Sample Introduction Probe.

1. Chemical ionization probe
2. Shaft support
3. Sealing "o"-rings
4. First stage vacuum lock component
5. Pumping port I leading to rough pumping and high capacity pumping
6. Ball valve
7. Second stage vacuum lock component
8. Pumping port II leading to high capacity pumping
9. Adapter flange
10. Vacuum insertion lock supporting tower
11. HPCI source/direct insertion probe system interface component
12. HPCI source housing
13. "Rulon" probe guide
14. Gas exhaust line
15. Electron gun assembly
16. Ion repeller and/or electron trap
17. Electrostatic shield

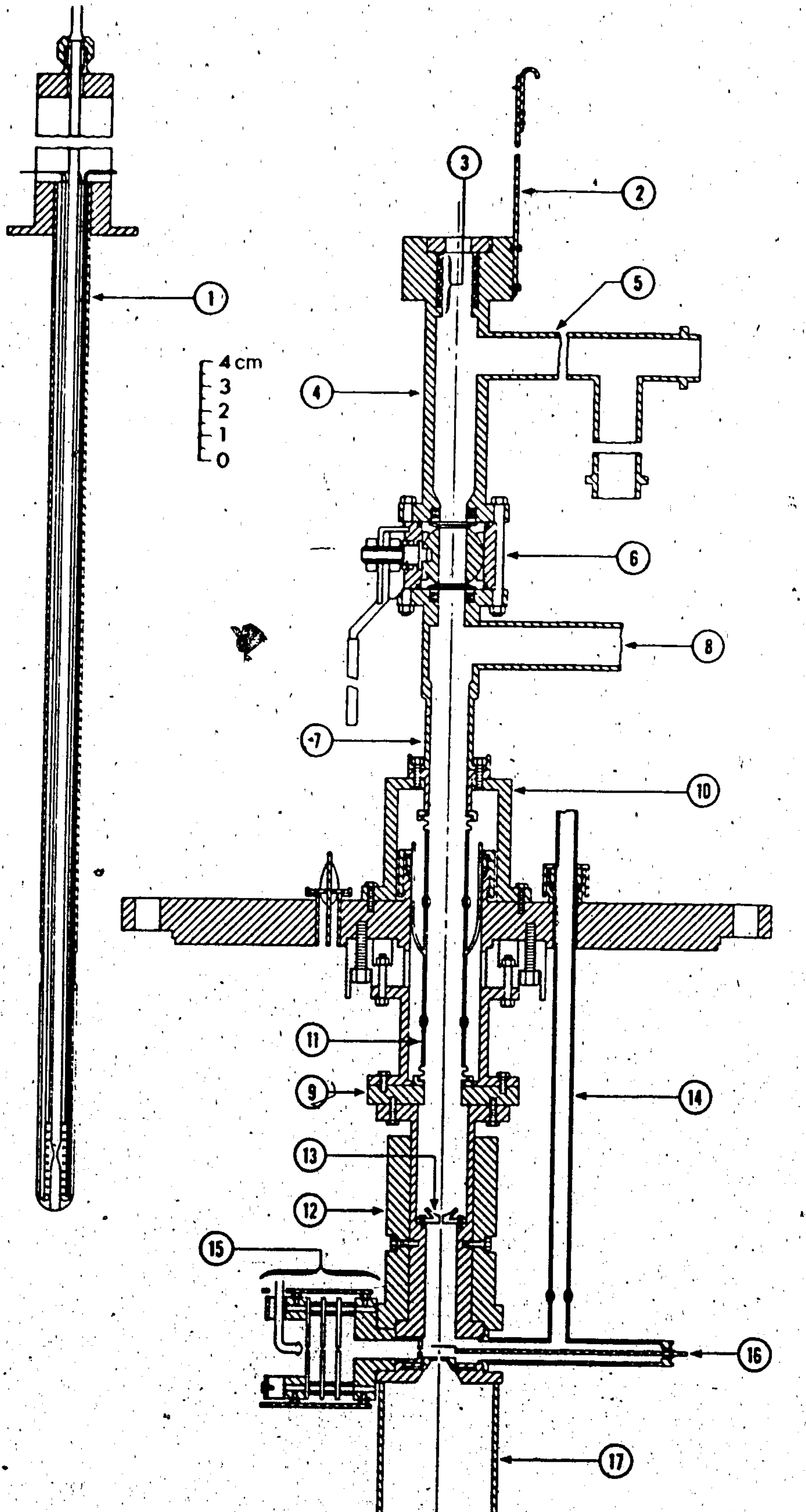
4 cm

Figure 2.6 Photographs of the Insertion Lock Components top left), HPCI Source Housing and Electron Gun Assembly (top right), and the Insertion Lock, HPCI Source Housing, and Electron Gun Components Coupled Together as they Appeared in the Final Configuration (bottom).

1. First stage vacuum lock component
2. Pumping port I leading to rough pumping and high capacity pumping
3. Ball valve.
4. Second stage vacuum lock component with pumping port II.
5. HPCI source/direct insertion probe system interface component and vacuum insertion lock supporting tower
6. Thermostatted HPCI source housing
7. Electron Gun Assembly and electron beam sheilding (on the left)

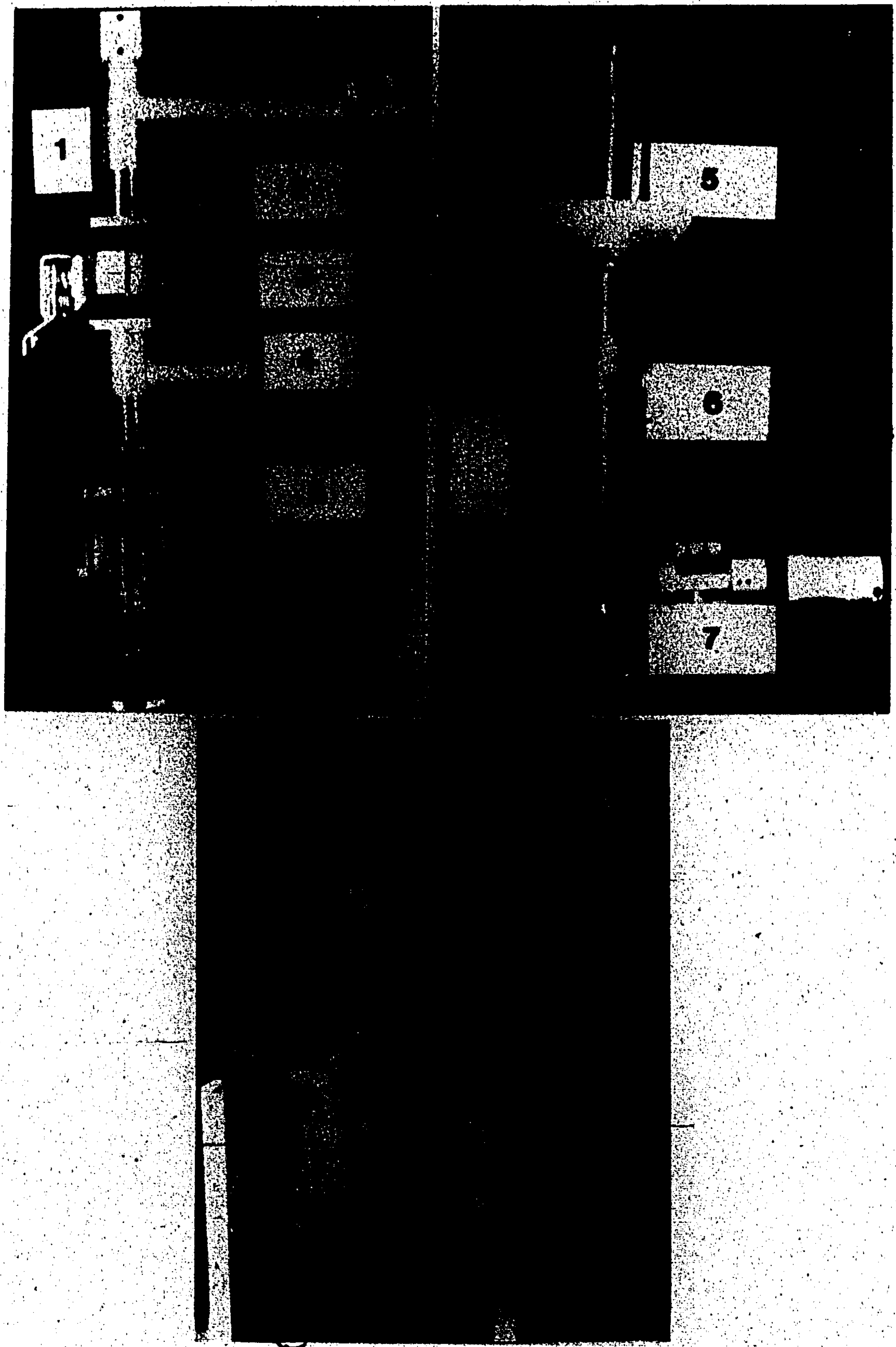
1
5
6
7

valve, was used to evacuate the first stage vacuum lock area and the gas inlet lines when the sample probe was inserted to its first stop, i.e. the top of the ball valve level (see part D of this section). Apart from rough pumping this area additional high capacity pumping was available through the GHS diffusion pump via a second isolation valve, if the sample was to be purified and also if gas inlet line cleaning was desirable. A set of four viton "o"-rings of 0.5 inch i.d. separated by stainless steel spacers, and located at the top of the first stage vacuum lock component, [3], served for sealing the sample probe shaft against atmosphere when the tip of the sample probe was exposed to vacuum. The bottom end of this first stage vacuum lock component was machined in such a way (square type flange with a 0.495 inch i.d. hole in the middle) as to couple directly to the body of the ball valve and also to ensure sealing against atmosphere, when screwed tightly against the ball valve. A ball seal (0.495 inch i.d.), along with a stainless steel spacer was also installed to this end of the component and served for shaft alignment purposes.

The ball valve was a "60" series Whitey valve and was used as supplied after being thoroughly cleaned with a number of solvents. The ball valve's teflon and viton seals, when held tightly against the flanges of the first and second vacuum lock components, served as a lock for the high vacuum present at one of its sides (HPCI source housing) against atmosphere present at the other. During normal system pump down with the ball valve closed, pressures as low as 5 x 10^{-8} Torr were obtained (measured on the ionization gauge located outside the HPCI source housing).

Pumping port II was connected via an isolation valve to the diffusion pump of ~~the~~ GHS, and was used to evacuate the area around the sample probe shaft between the "rulon" probe guide, [13], and the sealing rings, [3], during normal system operation with the probe fully pushed home. When the probe tip was snugly mated with the probe guide, back streaming of reagent gas from the reaction zone resulted in a pressure increase in this area. This pressure buildup was found to be cause of electrical discharges when the pressure was raised above 10^{-3} Torr (see part C of this section). High capacity pumping available via port II kept this area at pressures below 10^{-5} Torr and therefore discharges were totally suppressed. On both sides of this component were machined special flanges that coupled leak tight to the ball valve body at one end and to the interference component at the other. Again, a ball seal (0.495 ~~inch~~ i.d.) along with a stainless steel spacer was also installed at the top end (next to the bottom of the ball valve) of this component and served for shaft alignment purposes.

The interface component, [11], was coupled to the HPCI source housing at the adapter flange, [9], level and replaces the concentric sample inlet/outlet lines available with the conventional design. This component consisted of a

0.625 inch i.d. and 2.0 inch long quartz tube coupled to two stainless steel bellows (each being 0.625 inch i.d. and 0.75 inch long), via Kovar seals at each of its ends. One of the bellows was silver soldered onto the adapter flange, [9], at the base of the source housing and the second one was silver soldered to the flange which coupled the interface component to the second stage of the vacuum lock, [7]. The bellows were used to allow flexibility when aligning the system.

The purpose of using this quartz tube was to electrically insulate the high voltage source housing from the direct insertion probe sample introduction assembly, which was kept at ground potential. Also, the use of quartz rather than borosilicate glass was required because of the poor electrical insulating properties of the latter at elevated temperatures.

Around this quartz tube was connected a second tube (1.250 inch o.d.), which in turn was sealed onto the main flange supporting the ion source via an "o"-ring coupling and served as a seal for the high vacuum side against atmosphere.

The bottom part of the ion source housing was drilled out to 1.0 inch i.d. and 3.5 inch deep from the top of the base flange in order to fit in it the "rulon" probe guide. The guide was held against a knife edge base (at the source block) by six small screws to ensure no back leakage of reagent gas from the high pressure (reaction zone) to the low pressure side (interface area) when the CI probe was pushed fully home.

The probe guide was machined in such a way as to provide a good seal when mated with the probe tip. Rulon has a relatively inert surface, and is also a good electrical insulator . Its thermal conductivity is high enough to allow the probe tip to attain the ion source temperature in a short time, when independent heating of the probe was not desired. Rulon retains its rigid shape after repeated heating, up to 240°C. However, in some of the experiments, it was heated up to 300°C without creating any major problems.

The support tower, [10], was attached to the insertion lock system at the top flange of the interface component level and was used to support and hold the assembly rigidly against the main flange of the instrument.

All the components of the insertion vacuum lock system were larger than 0.50 inch i.d. in order to accomodate the 0.478 o.d. shaft of the specially constructed CI probe.

Finally, alignment of all the insertion lock system components was achieved by putting through it a 0.478 inch o.d. all-metal shaft and maneuvering it around until a perfect fit was obtained. After having all joints tightly screwed together, the system was leak tested with helium prior to its use.

B. The Direct CI Sample Introduction Probe.

A cross sectional view of the specially constructed chemical ionization-sample introduction probe is given in Figure 2.7. The shaft of the probe was constructed in such a way as to fit, vacuum tight, to the previously described vacuum insertion-lock system. Both sample and reagent gas were introduced into the reaction zone of the HPCI source via this probe.

The main body of the probe (shaft) consisted of 0.478 inch o.d. non-magnetic stainless steel tube extended to a 0.472 inch o.d. quartz tube, via a Kovar to quartz graded seal, which, in turn, was sealed to the 0.197 inch o.d. quartz inner tube at the probe tip level. The reason for using a quartz tip probe was to avoid exposure of the metal part of the shaft against the high voltage "walls" of the HPCI source housing.

The inner tube, which was used to admit reagent gas to the reaction zone, terminated at the top of the probe handle in a specially designed adapter seal, using a rubber "o"-ring, and served as a quick connector for coupling the probe to the reagent gas inlet line coming from the GHS. A slight constriction in the inner tube, 0.55 inch from the tip, served as a support for the sample container which was made from melting point capillary. A small piece of an appropriately shaped stainless steel strip was used as sample container holder. This prevented the sample

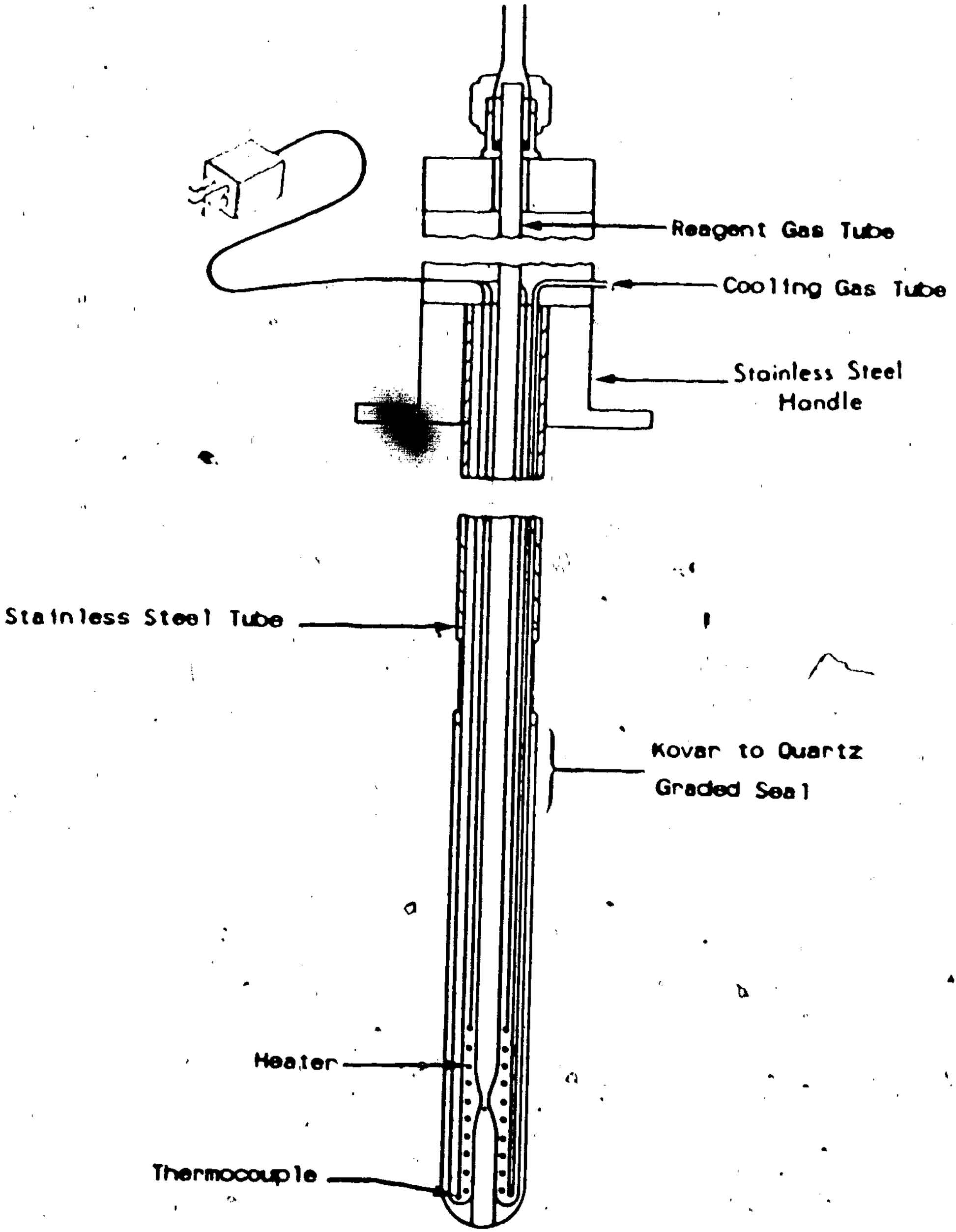
Reagent Gas Tube
Cooling Gas Tube
Stainless Steel Handle
Stainless Steel Tube
Kovar to Quartz Graded Seal
Heater
Thermocouple

Figure 2.7. Cross Sectional View of the Chemical Ionization Direct Insertion Probe.

capillary from falling out during probe insertion as well as providing better thermal contact between sample holder and probe heated area.

An adjustable locking collar on the probe shaft served as a guide for the probe and indicated when the probe tip had cleared the ball valve area during probe withdrawl, and also when the probe was fully home during probe insertion. During probe insertion a slight push of the probe against the "rulon" probe guide was found sufficient to ensure a good vacuum tight coupling.

The probe is equipped with a heater and thermocouple running the length of the shaft and terminating at the probe tip. A spirally shaped Nichrome heater heats the region from the tip of the probe to a point just past the constriction in the inner quartz tube. The heater was fixed in the probe tip by having the Nichrome wire tightly wrapped against the inner tube. A cable and plug connects the probe heater to a 115 V/12.5 V filament transformer, whose primary is controlled by a Variac variable autotransformer. Heating of the probe tip (sample area) is achieved by manually adjusting the current passing through the Nichrome heater via different settings of the Variac autotransformer.

Probe tip temperature, and therefore sample temperature, is monitored with a J-type thermocouple located against the heater towards the bottom of the probe shaft.

The CI probe was heated independently from the ion source. Temperatures up to 600°C were measured at the probe tip area with this heater arrangement at atmospheric pressure. Probe temperatures, higher than those of the ion source, had little effect on altering the ion source temperature. Thus when the probe temperature was about 50°C higher than that of the ion source, the observed increase in the ion source temperature was only 1 to 5°C.

Sample cooling is provided by blowing cold nitrogen gas or air, around the inner tube at the probe tip level (see Figure 2.7) via teflon tubing from a union at the top of the probe handle. The probe tip area could be cooled down to 100°C when the ion source was kept at 227°C. The probe can be heated and cooled much more rapidly than the ion source.

Chemical ionization reagent gas from the GHS flows through the gas inlet line and the inner tube of the probe, around the heated sample capillary and enters the reaction zone as a mixture containing a certain concentration of sample vapour evaporated from the capillary. The concentration varies with sample volatility and probe tip temperature. The gas mixture exits the reaction zone through the specially designed gas exhaust line (see [14] in Figure 2.5). Reagent gas flow is controlled by the needle valve at the GHS, and a capillary which restricts the flow in the exhaust line. The source pressure was fixed at the required settings by adjusting the needle valve.

The temperature of the reagent gas was controlled by heating the flow tubes. Heating was not available only for the region along the inner tube of the CI probe.

Also, since the probe tip was heated independently this caused the sample temperature to be different than that of the reagent gas. However, this does not effect the measurements because temperature equilibration of gases at pressures of a few Torr is very fast.

The concentration of sample vapour in the ion source was controlled by the temperature of the probe tip. The relative sample concentration was monitored by observing the intensity of ions due to the sample. A steady ion intensity could be obtained by careful control of the reagent gas flow, and probe tip temperature.

Typical sample weights used were of the order of 5 to 10 mg. The period of time that these quantities lasted, during system operation, varied with sample volatility and probe temperature. A systematic evaluation of the sample introduction system is given in Chapter 3.

A second CI sample introduction probe was designed and was used when labile and highly volatile samples were used. Samples of this nature were introduced into the system by the conventional procedure and this second "probe" simply served as a gas flow tube linking the inlet line coming from the GHS, with the ion source.

The only difference between this probe and the one previously described, was that its outer shaft consisted of a quartz tube (0.472 inch o.d.), and that the inner tube was thermostatically controlled along its entire length. Heating of the inner tube was accomplished by having a

Nichrome ribbon heater wrapped around it. The current going through the heater was controlled in exactly the same way as for the heater of the other probe. Its temperature was kept at the same level as that of the GHS and the sample inlet line, in order to avoid sample condensation on its path to the ion source.

C. Suppression of Electrical Discharge in the Interface Component Region.

The HPCI source of the mass spectrometer is run at 3 kV during standard operation, while the probe vacuum lock, the solids probe, the GHS, the gas inlet lines, and all the other components, which are physically attached to the ion source through vacuum feedthroughs, are at ground potential. This was accomplished by having the interface component ([11] in Figure 2.5), the CI probe tip, and all the parts of the reagent gas carrying lines made out of quartz and pyrex. However, in the development stages of the sample introduction system, under certain pressure and temperature conditions, high voltage break downs were experienced due to electrical discharges across the gas sample introduction system. It was established empirically that discharges took place from the ion source across the gas inlet lines to the GHS when the pressure in the lines was between 10^{-3} and 1.0 Torr. Discharges occurred also from the ion source to the vacuum lock assembly due to build up of gas in the interface volume connecting the ion source to the vacuum lock. This pressure build up was due to leakage of gas across the not completely tight rulon/probe tip contact.

Even though gases are known to be insulators at very low pressures and at high pressures, in the pressure range 10^{-3} to 1.0 Torr they become conducting and permit discharges (51). For most chemical ionization mass spectrometric studies, the operating gas sample pressures are in this pressure range and therefore precautions have always been taken to build gas sample introduction systems that would be free from discharges. A number of authors (52,53) have investigated the problem and different discharge suppressor systems have been proposed.

With our conventional sample introduction system, maintaining the GHS and the other gas inlet/outlet components at ground potential, (i.e. free of discharge), is not a problem since all the lines connecting these components to the ion source are long and made from glass. Furthermore, the operating pressure is mostly above 1.0 Torr. In addition, the needle valve at the top end of the gas inlet line serves as an insulator, securing the GHS from high voltage because discharges do not occur at the pressures normally found on the high pressure side of the valve. Nevertheless, a ground point is provided next to the needle and Philips valve (capillary pumping controller) for double safety purposes.

It was observed with the solid probe sample introduction system that if the high voltage was on, while gas was admitted to the HPCI source, discharges occurred at gas pressures in the HPCI source, and consequently, in the gas inlet/outlet lines below 0.8 Torr. These discharges could be avoided by switching on the high voltage only after the gas pressure in the source had been stabilized at the 0.8 Torr level or higher. Also, at the end of each experiment, evacuation of the source was commenced only after the high voltage had been switched off.

The discharges of the vacuum lock assembly could be prevented by having the interface area under vacuum at all times. Since the rulon joint could not be made completely tight, the volume was continually pumped by introducing pumping port II, see Figure 2.5. This line had sufficient capacity to maintain a pressure of 5 x 10^{-6} Torr (as measured by the GHS's ion gauge controller), with the ion source being at 10.0 Torr. Under these conditions, discharges in the area were totally suppressed.

D. Summary of Routine Solid Sample Introduction Procedures

The following step by step procedure had to be followed, carefully, when solid samples were used in order to ensure safety of operation. This procedure requires that a reagent gas mixture has already been prepared in the GHS, the CI probe is disconnected from the system, and all high voltages are switched off.

1. Deposit sample into capillary, insert capillary into the heated well, and place metal security strip around it.
2. Insert probe carefully into the first stage vacuum lock component, bringing it to the point where the end of the probe is just short of the ball valve (indicated by the location of the probe's adjustable locking collar against the shaft support). Adjust sealing "o"-rings until a tight fit against the probe shaft is obtained. Connect CI probe to the gas inlet line, via the quick connector at the top of the handle.
3. Slowly open valve 1, located on pumping port I and evacuate the inlet line and the first vacuum lock component area until a pressure of 20 mTorr or less has been obtained. If sample purification is required, close valve 1 at this point and open valve 2 (also located on the T joint at the end of pumping port I). This exposes the area to high capacity pumping for the desired length of time.
4. Once the pressure in the top part of the insertion lock is at least 20 mTorr, open the ball valve and carefully slide the probe forward until the tip is met with the "rulon" guide.
5. With the probe fully home, evacuate the interface component area, via pumping port II, fully open the exhaust valve and after allowing some time for pumping, start

bleeding in reagent gas. Stabilize the reagent gas pressure at the 1.0 Torr level or higher, using the needle valve.

6. After making sure that the ion source pressure is above 1.0 Torr and the pressure in the interface component is below 10^{-5} Torr, the ion source high voltage may be switched on.

7. Having optimized all operational conditions, i.e. electron and ion beam, reagent gas pressure, etc., obtain a mass spectrum for the reaction mixture used. Next, switch into single ion mode and observe the intensity of the ion of interest, while altering the probe tip temperature. Once a desirable ion current and consequently, an ion time profile has been obtained, data collection may commence.

To shut down the system, the procedure must be followed exactly in reversed order.

2.6 The Electron Gun Assembly

A. Arrangement of Electrodes

A schematic diagram of the electron gun assembly is shown in Figure 2.8. The design of this gun is different from the one generally used in this laboratory and described by Arshadi (54). In the present case the electron gun is directly attached to the ion source as it is shown in Figure 2.5. This design only requires half the number of electrodes

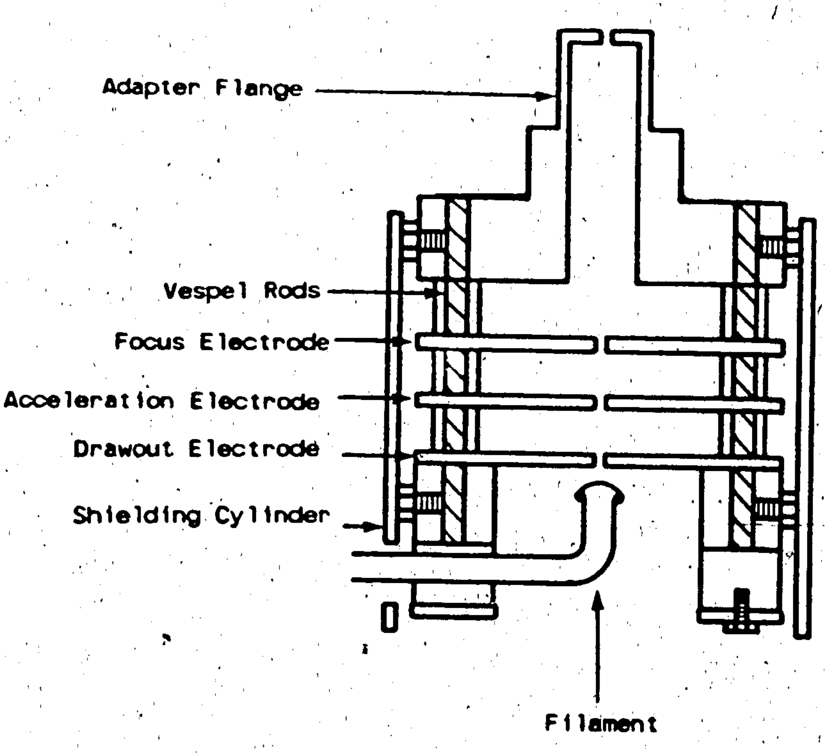
Adapter Flange
Vespel Rods
Focus Electrode
Acceleration Electrode
Drawout Electrode
Shielding Cylinder
Filament

Figure 2.8. Cross Sectional View of the Electron Gun Assembly.

with respect to the general design, and the specific mounting reduces alignment problems.

The electron gun assembly consisted of a filament element, a filament element holder, three electrodes (drawout, acceleration, and focus), and a specially designed adapter flange, which supported all the electron gun components through vespel rods against the source housing.

The filament was at sufficient distance from the ion source in order to avoid its exposure to high pressures and prolong its lifetime. For operation with positive ions, the center of the filament was maintained at ground potential and -2.0 to -3.0 kV relative to the ion source. Electrons emitted from the heated filament were accelerated and focussed by the electrode plates, along the z axis towards the ion source.

A simple potential divider was constructed to provide appropriate voltages to the electrodes of the electron gun. All electrode voltages were adjustable, via helipots attached to the potential divider. The voltage for the potential divider was supplied by a Hewlett Packard (Harrison 6110A, low ripple) regulated high voltage power supply. Three control meters were installed to monitor total emssion, case and trap currents under continuous electron irradiation. Typical voltage settings and control meter readings are given in Table 2.1.

The voltage to the drawout electrode was provided, via a separate voltage power supply (CALEX 30V, 200 mA), in order

TABLE 2.1 Typical Operating Voltages for the Electron Gun Assembly.

Electrode	Voltages (Volt)
Filament	0
Drawout	30
Acceleration	852
Focussing half plates	
Y_1	1020
Y_2	1118
Ion source, Trap, Repeller	2900

Typical Control Meter Reading Under Continuous Electron Irradiations:

Total Emission Current[a]:	800 μA
Case Current[b]:	30 μA
Trap Current[c]:	0.2 μA

[a] The amperemeter monitoring total emission is connected in series with the line connecting the filament element to ground. The current measured represents the number of electrons leaving the filament element.

[b] The case current amperemeter is connected in series with the high voltage line leading to the ion source. The current quantities measured are from electrons striking the ion source.

[c] The trap current amperemeter is connected between the ion source and the electron trap terminals, and measures the amount of current resulting from electrons reaching the electron trap.

to avoid loading of the main high voltage power supply when the filament emission was set high. Loading of the electron gun and the ion source power supply (main power supply) would severely affect the electron and ion focussing.

The filament of the electron gun was constructed from thoriated iridium because this material is known to be resistant to attack by a large number of gases. However, from the ferrocene study, it was found that filaments made of 75/25 tungsten/rhenium had longer lifetimes than the former material.

The effect of a hot filament (maximum emission) on the ion source temperature was found to be ion source temperature dependent. Heated filament electron beam sources, while at maximum emission, operate at around 200°C (55). With a hot filament, an ion source temperature of 50°C was found to increase by 2 to 3°C in the first 15 minutes of electron irradiation, and then stabilize at the higher temperature. Ion source temperatures of 130°C or above were unalterable, even by prolonged continuous electron irradiations. There were no special precautions taken to avoid this problem, since the temperature of the ion source could be regulated fairly precisely, through the ion source heater controllers. Focusing of the electron beam was performed with the system in vacuum. While in continuous irradiation mode, the filament emission and the electron gun electrode potentials were adjusted until a maximum case, and subsequently, trap current was obtained (see table 2.1). Optimum voltage settings for electron beam focussing under continuous irradiation are not necessarily the same as optimum settings for pulsed electron beam focusing, mainly because the drawout voltage is different for the continuous and pulsing modes.

B. Pulsing of the Electron Beam

Pulsing of the electron gun was accomplished by varying the potential of the drawout electrode at regulated intervals. Figure 2.1 shows a block diagram of the instrument including all the pulsing electronic components.

Electrons could only pass into the ion source when the filament was at a higher negative potential than the drawout electrode. In the pulsing mode, the drawout electrode was maintained some 30 to 60 volts negative to the filament.

Pulses generated by the master pulse generator trigger a floating pulse amplifier, which in turn altered the potential of the drawout plate to some 45 to 140 volts positive with respect to the filament for the desired period of time. This allowed electrons to pass through the drawout plate into the focusing and accelerating region of the electron gun. After the preset period of time had elapsed, the floating pulse generator would return the drawout plate to its original potential, negative with respect to the filament. In this way pulses of electrons of known time duration could be delivered to the ion source. The period of the electron beam on/off cycle (2.6 to 10.3 msec/cycle, depending on the experiment) was controlled by the master pulse generator whereas the duration of the "on" time for the electron beam (10-140 sec) was governed by the pulse amplifier. The pulse amplifier was battery powered and could be floated to drawout potentials. Controls on the pulse amplifier allowed adjustment of the pulse width, pulse height (positive polarity pulse), and back-off voltage (a negative voltage pulse used to repell the electron beam) until the best intensity of electron beam pulses was obtained.

The triggering pulse from the master pulse generator was also used to initiate the sweep of the multichannel scaler for data collection. In this manner the time dependence of ion intensities following the ionizing pulse could be obtained.

When the electron gun was not pulsed, the electron beam striking the ion source was around 30 microamperes. Only a small fraction of the electron beam passed through the electron entrance slit and reached the trap in the ion source. The current measured at the electron trap was 2×10^{-7} Amperes. From this, it can be calculated that in a 10 μsec pulse approximately 1×10^{7} electrons enter the ion source.

C. Electron Beam Deflection Due to Stray Magnetic Fields.

During the developing stages of this instrument, it was found that weak stray magnetic fields, resulting from the analysing magnet, significantly affected the focusing of the electron beam. By monitoring deflections in the trap current meter, it was observed that a perfectly focused electron beam, with the system in vacuum, was severely deflected when the analysing magnetic field was varied.

With the analysing magnetic field set at maximum, stray fields of the order of 100 to 150 Gauss were measured in the area occupied by the electron gun in the vacuum chamber. They were found to increase in intensity with increasing analyzer magnetic field, which indicated that electron beam deflection is magnetic field dependent. Furthermore, this indicated that ions of different mass would be resulting from different electron intensities such that their signals would not be comparable.

A mass dependent change of the ion intensity was observed when ions of even minimal difference in mass were selected for this investigation. By refocusing the electron beam at each given mass, it was found that the ion intensity could be increased by at least a factor of five, and the gain of intensity upon refocusing depended on the mass difference between the ions under investigation.

To overcome this problem, the space containing the electron beam path, i.e. electron gun area, was heavily shielded with high magnetic moment (μ) material (Netic-Conetic). The use of this shielding reduced the perturbing effect of the magnetic field on the electron beam to a negligible level. The shielding applied was proven, experimentally, sufficient to ensure complete absence of electron beam deflections even at relatively high masses. With the shielding in place, refocusing of the electron beam was proven unnecessary even when the mass difference of the ions under investigation was relatively high (230 amu or higher).

2.7 Ion Acceleration from the Ion Source to the Mass Analyzer.

Ions coming out of the ion source's ion exit slit were accelerated and focused towards the flight tube of the magnetic analyzer.

Acceleration, focusing, and deflection of the ion beam was achieved by a series of six electrode plates (ion acceleration tower) put together in a tower type arrangement, and held by the bottom against the analyzer's tube entrance. All electrodes were electrically insulated from each other. A schematic diagram of the ion acceleration tower with all the electrodes specified is shown in Figure 2.9. The cone, cone exit, and cylinder electrodes were mainly used for ion acceleration, while the

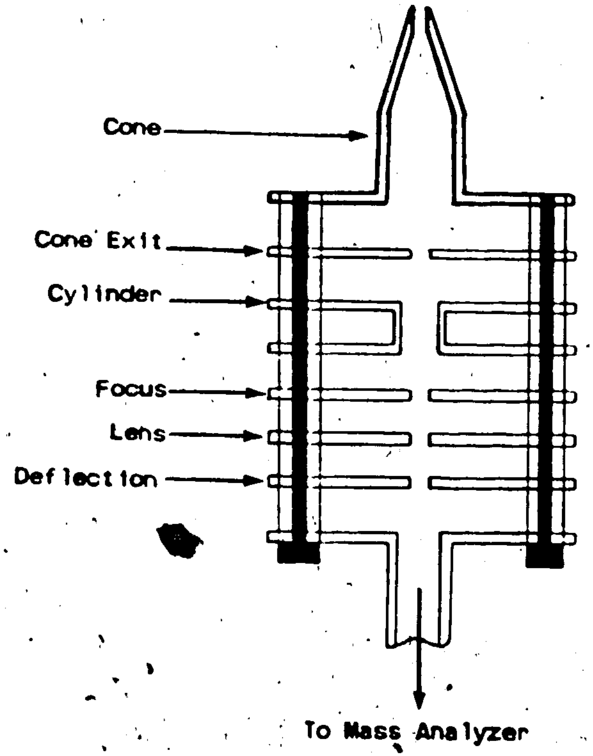
Cone
Cone Exit
Cylinder
Focus
Lens
Deflection
To Mass Analyzer

Figure 2.9. Cross Sectional View of Ion Accelerating and Focusing Electrodes.

others (focus, lens, deflection) served for x/y focusing and deflection of the ion beam.

The potentials of the ion acceleration and focusing electrodes were kept negative with respect to the ion source when positive ions were investigated. High voltage to the electrodes was provided via a potential divider connected in line with the ATLAS' high voltage power supply. Typical potentials applied to these electrodes for optimum operating conditions are given in Table 2.2. However, prior to conducting an experiment, the relative voltages of all six electrodes were chosen carefully until optimum sensitivity and mass resolution was obtained.

The resolution of the instrument under HPCI conditions using the 10% valley definition was estimated to be around 285 at m/e 43.

2.8 Mass Analysis and the Mass Readout System.

For the present instrument, the ATLAS's 20 cm radius 60° flight tube and electromagnet were used as a mass analyzer.

Positive ions from the ion source, after being accelerated and collimated by the ion acceleration tower electrodes and upon passing the analyzer's entrance slit, were subjected to magnetic analysis. The flight tube and the magnetic analyzer are kept at ground potential. Therefore, the kinetic energy of the ions entering the

TABLE 2.2 Typical Operating Voltages for Ion Accelerating Electrodes.

Electrodes	Voltage (Volt)
HPCI source and shielding cage	2900
Cone	1750
Cone exit	1759
Cylinder	2070
Focus half plates	
X_1	1950
X_2	1926
Lens #1	2010
Lens #2	2040
Deflection half plates	
Y_1	458
Y_2	470
Magnetic analyzer entrance slit	0

analyzer is determined by the voltage setting of the ion source. The electromagnet (mass analyzer) selects a particular primary ion reagent beam from the mixture of ions emitted from the high pressure ion source. Selection of a particular ion and deflection of all others is performed according to equation 2.5 (56).

$$m/e = 4.79 \times 10^{-5} (r^2B^2)/V \qquad 2.5$$

In this equation, r is the orbital radius of the ions' path, i.e. radius of the magnetic field, in cm, B is the magnetic induction (magnetic field flux) of the analyzer, in Gauss, which is applied to the ion in terms of force (evB) normal to the direction of its motion, and V is the accelerating voltage that has been applied to the ion. The constant of 4.79 x 10^{-5} has resulted from unit conversions. Equation 2.5 predicts the mass to charge ratio for the ion that will be transmitted through the analyzer for a particular V and B setting. Once the ion has entered the flight tube, it travels with a constant velocity through it, towards the ion detector.

As is evident from the above equation, the operating mass range of the magnetic analyzer is dependent on the strength of the field, radius of the field, and kinetic energy of the ions. Ions of different mass to charge ratio can be selected by means of scanning the magnetic field B while everything else is kept constant, or, by scanning the ion acceleration voltage, V, and keeping the rest constant. Both scanning modes were available with the present instrument, however, the first one was utilized for all experiments performed, due to its ease of operation and reproducibilty of results. Scanning the accelerating voltage introduces uncertainty in optimizing conditions for electron acceleration and ion focusing when HPCI source arrangement is utilized. Scanning of the magnetic field was obtained by varying the current through the magnet's coil, via the ATLAS' highly regulated constant current supply. With this particular electromagnet, the highest mass ion that could be transmitted through the magnetic field at an accelerating voltage of 2.9 kV was m/e = 220 Daltons.

Since the ATLAS MAT CH4 was not equipped with a data system, mass-marking facilities, or even a versatile and reliable mass-readout system, a system that would provide an effective and inexpensive solution to this problem was constructed. A number of versatile mass-readout systems, other than the commercial ones, for magnetic sector instruments, have been reported in the literature (57-59). Among these, the design by Bell (58) was found most suitable for our application.

A digital mass-readout system, identical to the one described by Bell was constructed by the Electronics Shop, at the Chemistry Department, and was interfaced to the instrument. This system was based on a commercial high linearity, temperature compensated Hall probe and an integrated circuit (Analog Devices AD 531L monolithic multiplier divider) capable of providing the transfer function $k(x^2/z)$, where k is a variable gain factor "corresponding" to the term $4.79 \times 10^{-5}\ r^2$ in equation 2.5, x is a voltage corresponding to B, and z a current corresponding to ion accelerating voltage. The output of the circuit is measured by a 4 1/2 digit voltmeter (Analog Devices 2008); by adjusting k the readout can be made to correspond to m/e such that of 1 mV = 1 amu. Furthermore, the circuits linear output can be used to drive the x axis of the mass spectrum recording apparatus.

For our system, as a field measuring device a Bell STJ8-0204 transverse Hall probe was used, powered by a Bell 810H field monitor. The probe was mounted in the pole gap on the ATLAS' magnet so that it was in good contact with the flight tube. The accelerating voltage was sampled from a resistor chain at the 6V level and was fed into the integrated circuit along with the output from the field monitor. A diagram of the Hall probe mounting arrangement and of the mass-readout system setup is shown in Figure 2.10. There were no modifications made to the circuit described by Bell since its performance was found very satisfactory for the mass range used. Calibration of the system was also obtained by following the procedures outlined in Bell's publication.

It should be mentioned, at this point, that an important assumption has been made in the derivation of equation 2.5

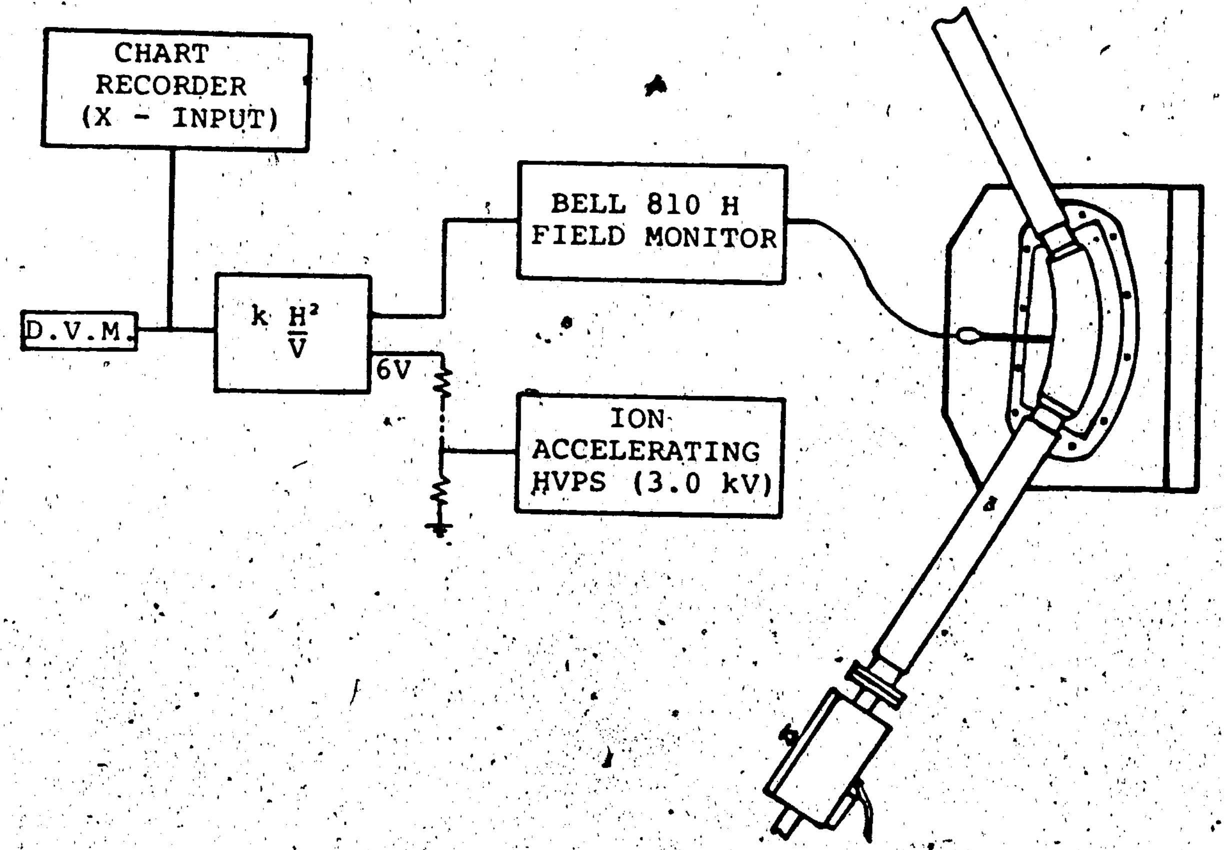
CHART
RECORDER
(X - INPUT)
D.V.M.
$k \frac{H^2}{V}$
6V
BELL 810 H
FIELD MONITOR
ION
ACCELERATING
HVPS (3.0 kV)

Figure 2.10. Diagram of the Hall Probe Mounting Arrangement and of the Mass Read-out System.

and in the design of the mass-readout system for relating m/e with B. It is assumed that a perfectly uniform magnetic field with sharp boundaries is available, and that the mass in focus at a given instant is directly related to the measurement of the magnetic field, B, at that instant. However, in practise, this is not the case. The path of an ion as it travels from the source to the collector is determined by the magnetic field at each point along the path, and if we are to predict the mass of ions reaching the collector at a certain instant, we shall need a map of the field along the entire path at that instant, in enough detail to give the required precision. Thus, by measuring the magnetic field at a single point, a number of uncertainties in the relationship between m/e and B are introduced. These uncertainties mainly result due to saturating Eddy Currents and hysterisis, which are the causes for non-uniformities in the magnetic field.

With rapid magnet scans, the effects of the above factors on the m/e and B relationship become quite severe. However, in these application, rapid scans were not necessary. Since the saturation, Eddy Currents and hysterisis effects are quite reproducible with slow magnetic field scanning, and because an accuracy of approximately a tenth of a mass unit was sufficient for these studies, an occasional calibration run with a known substance was all that was required to minimize error in mass assignments with the present mass-readout system.

2.9 Ion Detection and Data Collection

The ions, after magnetic mass analysis, were further collima[illegible] using an adjustable slit located at the bottom end of the flight tube, and then detected with an ion counting system. Ion counting was obtained by utilization of a channeltron electron multiplier (CEM 4830), purchased from Galileo Electron-Optics Corp.. The CEM was installed in the ion detection housing of the ATLAS, replacing the 16-stage copper-beryllium secondary electron multiplier available from the original setup (45). The potential divider associated with the exsisting Cu-Be multiplier was modified in order to meet the operational requirements of the channeltron.

The channeltron electron multiplier is superior to the conventional Cu-Be in a number of ways: it has a stable dynode surface that can be exposed to air without degradation, it has higher gain stability , and also has a minimal gain dependancy on ion mass (60). In addition, other factors associated with the detector and amplification efficiency of Cu-Be multipliers, such as ion velocity (49, page 214) and chemical composition of the ions (61), are not a problem with channeltrons when the pulse counting method is employed for ion detection. The channeltron was so operated that a pulse of about 10^6 electrons per input ion (gain) was delivered to the pulse amplifier. With a new channeltron, this necessitated a voltage of 1.8 kV across the multiplier, which also corresponded to the manufacturer's specifications. The output pulses, according to the manufacturer were of extremely narrow width (approximately 3 nsec), and of fairly uniform size. This has been attributed to space charge saturation of the pulse of electrons as it moves through the tube of the multiplier (62). This is also to be contrasted with multipliers of the conventional dynode structure whose output pulses are of rather variable height. The uniformity in pulse heights allows one to set up a gate in the amplifier discriminator such that only signal pulses are accepted while the low level noises are rejected.

The output negative pulses from the multiplier were amplified further by an amplifier before being counted. The pulse amplifier used was the SSR Model 1120 amplifier/ discriminator from Princeton Research Corp. It had a rise time of 6 x 10^{-9} sec and a minimum gain of 2300. The amplifier/discriminator was designed to permit the resolution of electron pulses separated by as little as 10^{-8} sec, with sufficient sensitivity to detect individual secondary pulses representing less than 10^6 electron charges. The discriminator sensitivity had a range of 25 mV to 250 mV, and it allowed the setting of a gate level such that only the signal pulses were transmitted while the low level noise pulses were rejected. The amplifier/ discriminator could be used for counting rates up to 10^7 per second. This resolution was sufficient for the present system as the typical signal rate was only about 10^4 per second. The output pulses from the amplifier/discriminator were fed into the SSR Model 1127 NIM adapter (from Princeton Research Corp.) which converted the discriminated pulses into uniform 5 volt, 10 nsec pulses. The uniform pulses were counted either with an Ortec Model 441 ratemeter and displayed on a chart recorder or with a multichannel scaler (Nuclear Data 2200). The typical noise level observed was about 10 counts per sec.

Mass spectra (ion intensity vs. mass to charge ratio) were recorded on an XY chart recorder. The output of the ratemeter was fed into into the Y input of the recorder while the x axis was driven via the mass readout system.

The temporal fluctuation (time dependence) of an ion's intensity was observed and recorded with the multichannel scaler in the following manner. The start of the sweep of the multichannel scaler was synchronized with the triggering pulse of the electron gun (Figure 2.1). In a typical experiment, the dwell time per channel of the multichannel was set to be 10 μsec, and 256 channels were used. The number of ions arriving at the detector in the first 10 μsec after the triggering pulse were stored in the first channel. The number of ions that arrived from 10 to 20 μsec were stored in the second channel and so on for 256 channels. In this way, the change in ion intensity was followed for 2.56 msec. After a period of 3 msec the signal had decayed by a factor of 10^3 - 10^4 and the electron gun was pulsed again and the whole process repeated. This time the signal was added to that already stored in the multichannel scaler. The content per channel was accumulated for the specified period of the collection time. In most experiments, a collection time of 60 seconds per ion was found to be sufficient to afford a statistically meaningful temporal profile of the ion intensity. The time of observation of the ion concentrations was varied from 2.56 to 20.48 msec, depending on the requirements of the reaction system studied.

2.10 Sample Ionization Under Pulsed HPCI conditions.

Gas mixtures prepared in the gas handling system were passed in slow flow through the ion source. Ionization of the sample is accomplished by a short (approx. 10 to 60 μsec) pulse of 2000-3000 eV electrons which create some 10^7 ions and electrons in the thermostatically controlled HPCI source. Following the short electron pulse, rapid reactions in the major reagent gas, methane (which was maintained at some 2.5 to 6.5 Torr of the total pressure in the reaction zone), produce CH_5^+ and $C_2H_5^+$. These two ions because of their high acidity, proton transfer very rapidly to the other major components in the gas mixture (analyte (A) and reference base (B)), which are of considerably higher gas phase basicity. Protonation of species A and B is accomplished by the methane reactant ions, very shortly after the electron pulse, according to reactions 2.6 and 2.7.

$$CH_5^+ + B \rightleftharpoons BH^+ + CH_4 \qquad 2.6$$

$$C_2H_5^+ + B \rightleftharpoons BH^+ + C_2H_4 \qquad 2.7$$

Consequently, proton transfer between the protonated species and the neutrals proceeds according to ion molecule reaction 2.8.

$$BH^+ + A \rightleftharpoons AH^+ + B \qquad 2.8$$

The direction of the reaction depends on the gas phase basicity of the individual components A and B. Also, the rate (efficiency) of the proton transfer reaction, 2.8, depends on reaction temperature, exothermicity of the reaction, and site of protonation of the species involved. In the study of protonation of ferrocene in the gas phase (Chapter 4), it is illustrated how each of these factors may affect the rate of the above reaction with ferrocene being A.

By proper choice of the neutral reactant concentrations, reaction 2.8 can be controlled such that the ions AH^+ and BH^+ reach ion-molecule reaction equilibrium.

Pulsing of the electron beam permits one to follow the kinetics of the approach to equilibrium for the ions of interest. The relative concentrations of the ions of interest that are present in the HPCI source, right after the electron pulse, is obtained by mass analyzing the ion beam exiting the ion source and by recording the intensity of ions of different masses as a function of unit time. Multiscaler, time-resolved ion detection gives ion time dependence profiles which can be used for the evaluation of thermodynamic and kinetic parameters of proton transfer or other reaction systems.

2.11 Temporal Behavior of Ions and Treatment of Data.

A. Temporal Behavior of the Ions.

The temporal profile of positive ions involved in the ion-molecule reactions, 2.9 and 2.10, are shown in Figure 2.11.

$$(H_2O)_2H_3O^+ + H_2O \rightleftharpoons (H_2O)_3H_3O^+ \qquad 2.9$$

$$(H_2O)_3H_3O^+ + H_2O \rightleftharpoons (H_2O)_4H_3O^+ \qquad 2.10$$

These were obtained with a mixture of 3.10 Torr methane, 12.67 mTorr water, and 0.005 mTorr CCl_4 (electron scavenger) in the ion source at 310 K. Small concentrations of CCl_4 (fraction of a mTorr) were added to all gas mixtures studied, in order to avoid disturbance of the temporal profile of the ions investigated due to ambipolar diffusion (63, p. 512- 513, 64). Figure 2.11 gives a plot of the

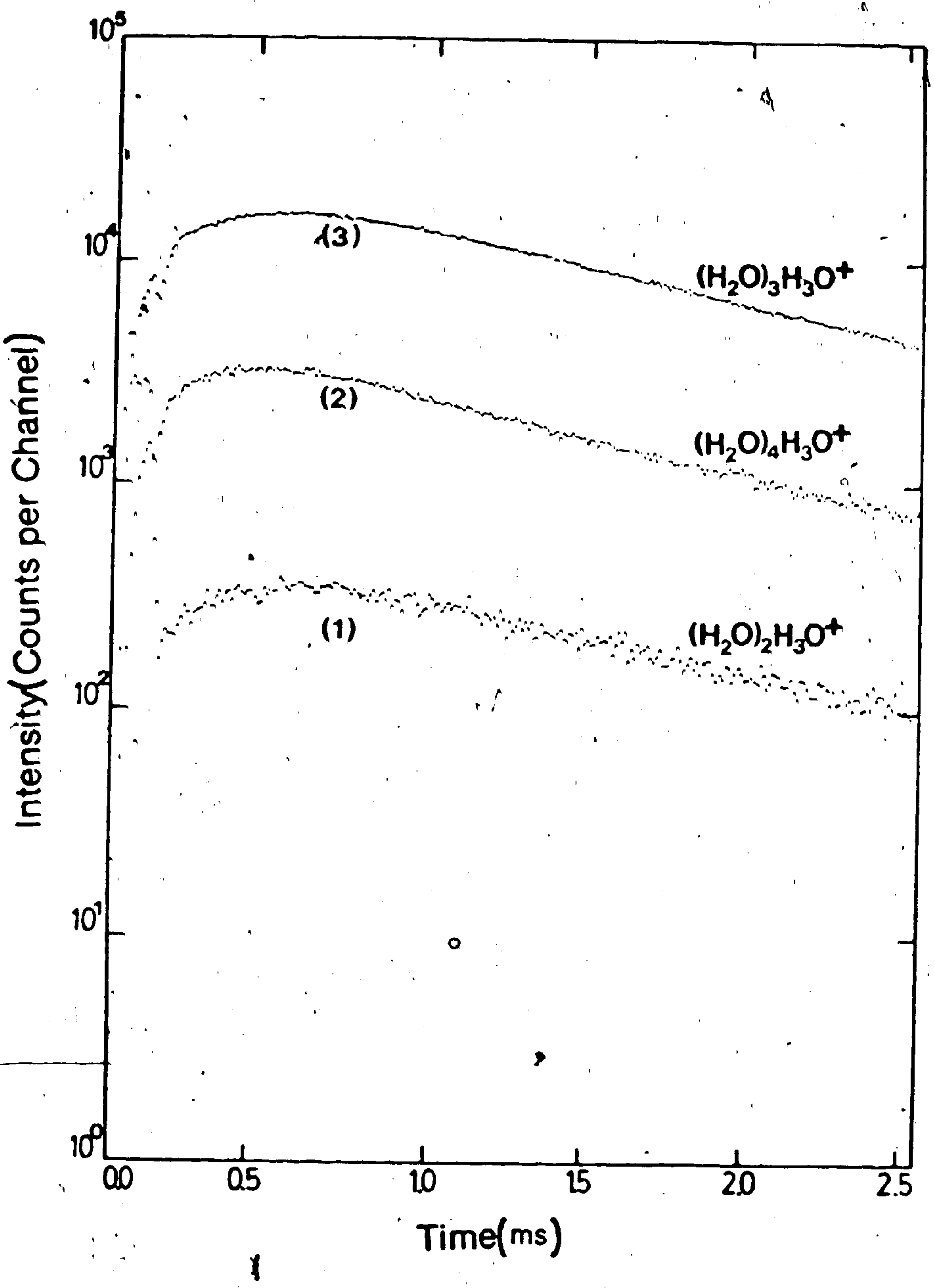

Figure 2.11. Time Dependence of Ion Intensities. Gaseous Mixture in the Ion Source: CH_4 ~~at~~ 3.10 Torr, H_2O at 12.67 mTorr. Source Temperature = 310 K.

logarithm of counts per channel against the time after the electron pulse. The relative intensities of the ions can be regarded as the same as their relative concentrations in the ion source. Since the concentration of water was constant in the ion source, the establishment of equilibrium is indicated by the invariance of relative ion intensities with time. This stage is achieved after some 500 μsec as shown in Figure 2.11 and lasts over the remaining time of the observation. The invariance of relative ion intensities between the two ions shows up as two parallel lines and the measured equilibrium ion intensity ratio can be determined by the vertical distance between two lines corresponding to ions of a specific equilibrium reaction, i.e. line 1 and 3 for evaluating equilibrium constant for reaction 2.9.

In all experiments conducted, the data recorded during the first 100 μsec after the electron pulse was not used in any calculations because the electron beam was still on and ions were still being created. This can be observed in all time dependence ion profiles reported throughout this thesis.

When the equilibrium concentrations of the neutrals and the ions are available from experimental measurements, then one can evaluate the equilibrium constant for a given ion-molecule reaction system. Furthermore, determination of the equilibrium constant at a single temperature allows one to evaluate the free energy change (ΔG^{o}) of the particular system by utilization of the Gibbs free energy equation

($\Delta G^o = -RT\ln K_{eq}$). Van't Hoff plots of the temperature dependence of the equilibrium constant, measured at different temperatures, lead to the evaluation of the enthalpy change (ΔH^o) and entropy change (ΔS^o) of the system under investigation. A detailed procedure for evaluating equilibrium constants and the thermodynamic quantities associated with them (ΔG^o, ΔH^o, and ΔS^o) is given in Chapter 4 (section 4.3A) for the acetophenone/ferrocene system.

Data sets of the type given in Figure 2.11 have been utilized in this laboratory to measure ion-molecule equilibria, involving a large variety of reaction types and leading to the ion thermochemistry for many different classes of ions (47,65).

B. Normalization of the Data.

As can be seen from Figure 2.11, the total ion intensity varies with time. To facilitate data analysis, in most cases, the ion intensities are "normalized". The normalization procedure involves expressing the ion intensity of a given ion at a given time, t, as the percentage of the total ion intensity at time t (66). Thus, the normalized ion intensities appear as if they represented ion changes in an ion source in which the total number of ions remained constant. Without this simplification, it is almost impossible to analyze the experimental data for kinetic parameters. This assumption is not involved in the determination of equilibrium constants since logarithmic ion profiles are sufficient for their evaluation.

Normalization of data was performed by a pdp 8/F (Digital Equipment Corporation) computer, which had been appropriately programmed in order to provide the normalization. Data from the multiscaler were transferred to the computer via an analog to digital converter, after the end of each experiment. Normalized time dependence ion intensities were displayed on an X,Y chart recorder, which was coupled to the pdp 8/F via a DAC. A number of different approaches could be applied to evaluate kinetic parameters, from the normalized data, depending on the reaction systems studied. Some of these approaches, which were used in the protonation of ferrocene study are outlined in Chapter 4.

The normalization procedure involves some approximations, however. It is assumed that all loss mechanisms, other than ion-molecule reactions i:e. charge particle recombination and diffusion affect all ions equally. Charge particle recombination phenomena, in the HPCI source are a negligible loss mechanism and this has been shown by Payzant (67). Diffusion is not a negligible process but the normalization procedure assumes that the diffusion coefficients for all ions are equal. This is incorrect as diffusion coefficients are dependent on mass as given below (63, page 435)

$$D \propto (1/\mu)^{1/2} \qquad 2.11$$

where μ is the reduced mass of the ion and neutral gas molecules. Diffusion coefficients are probably not greatly different for the ions which were studied in the present experiments (63, page 435).

In most of the experiments, in the present study, the rate of depletion of a particular ion by ion-molecule reactions is much faster than the rate of loss by diffusion. Thus diffusion, in many cases, is a minor contribution to the all over loss frequency when compared to ion-molecule reactions. It is concluded that the normalization procedure does not introduce serious error into the experimental results.

CHAPTER 3

ASSESSMENT OF THE INSTRUMENTS OPERATION

3.1 Physical Conditions of the HPCI Source.

Even though significant modifications were applied to the classical Kebarle HPCI source design in order to interface to it the direct solid sample inlet system and the electron gun, it was of major importance to keep the geometry of the reaction zone of the source in line with the classical design. Most of the parameters associated with the geometry of the reaction zone, i.e. position and dimensions of the electron entrance and ion exit slits, dimensions and temperature control of the reaction zone, operating pressure range, have been individually investigated and optimum conditions for these parameters have been established over the years in Dr. Kebarle's laboratory. These parameters have been shown to have important effects on ion formation, number of ion-molecule collisions in the source, removal of positive ions via diffusion to the wall and/or via ion-electron recombination, and ion sampling.

A number of systematic studies have been performed (55, 68-71) to show the significance of the size of the ion exit slit on sampling ions from a high pressure source. Also, a thorough discussion on the effects of the above parameters on the number of the ion molecule collisions in the source, ion removal, and the effect of ion-electron ambipolar diffusion on the temporal behavior of ions, can be found in reference (64).

Since the geometry and the dimensions of the reaction zone, of the present source, were not altered from the classical design, there was no need to conduct further experiments for establishing "new" conditions for the above mentioned parameters.

3.2 Performance of the HPCI Source with the Conventional Sample Introduction System Under Pulsed Electron Beam Environments.

A. Introduction

Since the instrument had been modified considerably from its original arrangement, and equipped with a new ion source, new electron gun (see Figure 2.4), and new gas handling system, it was planned to check the performance of all these new components, prior to performing further developments, i.e. interfacing the HPCI source to a direct solid sample introduction system.

It was of major importance to examine the instrument's capabilities in conducting time resolved HPCI studies. Therefore, the apparatus was tested by studying the ion-molecule reactions, leading to hydration of water in the gas phase, equation 3.1. This particular system was chosen because it has been well documented in the literature, thus giving us reliable data for comparative studies.

$$(H_2O)_{n-1}H_3O^+ + H_2O \rightleftharpoons (H_2O)_nH_3O^+ \qquad 3.1$$

Thermodynamic and kinetic parameters associated with the above reaction, for n=1 to 6, have been experimentally measured in this (72-74) and other laboratories (75,76). An extensive study of the temperature dependence of the equilibrium constants $K_{n-1,n}$ (n=3 to 6) for reactions 3.1, has been performed by Lau et al (77), who also give a summary of, and comparison with all the previously obtained results. In the present investigation, the hydronium ion equilibria for n=2,3,4 were studied, and the resulting equilibrium constants were compared to those reported by Lau et al.

B. Experimental

All the instrumental components and the experimental procedures utilized for time resolved HPCI studies with the conventional source design, and the conventional sample introduction system are outlined in detail in Chapter 2.

The gas mixtures, CH_4/H_2O, were prepared in the thermostated 5 L glass bulb of the GHS by filling the bulb with CH_4 to near atmospheric pressure and injecting liquid H_2O with a graduated syringe. The gas mixture was circulated through the HPCI source, at a flow rate considerably higher than the outflow through the ion source exit slits. The concentration of H_2O in the ion source was chosen to be sufficiently high so that the approach to equilibrium, was short (less than approximately 0.4 msec). This generally happened for $P(H_2O)$ in the 5 to 15 mTorr range. The ion source was operated at pressures between 2.0 and 4.5 Torr.

Temporal ion profiles were obtained by operating the system in pulsed electron mode, and the variation of intensity of the ion beams of interest was monitored by the multichannel scaler. Electron beam pulses applied were in the range of 10 to 30 μsec, depending on the equilibrium studied.

~~Logarith~~mic time dependence ion profiles were used for evaluating equilibrium constants. The variation of intensity of the major ions observed in a mixture of 12.67 mTorr H_2O in 3.10 Torr CH_4 at an ion source temperature of 310 K, is shown in Figure 2.11. This represents a set of typical data used to evaluate equilibrium constants for clustering equilibria for n=3,4 in reaction 3.1.

Equilibrium constants for the van't Hoff plots were determined in the conventional way, i.e. using a given reaction mixture with a fixed concentration of H_2O and gradually changing the reaction temperature.

C. Results and Discussion

The equilibrium constant for the solvation reaction, 3.1, can be denoted by K_{eq} (n-1,n) for the addition of the nth solvent molecule to the cluster. The K_{eq} (n-1,n) values were evaluated with equation 3.2, substituting $I_{(n)}/I_{(n-1)}$ for the observed equilibrium intensities for

$$K_{eq}\ (n-1,n) = I_{(n)}/I_{(n-1)}P \qquad 3.2$$

$H_3O^+(H_2O)_n$ and $H_3O^+(H_2O)_{n-1}$ respectively, and P is the water pressure.

An example of the equilibrium determinations is given in Figure 3.1. Shown are the experimentally determined equilibrium constants (K_{eq} determined via equation 3.2) at different constant temperatures for the n=3 clustering equilibrium. The invariance in equilibrium constant while varying the water pressure by a factor of approx. 6, at seven different reaction temperatures, is well illustrated in this Figure. The results of $K_{eq(n-1,n)}$ given in Figure 3.1 are typical, also for all the other equilibrium constant determinations.

Van't Hoff plots of the data from Figure 3.1 and similar data for the other equilibria measured in the present work are shown in Figure 3.2. The solid lines, in the Figure, indicate the results obtained by Lau et.al. (77) while the

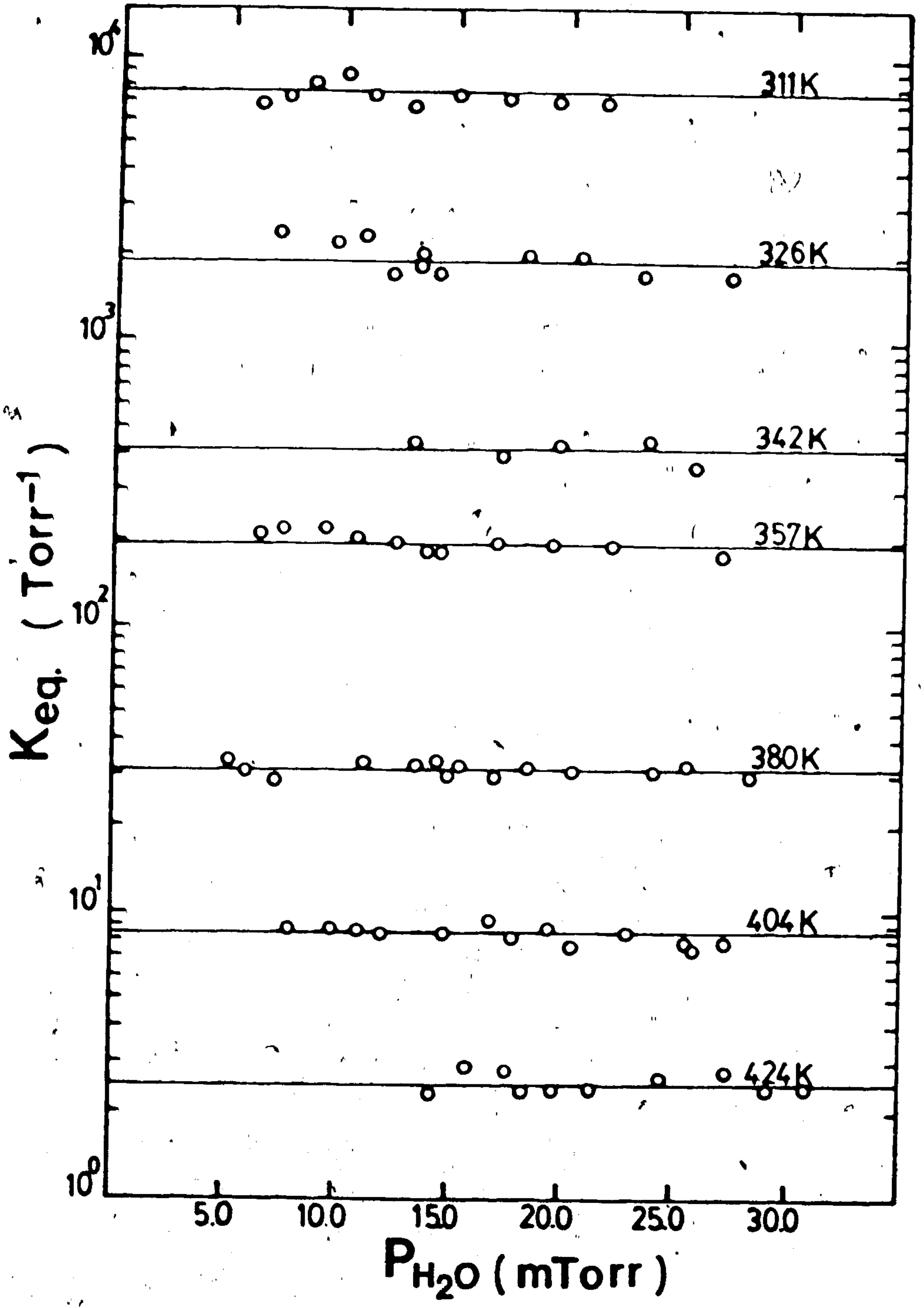

Figure 3.1. Measured equilibrium constants (K_{eq}) for the equilibrium $(H_2O)_2H_3O^+ + H_2O \rightleftharpoons (H_2O)_3H_3O^+$. Mixtures of the major gas methane containing the partial pressures of water shown on the abscissa were used. Reaction temperatures are given next to the lines.

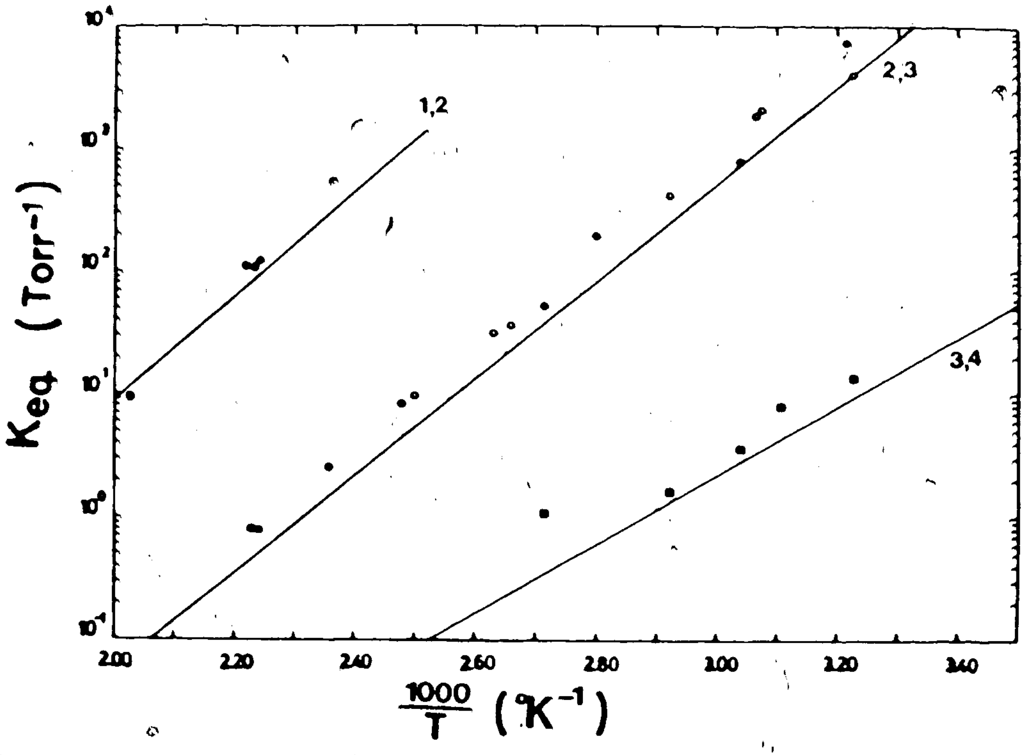

Figure 3.2. Van't Hoff plots for reactions $(H_2O)_{n-1}H_3O^+ + H_2O \rightleftharpoons (H_2O)_nH_3O^+$ with n=1,2,3. Solid lines indicate results obtained by Lau (77) while all data points are from the present work.

experimental points obtained from the present study lie next to the lines.

A least squares analysis was applied to the data of the n=3 clustering equilibria, and the resulting plot is shown in Figure 3.3. The change in enthalpy of this reaction was obtained by setting the slope of the line, in Figure 3.3, equal to $-\Delta H^{o}/2.303R$, while the change in entropy was calculated by setting the intercept equal to $\Delta S^{o}/2.303R$.

Equation 3.2 gave K_{eq} in Torr^{-1}, i.e. the standard state was 1 Torr. To get ΔS^{o} in units based upon one atmosphere, as the standard state, K_{eq} in Torr^{-1} was multiplied by 760 Torr atm^{-1}. Since ΔH^{o} is taken from the slope, the units of K_{eq} do not effect its units.

From Figure 3.3, the following values were obtained, $\underline{\Delta H^{o}}=-\underline{18.2}\ \underline{\pm}\ \underline{0.4\ \text{kcal mol}}^{-1}$, $\underline{\Delta S^{o}}=-\underline{28.1}\ \underline{\pm}\ \underline{1.1\ \text{cal mol}}^{-1}\ \underline{K}^{-1}$. These are in excellent agreement to those obtained by Lau(77) (ΔH^{o}[illegible]-17.9 kcal mol^{-1}, $\Delta S^{o}=-28.4$ $\text{cal mol}^{-1}\ K^{-1}$).

The experimental procedures for obtaining the above results were straightforward and free from any apparent complications. Since the results obtained, when the instrument (containing all the previously mentioned new components) was tested, proved satisfactory, this allowed us to proceed with further modifications as originally intended.

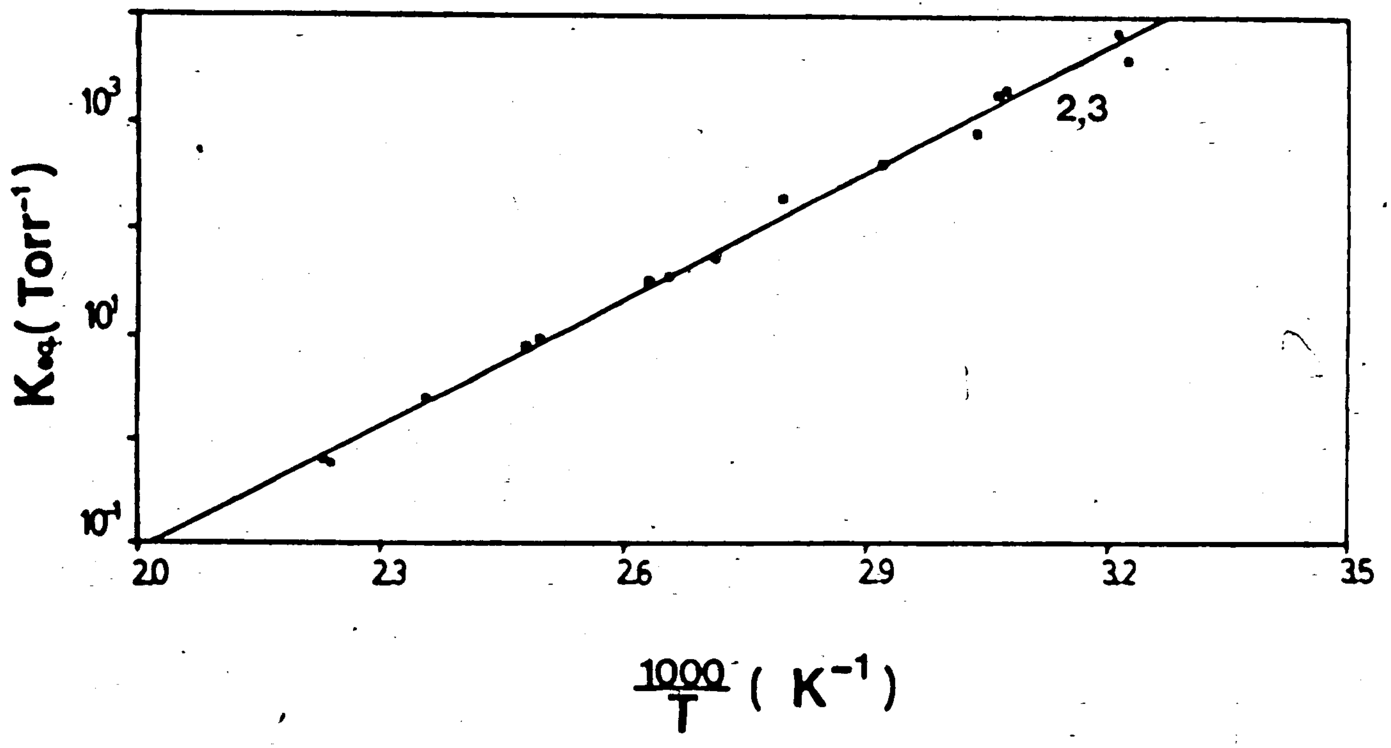

Figure 3.3. Van't Hoff plot resulting from least squares analysis of the experimentally obtained data for the clustering equilibrium reaction: $(H_2O)_2H_3O^+ + H_2O \rightleftharpoons (H_2O)_3H_3O^+$. These points are also indicated in Figure 3.2. designated by (o).

3.3 Performance of the Direct Solid Sample Introduction System Operated in Line With the HPCI Source.

A. HPCI Mass Spectra of Glycine, Leucine, and D-(+)-Galactose

After the direct solid sample inlet system had been interfaced to the HPCI source (see Chapter 2), the performance of the system in mass analyzing low volatility compounds was to be explored. Initially, it was intended to use the DIP only for qualitative investigations and then explore its quantitative capabilities.

Samples of biomolecules with low vapor pressures, specifically α-amino acids (glycine, leucine) and monosacharides (D-(+)-galactose) were chosen for the present investigation. Amino acids, in particular, as solids have low vapor pressures and decompose at temperatures above 300°C (78). The samples of interest, without any prior preparation were introduced directly into the reaction zone of the HPCI source by utilization of the DIP.

In Figure 3.4, are shown the HPCI mass spectra of glycine and leucine under pulse electron beam conditions, using methane as the reagent gas. Water impurity in the sample lead to peaks at m/e 19, 37, and 55. However, it was found that prolonged sample heating at an elevated probe temperature resulted in the elimination of these ions from the HPCI mass spectra. The effect of the latter is well

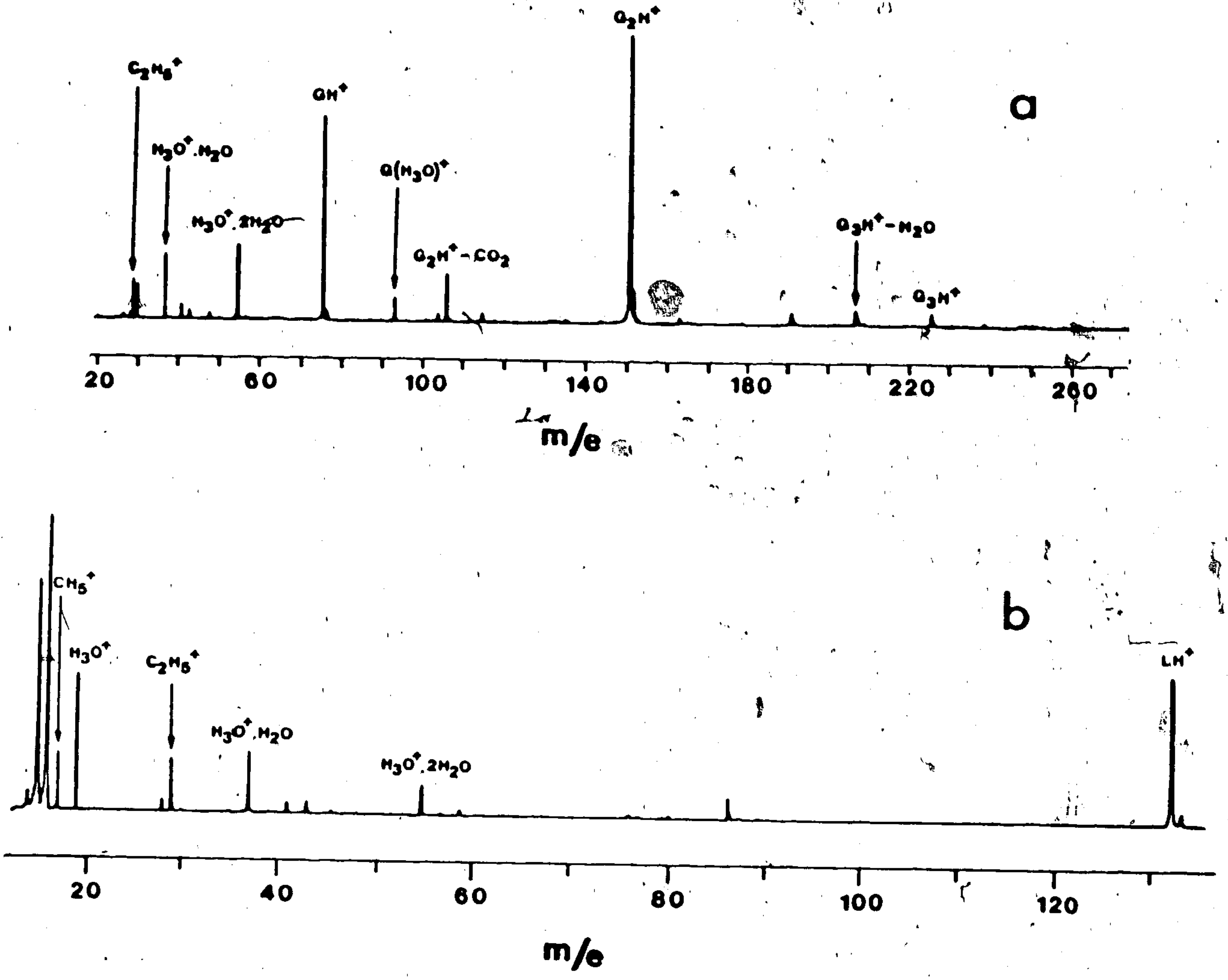

Figure 3.4. (a) HPCI mass spectrum of glycine, (G), with CH_4 being the reagent gas, and glycine being evaporated from the DIP, $T_{IS}=T_P=134^{o}C$, $P_{IS}=4.1$ Torr, max. sens. 10^4CPS, pulsing mode. (b) HPCI mass spectrum of leucine, (L), all of the above experimental conditions apply but in this case $P_{IS}=3.0$ Torr.

demonstrated in Figure 3.5, where the ions m/e 19, 37, 55 are reduced in intensity with increasing probe temperature (Tp). The spectra of both glycine and leucine are free of any apparent fragmentation of the parent ion, and the pseudo-molecular ion is present at relatively high abundances. However, a number of cluster ions, resulting from ion molecule reactions of the pseudo-molecular ion (GH^+) with neutral molecules G, were observed, particularly in the glycine spectrum, Figure 3.4A. Cluster ions are not unusual in HPCI mass spectra, especially with low ion source temperature and high analyte concentrations. Cluster formation is favored under high pressure environments since the products of exothermic ion-molecule reactions of the type $M_{n-1}H^+ + M \rightleftharpoons M_nH^+$ are stabilized through third body collisions in the HPCI source (65). The effect of elevated Tp (i.e. increase in the concentration of the neutrals) on cluster formation for the glycine system is illustrated in Figure 3.5. Formation of G_3H^+ is favored at higher glycine concentrations, while the GH^+ ion intensity is reduced considerably. This is due to participation of glycine in ion-molecule clustering reactions forming adduct ions G_2H^+ and G_3H^+. A similar trend is also observed with ions G_2H^+ and G_3H^+ (i.e. increase in G_3H^+ intensity at the expense of G_2H^+).

The HPCI mass spectrum of D-(+)-galactose under pulsed electron beam conditions using a methane/toluene(T) mixture as a reagent gas is shown in Figure 3.6.

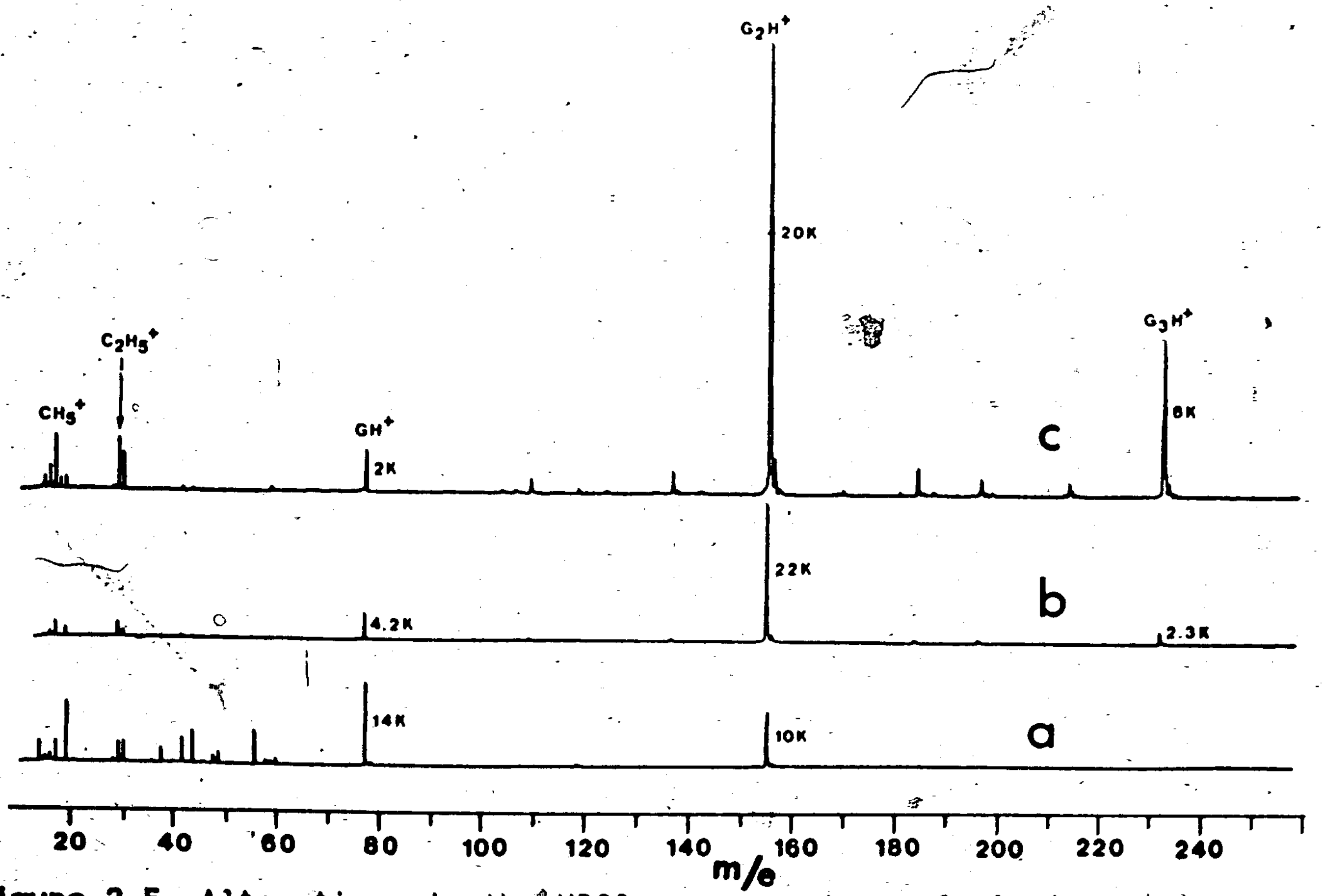

Figure 3.5. Alterations in the HPCI mass spectrum of glycine, (G), as a function of T_p. Going from (a) to (b) to (c), T_p had been increased from 146 to 170 to 187°C, while all other experimental conditions are kept constant: T_{IS}=131°C, P_{IS}=3.5 Torr, sensitivity is specified next to peaks in K=10^3CPS, pulsing mode with methane being the carrier gas.

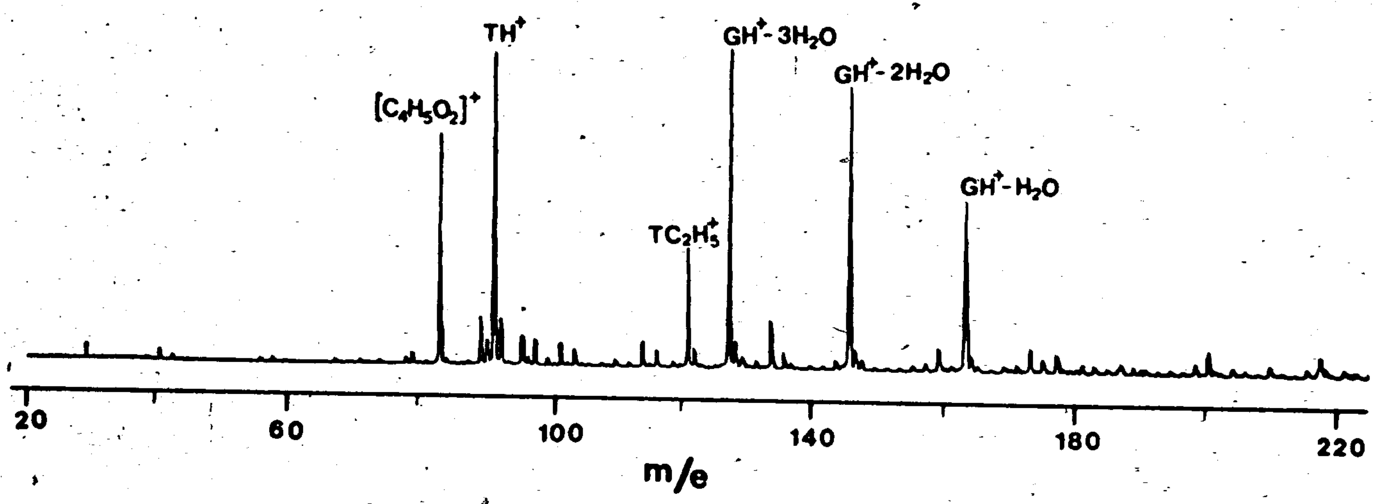

Figure 3.6. HPCI mass spectrum of D-(+)-galactose, (G), with a methane/toluene (T) mixture being the reagent gas and galactose being evaporated from the DIP. $T_{IS}=200^{\circ}C$, $T_p=178^{\circ}C$, $P_{IS}=2.45$ Torr, $P_{toluene}=2.27$ mTorr, max. sens. 10^4CPS, pulsing mode.

The methane/ toluene mixture was chosen in an attempt to ionize D-(+)-galactose through proton transfer, via a milder pathway, i.e. by utilizing protonated toluene as the reagent ion rather than CH_5^+ and $C_2H_5^+$ from methane. Since the proton affinity of toluene (PA = 189.8 Kcal mol^{-1}) is some 58.0 Kcal mol^{-1} higher than that of methane (23), the exothermicity of the proton transfer reaction to D-(+)-galactose from protonated toluene is much lower. Unfortunately, a reduction of the exothermicity of the proton transfer reaction by 58.00 Kcal mol^{-1} was not sufficient to suppress fragmentation. The D-(+)-galactose pseudo-molecular ion was still absent from the HPCI mass spectrum and the fragmentation pattern was unchanged. An identical fragmentation pattern of the D-(+)-galactose molecule was observed when neat methane or methane/acetone ($PA_{(acetone)}$ = 196.7 Kcal mol^{-1}) mixtures were used as reagent gases and all other experimental conditions were kept the same.

The fragmentation pattern of D-(+)- galactose shown in Figure 3.6 bears some resemblance to the one reported by Hogg, et. al. (79), obtained with methane at low pressure CI conditions. Hogg reported prominent peaks at (MH^+-H_2O), (MH^+-$2H_2O$), and (MH^+-$3H_2O$) with M being D-(+)-galactose, and at m/e 61,73,85. Prominent peaks at m/e 61 and 73 were not observed in the present investigation and this can be attributed to the high pressure environment, which assists in stabilization of ions.

The fact that the fragmentation of the D-(+)-galactose pseudo-molecular ion in the methane/galactose and in the methane/toluene/galactose HPCI mass spectra is identical, indicates that the fragmentation is most probably due to D-(+)-galactose being thermally labile (pyrolyzes upon heating and only fragments are available for ionization) and not due to excess energy deposited on the molecule upon protonation. However, in order to confirm this, a study of the thermochemical properties of the D-(+)-galactose or of a homologous series including D-(+)-galactose would have been required. Such a study was not performed since it did not fall within the framework of this research.

B. Evaluation of Analyte Concentration in the HPCI Source by Utilizing Thermochemical Data. Dimerization of Glycine.

The determination of analyte concentration in the reaction zone of the HPCI source, for samples that are introduced into the source via the DIP is not a simple matter. Such determinations could be obtained with the time resolved technique by utilizing ion-molecule kinetic data. Glycine was chosen for the present investigation because this system has also been studied by Mautner et al (80), and thus comparable data was available.

The concentration of glycine (in molec. cm^{-3}) in the source was determined by a technique proposed by Mautner (80).

This technique is based on the measurement of the rate of protonation of glycine from chemical ionization reagent ion BH^+. In the present investigation, a methane/toluene gas mixture was used as the reagent gas and protonated toluene (TH^+) served as the CI reagent ion. Protonated toluene is formed via proton transfer reactions from methane reagent ions, since toluene has a higher proton affinity. In turn, TH^+ proton transfers to glycine (G) according to reaction 3.3.

$$TH^+ + G \longrightarrow GH^+ + T \qquad 3.3$$

A typical mass spectrum, which has resulted from a mixture of methane/toluene/glycine (evaporated from the CI probe) is given in Figure 3.7.

The rate of disappearance of TH^+ and of the appearance of GH^+ was followed experimentally by application of the time resolved technique. The temporal profiles of the major positive ions, resulting from the previously mentioned gas mixture, are shown in Figure 3.8. This plot gives the logarithm of the counts per channel, for each ion, against the time after the electron pulse. As is evident from the figure, ions GH^+ and G_2H^+ have reached equilibrium some 0.75 msec after the electron pulse.

Following the rate of disappearance of TH^+, the pseudo- first order rate constant ν for reaction 3.3 can be evaluated. The method for obtaining pseudo-first order rate

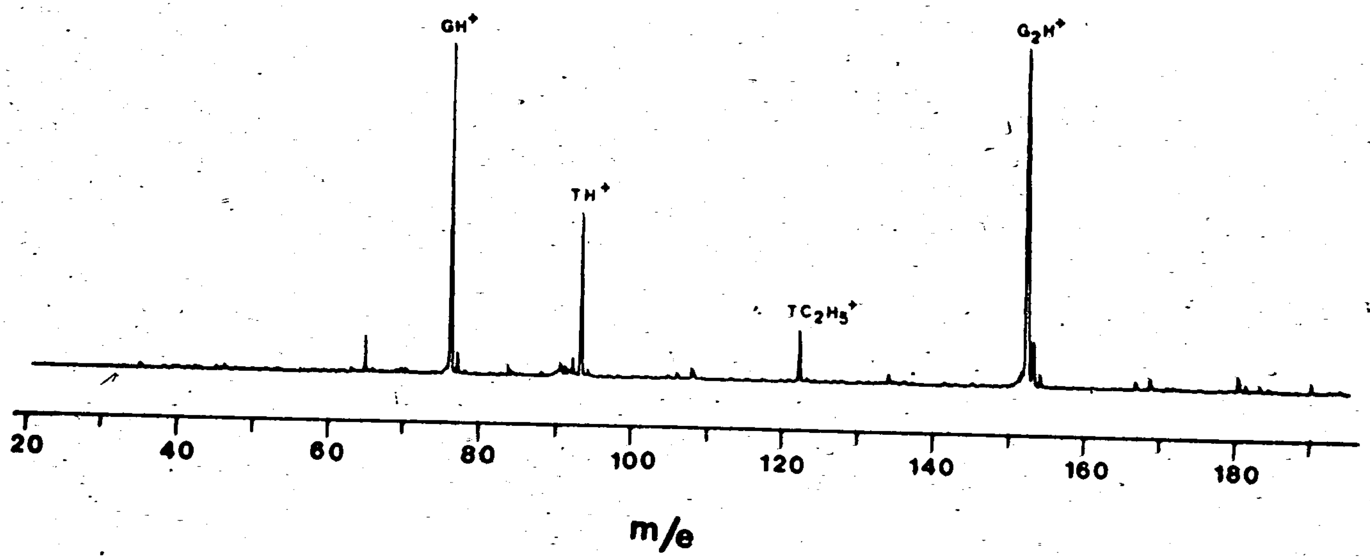

Figure 3.7, HPCI mass spectrum of glycine, (G), with a methane/toluene (T) mixture being the reagent gas. T_{IS}=197°C, T_p=180°C, P_{IS}=3.5 Torr, $P_{toluene}$=11.8 mTorr, max. sens. 10^3CPS, pulsing mode.

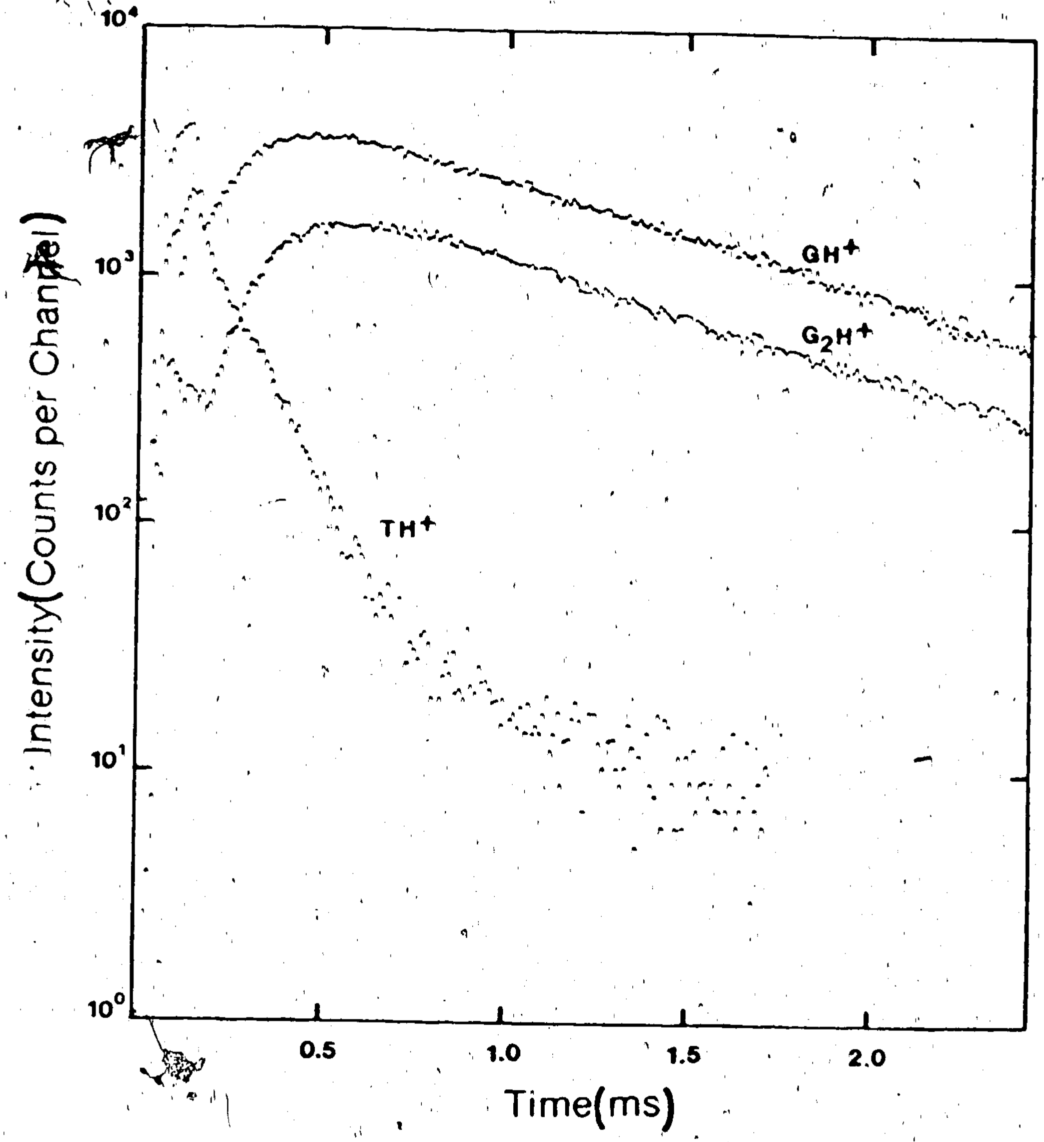

Figure 3.8. Plot of the logarithmic ion intensities versus time after the ionization pulse in a mixture of methane, 4.73 Torr, toluene, 1.29 mTorr, and with T_{IS}=227°C. From the rate of disappearance of the TH^+, a value of =5710 sec^{-1} was obtained which, in turn, was used to calculate $P_{glycine}$, 0.195 mTorr in this case.

constants from the data sets, similar to the one given in Figure 3.8, is outlined in detail in Chapter 4 section 4.4.1A of this thesis, for the benzene/ferrocene system. The concentration of the analyte molecule, glycine (G) in the present case, is related to ν by equation 3.4.

$$\nu = k_f[G] \tag{3.4}$$

k_f is the second order forward rate constant for reaction 3.3. This k_f value for the reaction of TH^+ with amino acids is not available, but it was assumed to be 1.5×10^{-9} $cm^3 \cdot sec^{-1}$ $molec.^{-1}$, which corresponds to a collision efficiency of approximately 1.0. Based on the available rate constant data, this value is almost certainly accurate to better than ± 50% (80).

So, at this point the concentration of glycine in the ion source could be obtained simply by evaluating the ν value for the proton transfer reaction 3[illegible]

Since the temperature of the CI probe could be varied independently from that of the source, the concentration of G in the source was controlled by the probe temperature. The probe temperature was set at values which produced concentrations of G such that ν was in the range of $5\text{-}50\times10^3$ s^{-1}. This is the observable range for ν with this method, and in turn, defines the measurable range of concentration of G. In general, the probe temperatures used to produce measurable concentrations of G were different from the source temperatures.

When the ion source was operated below 100°C and the probe temperature was kept at a temperature of 30° or higher, for prolonged periods of time, the ion signal intensity was found to decrease considerably. This was due to condensation of glycine on the inner walls of the ion source, and consequently on the slits. This caused ions to be trapped in the source since diffusion through the ion exit slit was prevented by the slits being blocked with a film of glycine molecules.

Once the concentration of glycine had been evaluated, by using the time dependence of ion intensities GH^+ and G_2H^+ reported in Figure 3.8, the equilibrium constant, K_{eq}, for the cluster reaction 3.5 could be evaluated

$$GH^+ + G \rightleftharpoons G_2H^+ \qquad 3.5$$

by application of the relationship $K_{eq}=I(G_2H^+)/I(GH^+)[G]$. The invariance of $\ln K_{eq}$ for reaction 3.5 with probe temperature (Tp) while keeping all other experimental conditions constant, is shown in Figure 3.9. The scattering of the points is within experimental error.

It is important to mention at this point that an attempt to obtain calibration curve(s) of Tp vs. glycine concentration proved unsatisfactory. This was attributed to the great number of variables involved:

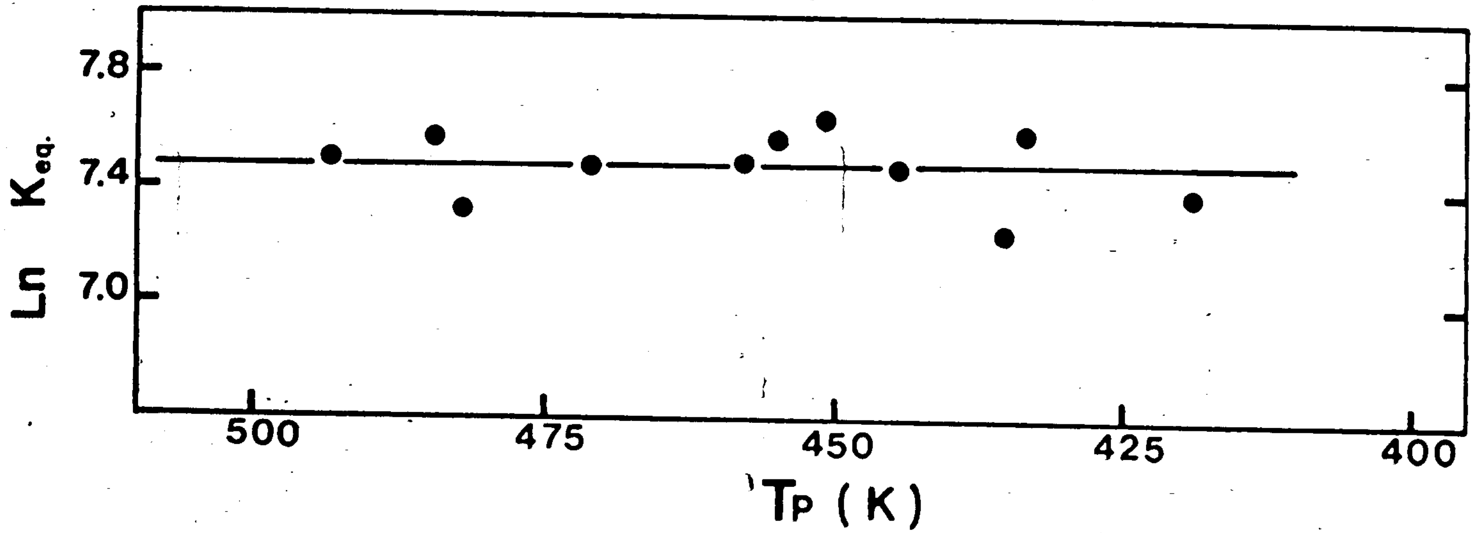

Figure 3.9. Equilibrium constant K_{eq} for the reaction: $GH^+ + G \rightleftharpoons G_2H^+$ at $T_{IS}=223^oC$. Equilibrium constant is independent of probe temperature. Reagent gas, CH_4.

source pressure, source temperature, heating and/or cooling rate of the probe, reagent gas temperature, surface area of sample exposed to reagent gas, period of time that the sample had been exposed at a specified Tp, and a number of others. However, all these factors are of no importance during a specific run since the concentration of the glycine was obtained directly from the ν value, which had resulted from the time dependence ion intensity of TH^+ during that specific run.

A van't Hoff plot corresponding to equation 3.5 was obtained in the conventional way and is shown in Figure 3.10. The solid line represents results from the present study, while the dashed line indicates results obtained by Mautner et al (80). The thermochemical quantities ΔH^o and ΔS^o, obtained from the van't Hoff plot of reaction 3.5, were in good agreement with those obtained by Mautner. In Table 3.1, are listed the ΔH^o and ΔS^o values of reaction 3.5 measured in this work and those reported by Mautner. ΔH^o and ΔS^o from the present work were obtained by applying a least squares analysis to the data reported in Figure 3.10. The resulting values of ΔH^o and ΔS^o were within the error limits quoted by Mautner (80).

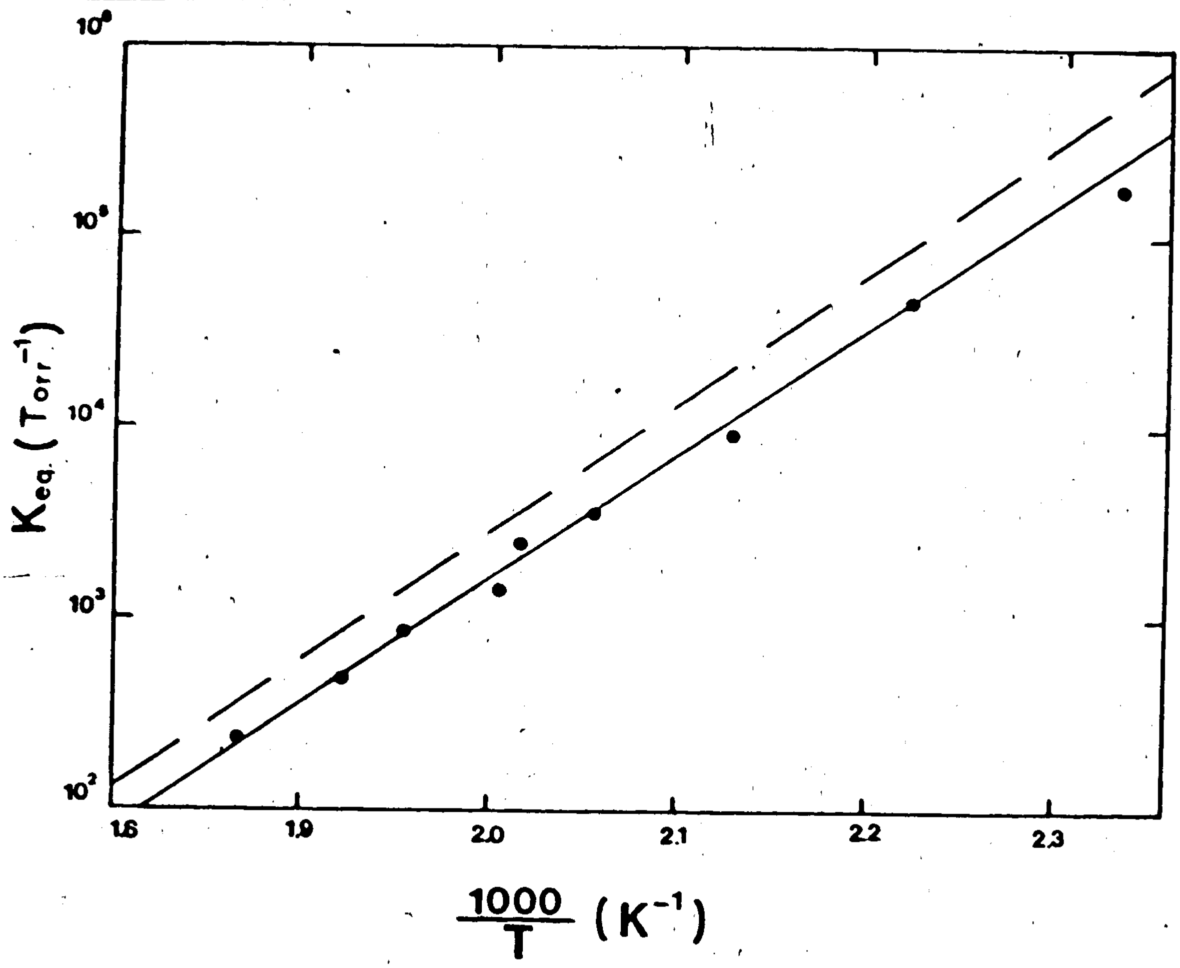

Figure 3.10. Van't Hoff plot for the clustering equilibrium: $GH^+ + G \rightleftharpoons G_2H^+$. Dashed lines correspond to measurements by Mautner (80); equilibrium constant obtained from the present study.

Table 3.1. Thermodynamic Data[a] for Ion-Molecule Reactions of Glycine and Aniline.

Reaction	$-\Delta H^o$ kcal/mol	$-\Delta S^o$ cal/mol K
$GH^+ + G \rightleftharpoons G_2H^+$	28.8 ± 0.7[b]	29.9 ± 1.4[b]
	31 ± 2[c]	33 ± 5[c]
$AH^+ + G \rightleftharpoons GH^+ + A$	0.2 ± 0.8[b]	-0.6 ± 1.7[b]
	0.0[c]	0.0[c]
$AH^+ + G \rightleftharpoons AGH^+$	27.7 ± 0.6[b]	30.2 ± 1.3[b]
$AH^+ + A \rightleftharpoons A_2H^+$	24.3 ± 0.6[b]	32.5 ± 1.4[b]

[a] All ΔH^o and ΔS^o values resulted from the present work were obtained by applying least squares analysis to the experimental data. [b] From the present work. [c] Reference 80.

C. Experimental Determination of the Proton Affinity of Glycine in the Gas Phase. The Significance of the Dual Bulb GHS in the Present Study.

In addition to obtaining thermodynamic data for clustering reactions, the determination of the concentration of analyte by the present method makes it possible to study, quantitatively, other ion-molecule processes, which can lead to an evaluation of proton affinity values for low volatility compounds.

The proton affinity of glycine has been thoroughly investigated by a number of authors (80-82) using both pulsed HPCI (80) and pulsed ICR mass spectrometry (81-82), and reliable values have been established (23).

In this work, the proton affinity of glycine was obtained from measurements of proton transfer equilibrium between glycine and the reference base aniline (A). Protonated aniline proton transfers to glycine according to reaction 3.6.

$$AH^+ + G \rightleftharpoons GH^+ + A \qquad 3.6$$

Known quantities of aniline were injected into the storage bulb of the GHS, which was already filled to atmospheric pressure with methane. Glycine was evaporated from the probe directly into the reaction zone of the source. A typical HPCI mass spectrum, resulting from a mixture of methane/aniline/glycine, is shown in Figure 3.11. Apart from the methane reagent ions and GH^+, AH^+, $AC_2H_5^+$, G_2H^+, G_3H^+ ions, whose formation has been previously described, the spectrum also exhibits prominent peaks at $G_2H^+-CO_2$, AGH^+, and A_2H^+. $G_2H^+-CO_2$ is just a fragment ion of G_2H^+, while AGH^+ and A_2H^+ are products of the ion-molecule association reactions 3.7 and 3.8, respectively.

$$AH^+ + G \rightleftharpoons AGH^+ \qquad 3.7$$

$$AH^+ + A \rightleftharpoons A_2H^+ \qquad 3.8$$

During a single run, the time dependence of the intensities of the ions AH^+, A_2H^+, AGH^+, GH^+, and G_2H^+ could be recorded. Once the glycine concentration had been evaluated, via the method previously described, the equilibrium constants for reactions 3.5-3.7 were evaluated with the known concentration of aniline in the conventional way, by utilizing a set of experimental data of the kind shown in Figure 3.12 and also by knowing the concentration of aniline. The particular set in Figure 3.12 was chosen to illustrate that equilibrium constants for more than one reaction could be obtained from a single experiment.

The equilibrium constants for reactions 3.6 to 3.8 were measured at a number of temperatures, and van't Hoff plots for all three systems were obtained (Figure 3.13). From these plots, the enthalpy and entropy change for each reaction was evaluated. The resulting values are summarized

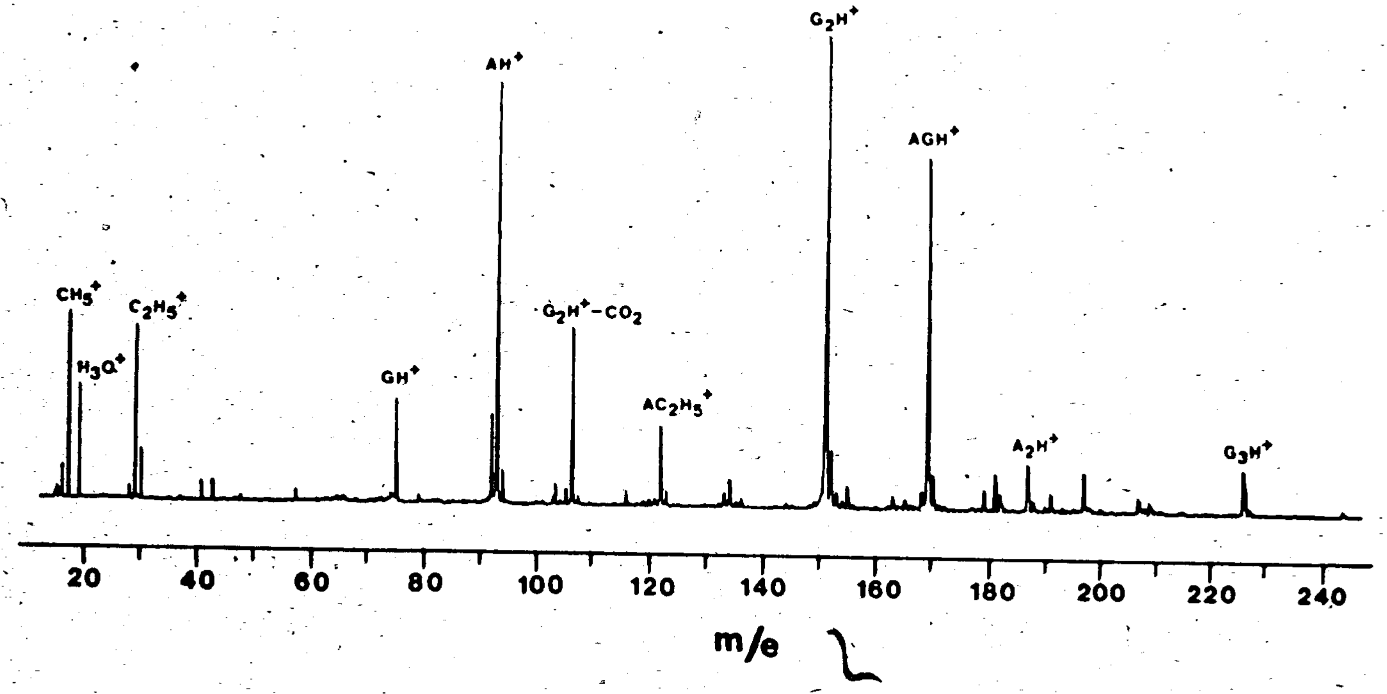

Figure 3.11. HPCI mass spectrum of glycine, (G), with a methane/aniline, (A), mixture being the reagent gas. $T_{IS}=T_P=132^oC$, $P_{IS}=4.0$ Torr, $P_{aniline}=5.92$ mTorr, max. sens. 10^4CPS, pulsing mode.

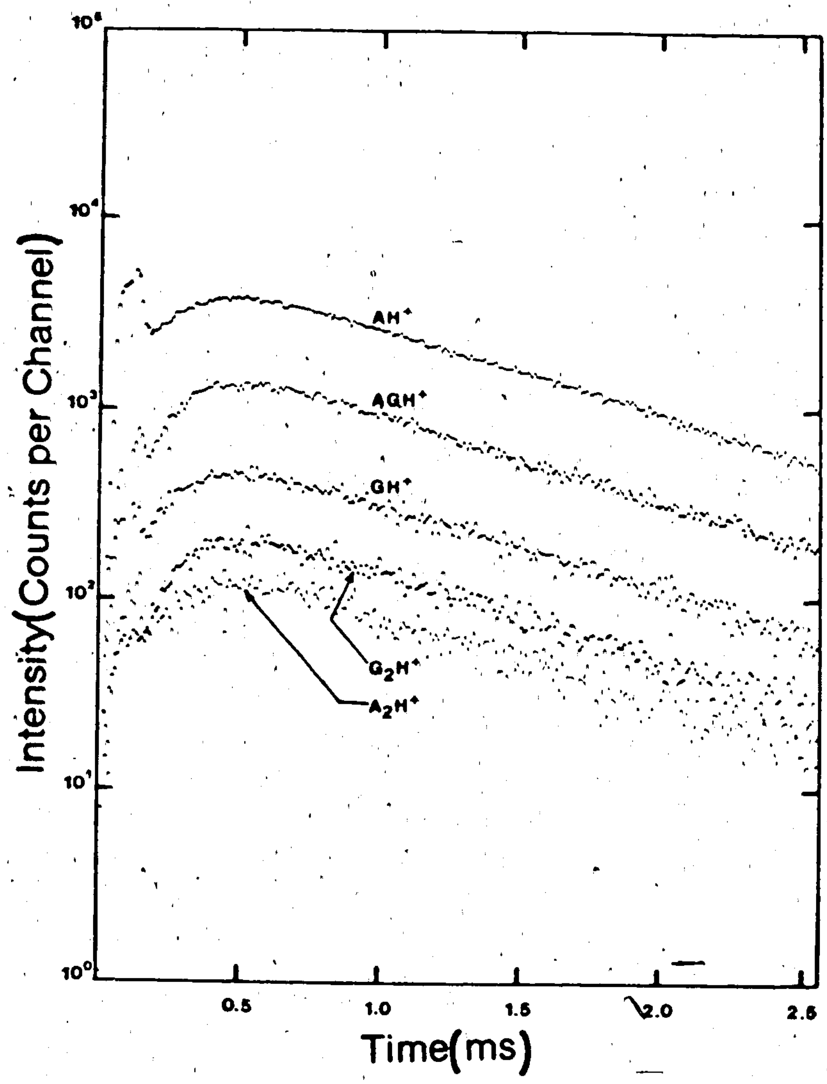

Figure 3.12. Plot of the logarithmic ion intensities versus time after the ionization pulse in a mixture of methane, 4.73 Torr, aniline, 3.24 mTorr, glycine, 0.195 mTorr, and T_{IS}=227°C. AGH^+ was collected for 60 sec, A_2H^+ for 40 sec, and all others for 20 sec.

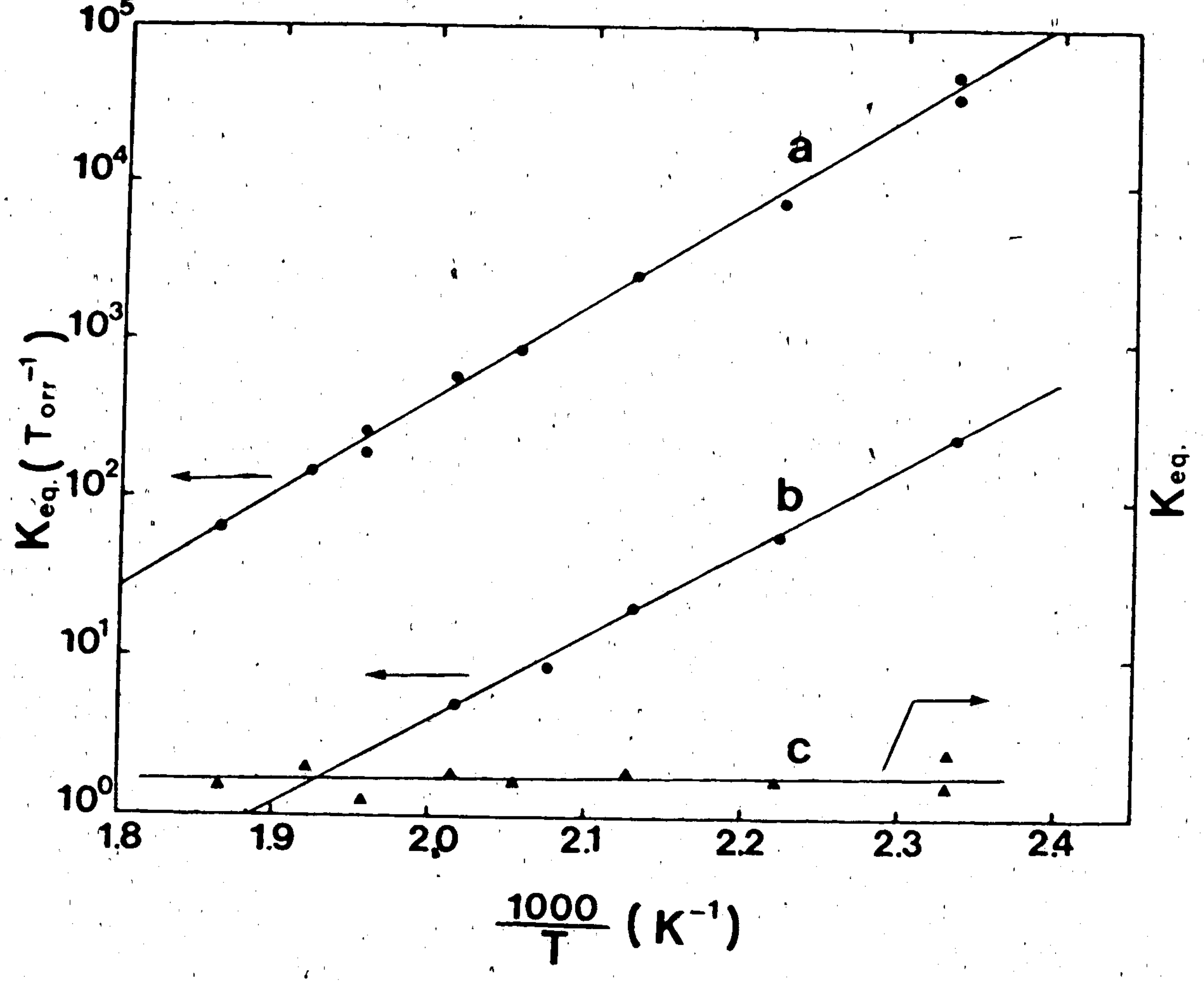

Figure 3.13. Van't Hoff plots for the equilibrium reactions: (a) $AH^+ + G \rightleftharpoons AGH^+$, (b) $AH^+ + A \rightleftharpoons A_2H^+$, and (c) $AH^+ + G \rightleftharpoons GH^+ + A$. Arrows specify the appropriate Y axis.

in Table 3.1. Combining the enthalpy change of the proton transfer equilibrium between aniline and glycine (0.2 kcal mol^{-1}) with the proton affinity of aniline (PA=209.5 kcal mol^{-1} (23)), a value of 210.1 kcal mol^{-1} is obtained for the proton affinity of glycine. This proton affinity value is within the error limit quoted by Mautner et al 208.8 ± 1.5 kcal mol^{-1} (80).

In order to obtain reliable thermodynamic data, for the reaction systems (3.5-3.8), when the direct solid sample inlet system was used, the following experimental conditions had to be followed during all experiments.

1. Bulb I of the GHS was always filled with a methane/toluene gas mixture, while bulb II was always filled with a methane/aniline mixture. In both bulbs, the concentration of toluene and aniline, respectively, were known accurately.
2. At first the methane/toluene gas mixture was passed slowly through the HPCI source at known pressures, in the 2.5 to 5.0 Torr range. While in single ion monitoring mode, the probe temperature was adjusted until an intense GH^+ peak was observed. In turn, a set of data of the type shown in Figure 3.8 was recorded, which allowed the evaluation of the concentration of glycine, [G], in the source.
3. Once satisfactory data for the evaluation of [G] had been recorded, the valve connecting bulb I to the GHS manifold was shut off and the valve connecting bulb II to

the manifold was opened slowly, after the manifold had been partially evacuated, say from 500 Torr down to 10 Torr. While keeping all experimental conditions constant, after a short waiting period, around 5 minutes (for gas mixtures of bulb II to reach the source and for P_{IS} to stabilize), a set of data of the type shown in Figure 3.11 was recorded.

4. In order to check for short term fluctuations of glycine concentration in the source during step 3, step 2 was repeated after each methane/aniline/glycine run. Also, during the aniline/glycine runs, if there was some fluctuation in [G] that would cause large changes in the glycine monomer/dimer equilibrium which was also monitored during these experiments. The equilibrium constants for the glycine monomer/dimer reaction served as a double check for [G] under conditions where the dimer was present and was also in equilibrium with the monomer.

The completed tests for the performance of the electron gun, pressure controls, temperature controls, and solid sample inlet system described above, demonstrate the ability of the system to provide thermodynamic data, with the time resolved HPCIMS. Since the results obtained were in agreement with determinations in the literature, one can now confidently utilize this instrument for studies involving low volatility compounds.

CHAPTER 4

THERMODYNAMICS AND KINETICS ASSOCIATED WITH THE PROTONATION OF FERROCENE IN THE GAS PHASE

4.1 Introduction

In recent years a number of exothermic bimolecular ion molecule reactions have been shown to be slow and to have a negative temperature dependence (83,84). Examples of slow proton transfer reactions include proton transfer to large delocalized anions (85) and sterically hindered proton transfer reactions (86). Some hydride transfer reactions, $R_1^+ + R_2H \rightleftharpoons R_1H + R_2^+$, are also known to be slow (87). Farneth and Brauman (85) found that for a large number of delocalized anions, protonation on a carbon atom was slow, whereas protonation on an oxygen atom was fast. The negative temperature dependence of these slow reactions has been explained by Brauman (85), with the assumption that a tight transition state is present in the reaction coordinate. In order to more firmly establish the physical explanation for the negative temperature dependence of these slow ion molecule reactions, it is important to obtain more kinetic data on different kinds of chemical systems. A better understanding of these processes will be of significant importance in improving the analytical capabilities of CI.

In CI the general assumption is made that when proton transfer from a reagent ion, BH^+, to the analyte is exothermic, it will lead to a fast process. Thus, the proton affinity of the analyte and the reagent, B, are taken as a guide to achieve exothermic protonation. Analytes for which the proton transfer, even though exothermic, is slow will be detected with reduced sensitivity and if the rate is exceedingly slow might not be detected at all.

It was of interest to examine the mechanism of gas phase proton transfer reactions involving organometallic compounds like ferrocene, and try to see to what extent the rate of protonation depends on ion source temperature, exothermicity and structure of the reacting species, and if the mechanism of protonation is similar to those of organic molecules.

Organometallic compounds were chosen for the following reason. There is a wide variety of organometallic compounds which are sufficiently thermally stable to be handled with the direct insertion probe. Thus, experiments with a series of organometallic compounds would represent a test of the capabilities of the DIP. Organometallic compounds are routinely identified with electron impact, EI, mass spectrometry while the capabilities of the CI method have been explored much less.

Foster and Beauchamp (88), have reported a value of 213 ± 4 kcal mol^{-1} for the proton affinity, PA, of ferrocene. The uncertainty in the value was rather large since only bracketing was used, i.e. the PA determination was based on whether proton transfer reactions with a number of reference bases was observed or not. Corderman and Beauchamp (89) subsequently published a value for the proton affinity of nickelocene, 218.9 ± 1.0 Kcal mol^{-1}. In contrast to the bracketing measurements for ferrocene, the more accurate proton affinity value for nickelocene was obtained by equilibria measurements. This indicated that proton transfer reactions involving ferrocene may be slow whereas the reactions with nickelocene are probably fast. However, the authors did not report any observations on the kinetics. The ferrocene self-exchange electron transfer reaction, has been shown to be slow (90).

There are other reasons for suspecting that proton-transfer reactions involving ferrocene may be slow. Infrared spectra obtained with solutions, have revealed that the rings of protonated ferrocene become tilted and that the iron-ring bonds are weakened upon protonation (91). Ion molecule reactions that involve large geometry changes of the reactants are often observed to be slow (92). Utilizing the PHPCI technique the present work describes measurements of the kinetics of gas phase proton transfer reactions from various reagent ions BH^+ to ferrocene, together with equilibria determinations of the proton affinity and the entropy of protonation of ferrocene.

4.2 Experimental

The apparatus used for the study of the protonation of ferrocene in the gas phase is described in detail in Chapter 2. The specially constructed DIP CI probe for introducing solid and low volatility samples directly into the HPCI source was used for most of the exploratory work in this study. However since the DIP could not be easily calibrated to deliver accurately known analyte concentrations, see Chapter 3, the quantitative measurements which required accurately known ferrocene concentrations were performed with a different sample introduction system (see Chapter 2, Section 2.5B). Fortunately, ferrocene has a sufficiently high vapour pressure (93) to be handled with the heated gas handling system, GHS (see Chapter 2). Ferrocene vapor was produced by dissolving suitable amounts of solid ferrocene in toluene or benzene, and injecting with a graduated syringe, predetermined amounts of solution of the known concentration, into the 5 L bulb of the thermostatically controlled gas handling system, GHS. The bulb contained 1 atm of reagent gas methane and about 0.005 mTorr CCl_4 (electron scavenger). The choice of concentration conditions for the different compounds used is related to the kinetics and the thermodynamic measurements that were encountered. However, typical partial pressure ranges used in the ion source were 0.01-10.0 mTorr for ferrocene and 0.5-15.0 mTorr for the reference base. The partial pressures of the individual compounds in the 5 L bulb after injection of a certain volume of known concentration were evaluated by utilizing the ideal gas law. The temperature of the GHS was set to 115^{o}C which was considered sufficient to ensure complete vaporization of the samples used. The gas mixtures were allowed to mix in the bulb for about 1/2 hour prior to introduction into the HPCI source.

Interfacing the GHS to the reaction zone of the HPCI source was accomplished with the all glass (quartz) heated CI probe (see chapter 2), via a short piece of teflon tubing (10 mm i.d.) connecting the low pressure side of the needle valve (valve regulating the gas flow from the GHS manifold) to the base of the probe. The teflon tubing and the inner tube of the probe were kept at the GHS temperature as to avoid sample condensation on its way to the reaction zone of the HPCI source. The gas mixture, with methane being the reagent gas in most ferrocene experiments was passed in slow flow through the ion source. Constant flow was maintained by means of adjusting the needle valve between the bulb and the ion source

Measurements for obtaining K_{eq} and k_F for reaction 4.1, with B being a reference base were performed as follows.

$$BH^{+} + (C_5H_5)_2Fe \underset{k_R}{\overset{k_F}{\rightleftharpoons}} (C_5H_5)_2FeH^{+} + B \qquad 4.1$$

The major reagent gas, methane, carried known partial pressures of reference base, B, and ferrocene into the reaction zone of the source. The ion source was operated at pressures between 2.5 and 6.5 Torr. Short electron pulses of 40 μsec duration caused primary ionization producing CH_5^+ and $C_2H_5^+$ as final ions in methane. Protonation of reference base, B, and ferrocene is accomplished from reagent ions CH_5^+ and $C_2H_5^+$, via proton transfer ion-molecule reactions. Then, proton exchange between the reference base and ferrocene follows according to equation 4.1. Multiscaler time-resolved ion detection (see chapter 2) resulted time dependence profiles of BH^+ and $(C_5H_5)_2FeH^+$, which were used for evaluating thermodynamic and kinetic parameters of reaction 4.1.

The time of observation of the ion concentrations varied from 2.56 to 10.24 msec after the electron pulse, depending on the reacting system studied.

For most of the experiments performed, only the two ions BH^+ and $(C_5H_5)_2FeH^+$ were collected and analyzed. Additional ions see Figures 4.1 to 4.4 were also observed. The presence of these ions, i.e. BCH_5^+, $BC_2H_5^+$, proton bound dimers B_2H^+ etc. led in some cases to interference with the measurements as outlined further in this Chapter.

Ferrocene and all the other chemicals used were obtained from commercial sources and were used as supplied. Ferrocene was purchased from Aldrich and was of 98% grade.

4.3 Equilibrium Measurements Leading to Gas Phase Basicity and Proton Affinity of Ferrocene

The gas phase basicity of ferrocene was obtained from studies of the gas phase proton transfer equilibria involving ferrocene and the reference bases: $C_6H_5COCH_3$, C_4H_5N, $(CH_3)_2NCHO$ (DMF), and $3\text{-}ClC_5H_4N$ (3-ClPy). Establishment of the equilibrium for the proton transfer reaction 4.2-4.5 was confirmed by monitoring the temporal profile of the positive ions involved in the particular ion-molecule equilibrium reaction.

$$[C_6H_5COHCH_3]^+ + (C_5H_5)_2Fe \rightleftharpoons (C_5H_5)_2FeH^+ + C_6H_5COCH_3 \tag{4.2}$$

$$C_4H_5NH^+ + (C_5H_5)_2Fe \rightleftharpoons (C_5H_5)_2FeH^+ + C_4H_5N \tag{4.3}$$

$$DMFH^+ + (C_5H_5)_2Fe \rightleftharpoons (C_5H_5)_2FeH^+ + DMF \tag{4.4}$$

$$3\text{-}ClPyH^+ + (C_5H_5)_2Fe \rightleftharpoons (C_5H_5)_2FeH^+ + 3\text{-}ClPy \tag{4.5}$$

Equilibria 4.3 and 4.4 were studied at a single temperature (500 K), whereas 4.2 and 4.5 were examined over a range of temperatures. Van't Hoff plots of the temperature dependence of K_2 and K_5 (equilibrium constants for reactions 4.2 and 4.5 respectively) permit the evaluation of the corresponding ΔH^o and ΔS^o changes. Typical HPCI mass spectra observed with the systems: $CH_4/C_6H_5COCH_3/(C_5H_5)_2Fe$, $CH_4/C_4H_5N/(C_5H_5)_2Fe$, $CH_4/DMF/(C_5H_5)_2Fe$, and $CH_4/H_2O/$ $3\text{-}ClPy/(C_5H_5)_2Fe$ mixtures under the specified reaction conditions are shown in Figures 4.1 to 4.4 respectively.

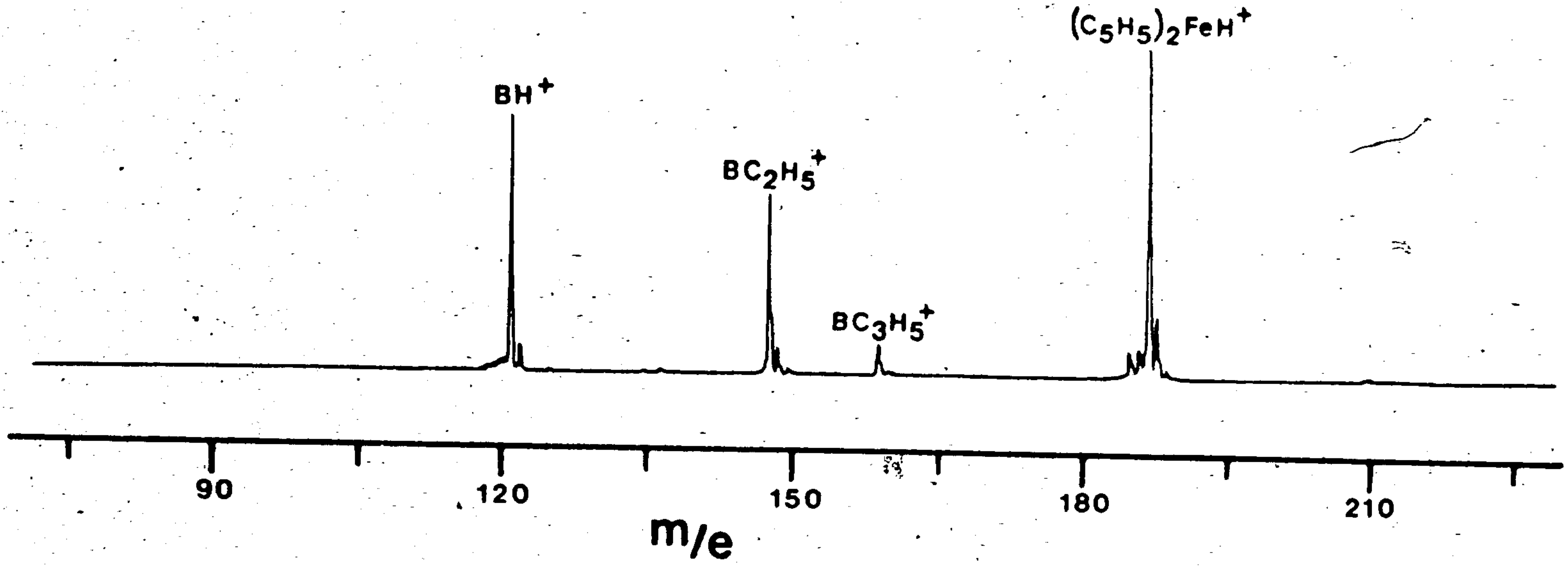

Figure 4.1. HPCI mass spectrum of a methane/B:acetophenone/ferrocene dissolved in toluene, mixture. Ion source conditions: T=480°K, P_{IS}=3.5 Torr, $P_{acetophenone}$ =4.1 mTorr, $P_{ferrocene}$=0.18 mTorr, and $P_{toluene}$=0.25 mTorr. Max. sens. 500 CPS, pulsing mode.

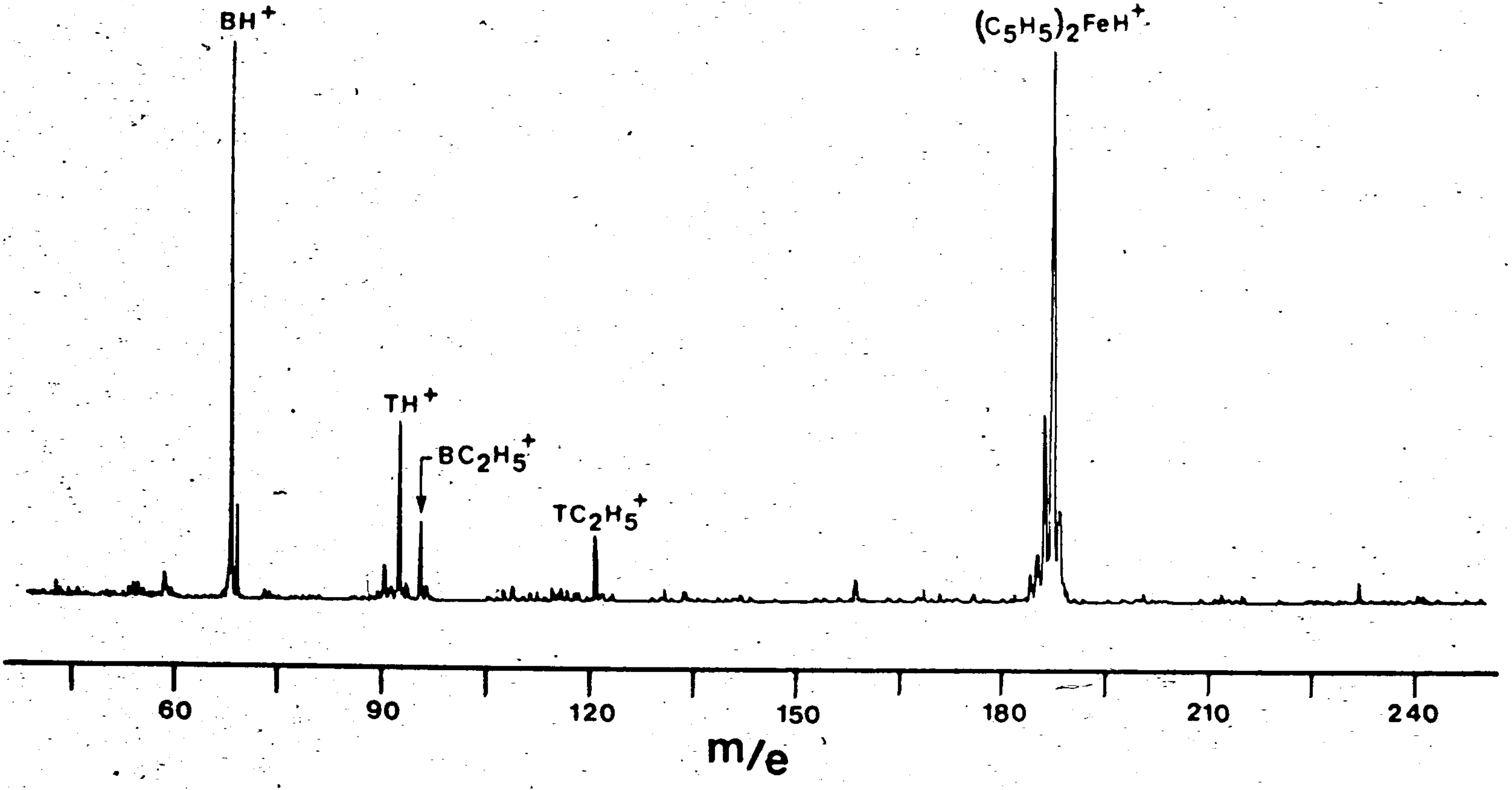

Figure 4.2. HPCI mass spectrum of a methane/B:pyrrole/ferrocene dissolved in toluene, mixture. Ion source conditions: T=455^{o}K, P_{IS}=3.0 Torr, $P_{pyrrole}$=1.2 mTorr, $P_{ferrocene}$=0.67 mTorr, and $P_{toluene}$=12.1 mTorr. Max. sens. 10^3CPS, pulsing mode.

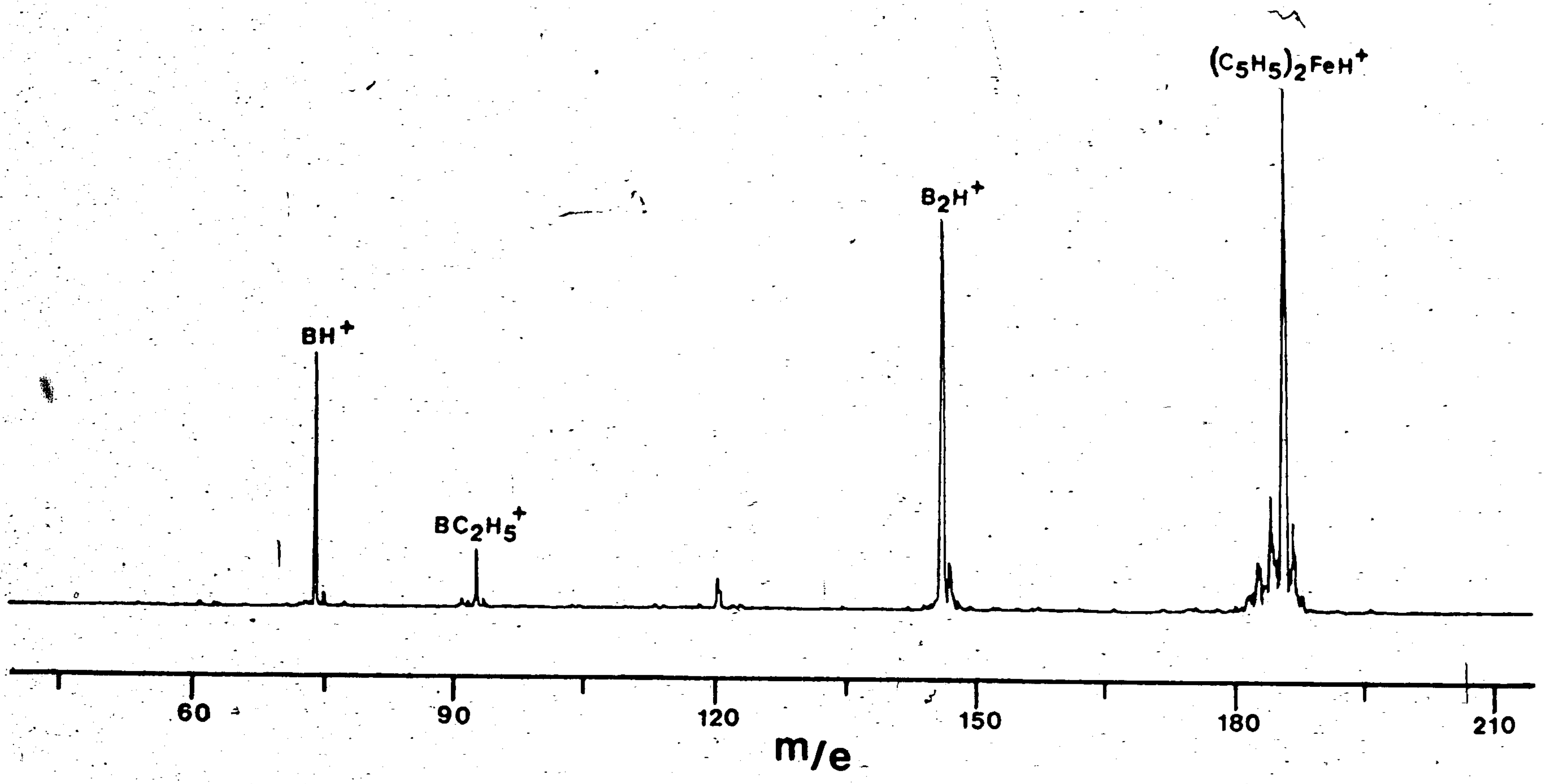

Figure 4.3. HPCI mass spectrum of a methane/B:DMF/ferrocene dissolved in toluene mixture. Ion source conditions: T=500°K, P_{IS}=3.4 Torr, P_{DMF}=0.15 mTorr, $P_{ferrocene}$=1.5 mTorr, $P_{toluene}$=25.6 mTorr. Max. sens. 5*10^3CPS, pulsing mode.

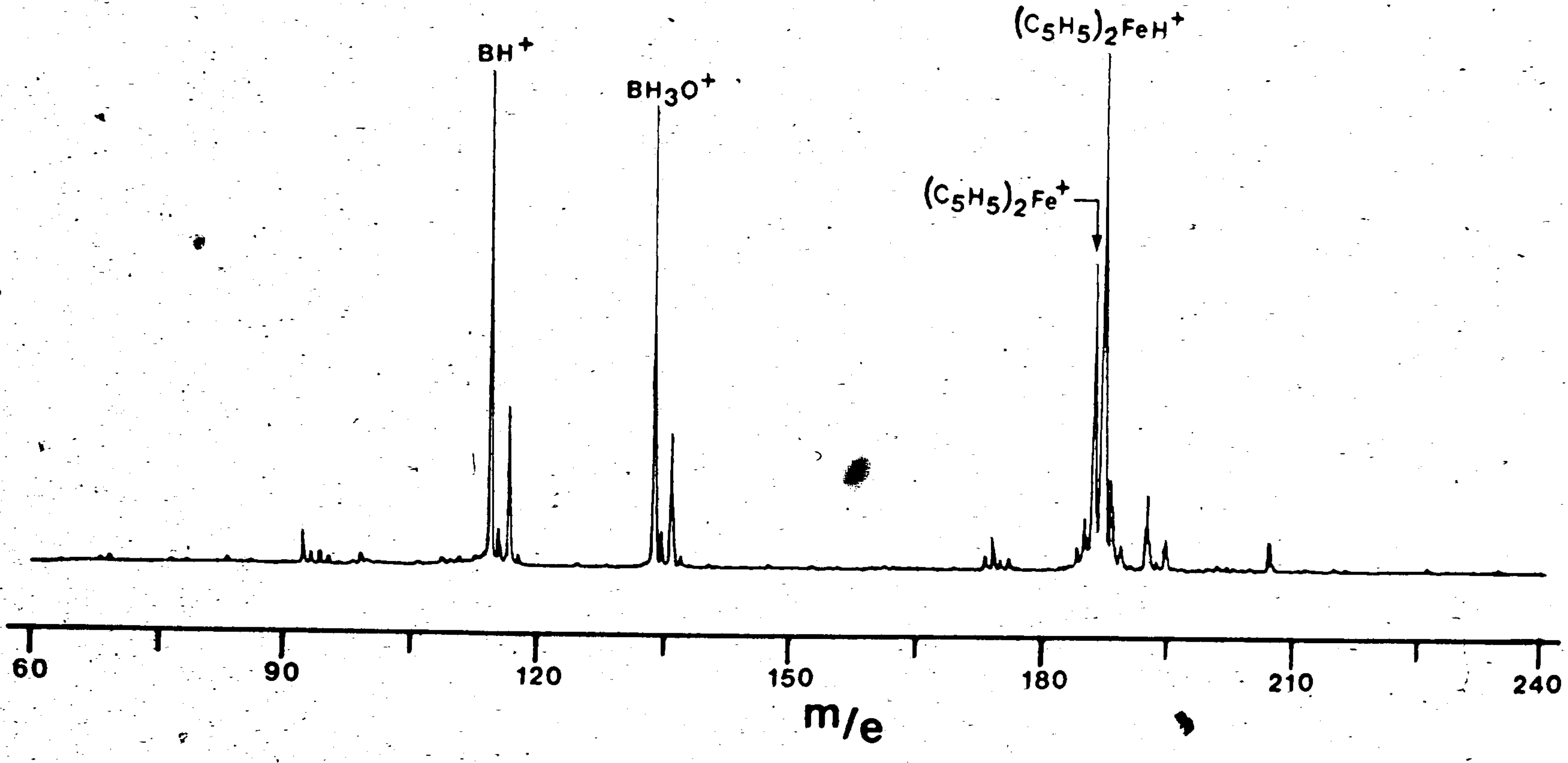

Figure 4.4. HPCI mass spectrum of a methane/water/B:3-ClPy/ferrocene dissolved in toluene, mixture. Ion source conditions: T=405°K, P_{IS}=3.9 Torr, P_{water}=1.4 Torr, $P_{3\text{-}ClPy}$=0.13 mTorr, $P_{ferrocene}$=4.9 mTorr, and $P_{toluene}$=0.07 mTorr. Max. sens. 5*10^3CPS, pulsing mode.

The specificity and versatility of the HPCI technique is illustrated in these figures by the cleanliness of the mass spectra, with the pseudo molecular ion (MH^+) always present in large abundance due to the absence of any apparent fragmentation.

A. Treatment of Experimental Data for Evaluating K_{eq}, ΔG^o, ΔH^o, and ΔS^o for the Proton Transfer Equilibrium Reaction: $BH^+ + (C_5H_5)_2Fe \rightleftharpoons (C_5H_5)_2FeH^+ + B$.

The temporal profile of the positive ions involved in the ion-molecule equilibrium reaction 4.2 obtained from a typical experimental run, is shown in Figure 4.5A. A mixture of 4.65 Torr CH_4, 9.55 mTorr acetophenone and 0.361 mTorr ferrocene at 500^{o}C was used in this run. Figure 4.5A gives a plot of the logarithm of the counts per channel for each ion against the time after the electron pulse. The primary ions produced by the electron pulse are mainly due to methane, which is present in very large concentrations. As is evident from Figure 4.5A, both acetophenone and ferrocene are protonated by the reactant ions from methane (CH_5^+, $C_2H_5^+$) very soon after the electron pulse. Proton transfer between the protonated species and the neutral acetophenone and ferrocene then follows.

An alternate way of displaying the experimental data is obtained through the normalization procedure, in which the

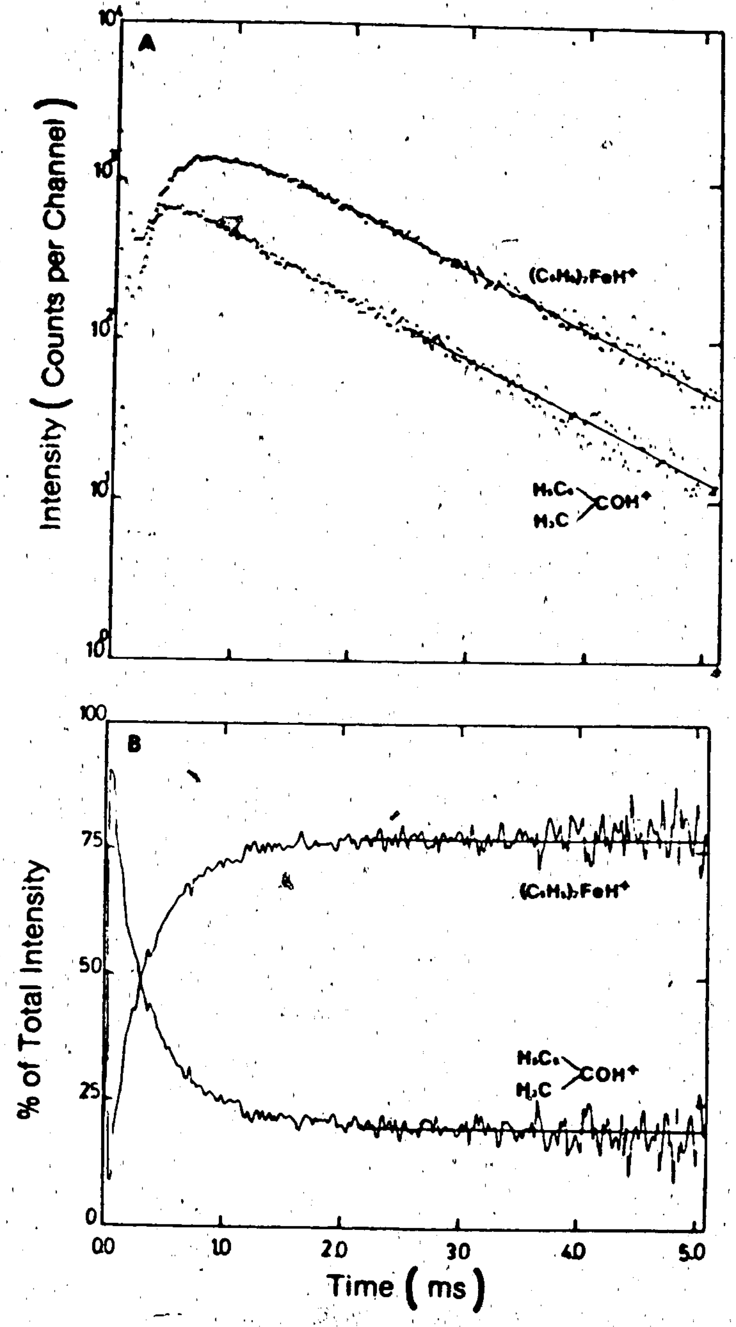

Figure 4.5. Time dependence of ion currents with achievement of equilibrium. Gaseous mixture in ion source: CH_4 at 4.65 Torr, $C_6H_5COCH_3$ at 9.55 mTorr, and $(C_5H_5)_2Fe$ at 0.361 mTorr. T_{IS} = 500 K. (A) Time dependence of ion counts observed with the multichannel scaler. (B) Same experimental results as in (A) but presented in per cent of total ionization (normalized). Note: The straight lines in both (A) and (B) are drawn as means and are used for the evaluation of K_{eq}.

kinetic sequence leading to rather slow equilibrium between acetophenone and ferrocene is more evident. A normalized time profile of the protonated species is shown in Figure 4.5B (ions displayed as % of total ions). From the normalized data one can see more clearly the formation of $(C_5H_5)_2FeH^+$ from $[C_6H_5COHCH_3]^+$. The decrease of the protonated acetophenone intensity is due to formation of $(C_5H_5)_2FeH^+$. This kinetic stage is about a 2.0 msec duration, as is evident from Figure 4.5B. It will be assumed that the detected ion intensities for different reactant ions are proportional to the respective ion concentrations in the HPCI source (see Kebarle (66)). Since the concentration of the neutrals were constant in the HPCI source, due to the large abundance of neutrals relative to ions, the establishment of equilibrium is indicated by the invariance of relative ion intensities with time. This stage is achieved after some 2.0 msec, as shown in Figure 4.5 and lasts over the remaining time of the observation. The invariance of relative ion intensities between the two ions shows up as two parallel lines and the measured equilibrium ion intensity ratio can be determined from the vertical distance between the two lines of the logarithmic plot or from the ratio of the vertical distances between the base line and the two ion profile lines of the normalized (linear) plot.

The equilibrium constant K_2 and the standard free energy change for the proton transfer reaction G_2 were calculated with equation 4.6 and 4.7.

$$K_2 = \frac{P_{C_6H_5COCH_3}}{P_{(C_5H_5)_2Fe}} \times \frac{I((C_5H_5)_2FeH^+)}{I(C_6H_5COHCH_3)^+} \qquad 4.6$$

where P is the pressure of the neutrals and I is the intensity of the ions. For this particular experiment the pressure ratio of the neutrals was 26.5 and the ion intensity ratio, as measured from the logarithmic plot in Figure 4.5, was found to be 4.1. Substituting numerical values into equation 4.5 one obtains the equilibrium constant at 500 K:

$$K_2 = 26.5 \times 4.1 = 108.7$$

The standard free energy change, ΔG°_{T}, for the reaction can be calculated with equation 4.7.

$$\Delta G^{\circ} = -RT\ln K \qquad 4.7$$

therefore at 500 K, $\Delta G^{\circ}_{500} = -1.987 \times 10^{-3} \times 500 \times \ln 108.6$ kcal mol^{-1} = -4.7 kcal mol^{-1}.

The partial pressure of ferrocene in the ion source was varied in order to examine whether the equilibrium constant was independent of the ferrocene concentration. The invariance of the measured equilibrium constant K_1 with pressure of ferrocene is shown in Figure 4.6. Also, variation of the total ion source pressure, while all other conditions are constant, had no effect on the equilibrium constant. This is demonstrated in Figures 4.7A and B for two different ion source temperatures and the same gas mixture.

The standard free energy changes for reactions 4.3 and 4.4 were evaluated at 500 K by an analogous procedure and

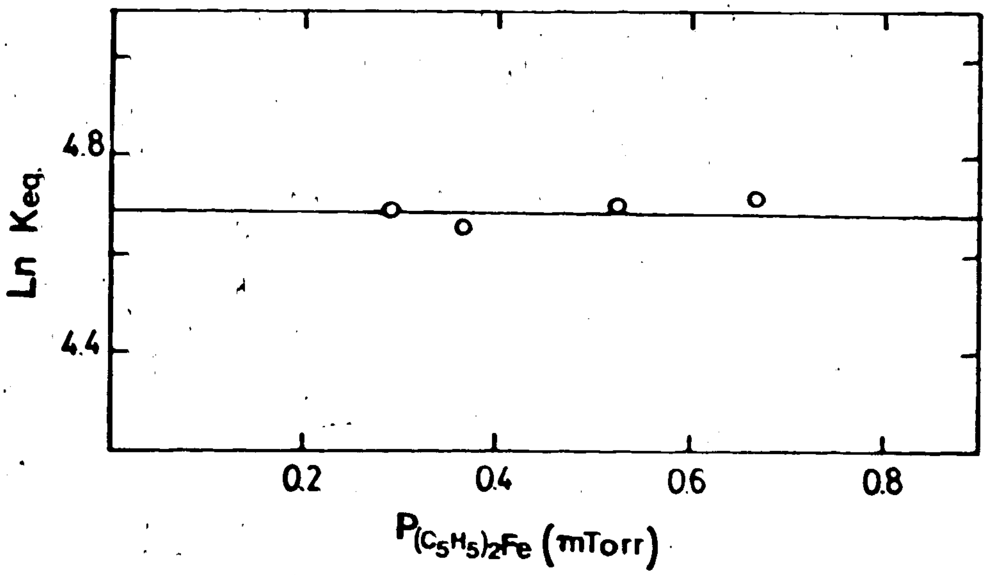

Figure 4.6. Logarithm of equilibrium constant K versus partial pressure of ferrocene at 500 K for the reaction: $[C_6H_5COHCH_3]^+ + (C_5H_5)_2Fe \rightleftharpoons C_6H_5COCH_3 + (C_5H_5)_2FeH^+$. Equilibrium constant is independent of ferrocene concentration changes. Bath gas, CH_4.

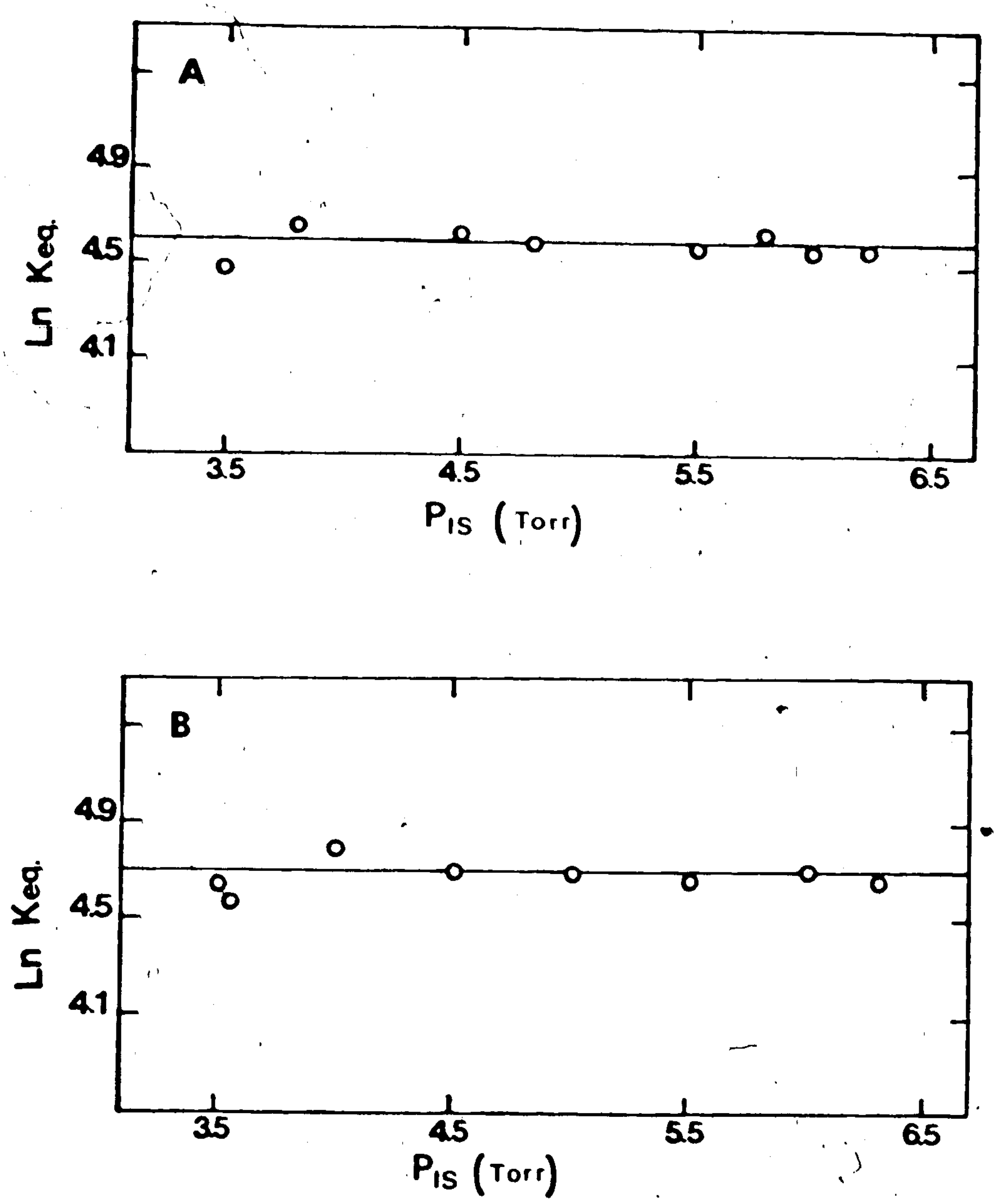

Figure 4.7. Logarithm of equilibrium constant K versus ion source pressures for the reaction: $[C_6H_5COHCH_3]^+ + (C_5H_5)_2Fe \rightleftharpoons C_6H_5COCH_3 + (C_5H_5)_2FeH^+$ at 490 K (A), and at 550 K (B). Equilibrium constant is independent of changes in total ion source pressures. Reagent gas, CH_4.

the results are reported in Table 4.1. The equilibrium constant K_4 for the DMF proton transfer reaction (equation 4.4) shows no dependence on ferrocene concentration at 500 K, as illustrated in Figure 4.8.

The temperature dependence of the acetophenone/ferrocene proton transfer equilibrium (reaction 4.2) was also investigated. Equilibrium constants, at different ion source temperatures, were obtained in exactly the same way as discussed above. The van't Hoff plot of this system is shown in Figure 4.9, while the resulting ΔH^o (slope of the line) and ΔS^o (intercept) values are given in Table 4.1

Attempts were made to study the temperature dependence of the DMF/ferrocene system, however the presence of DMF dimer $(DMF)_2H^+$ interfered, particularly at low temperatures. At ion source temperatures below 430 K the DMF dimer intensity was 10^3 times higher than that of the monomer. The dominance of the DMF dimer even at 500 K is evident in Figure 4.3.

B. Formation of $(C_5H_5)_2Fe^+$ and its Effect on the Proton Transfer Equilibrium Measurements.

The presence of $(C_5H_5)_2Fe^+$ was observed when the partial pressure of ferrocene in the source was raised above 3.0 mTorr. Using such a high pressure was necessary in the ferrocene/3-ClPy equilibria experiments in order to speed up the achievement of equilibrium. For equilibrium to be

TABLE 4.1 Thermochemical data resulted from the protonation of ferrocene equilibrium measurements.

Reaction	R.G.[a]	GB_B[b,e]	ΔH°[b]	ΔS°[c]	ΔG°_{500}[b]
1. $[C_6H_5COHCH_3]^+ + (C_5H_5)_2Fe = (C_5H_5)_2FeH^+ + C_6H_5COCH_3$	CH_4	197.4	-0.62±.4[d]	10.5±1.8[d]	-4.6
2. $C_4H_5NH^+ + (C_5H_5)_2Fe = (C_5H_5)_2FeH^+ + C_4H_5N$	CH_4	200.3	-	-	-1.9
3. $DMFH^+ + (C_5H_5)_2Fe = (C_5H_5)_2FeH^+ + DMF$	CH_4	203.6	-	-	1.75
4. $3\text{-}ClPyH^+ + (C_5H_5)_2Fe = (C_5H_5)_2FeH^+ + 3\text{-}ClPy$	CH_4/H_2O	207.0	10.1±1.0[d]	8.0±1.8[d]	6.04

[a] Reagent gas used. [b] Kcal/mol. [c] cal/mol K. [d] From van't Hoff plots shown in Figure 4.9. [e] Selected gas phase basicity values from Lias S.G. et al. (23) at 300°K. All (d) values have been obtained via linear regression and the error limits correspond to two standard deviations.

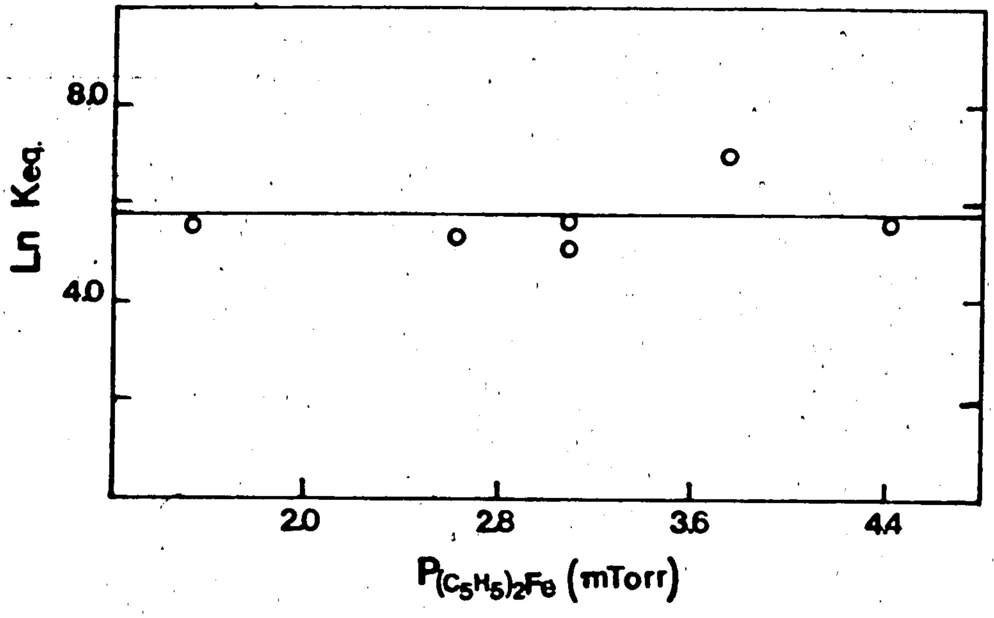

Figure 4.8. Equilibrium constant K versus partial pressure of ferrocene at 500 K for the reaction:

DMF + $(C_5H_5)_2FeH^+ \rightleftharpoons (C_5H_5)_2Fe$ + $DMFH^+$. Equilibrium constant is independent of ferrocene concentration changes.

Reagent gas, CH_4.

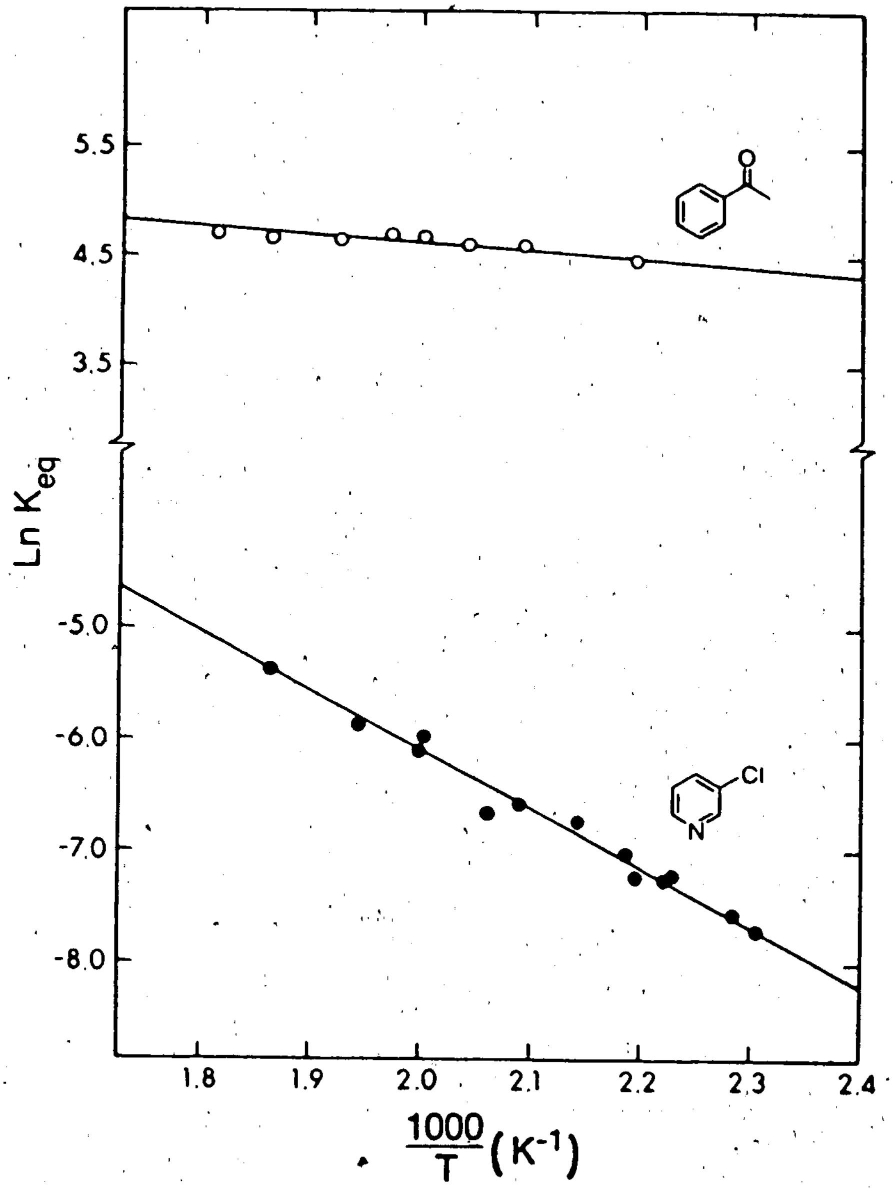

Figure 4.9. Van't Hoff plot of equilibrium constants for proton transfer reactions:
$BH^+ + (C_5H_5)_2Fe \rightleftharpoons (C_5H_5)_2FeH^+ + B$. a) B = 3-chloropyridine, $\Delta H^o = 10.1 \pm 1.0$ Kcal mol^{-1} and $\Delta S^o = 8.0 \pm 1.8$ cal mol^{-1} K^{-1}; b) B = acetophenone, $\Delta H^o = -0.6 \pm 0.4$ Kcal mol^{-1} and $\Delta S^o = 10.5 \pm 1.8$ cal mol^{-1} K^{-1}. Standard state 1 atm.

established, the partial pressure of the much stronger base 3-ClPy had to be kept low (0.1 to 1.0 Torr), while the partial pressure of ferrocene had to be raised above 4.5 mTorr.

The formation of $(C_5H_5)_2Fe^+$ probably occurs through the charge transfer ion-molecule reactions (4.8-4.10) involving the CH_4 reagent ions which are formed in the ion source during and immediately after the electron pulse. Evaluation of the energetics for each of the reactions 4.8-4.10 on the basis of available thermochemical data (23,94) shows that the reactions are exothermic. Since in general exothermic charge transfer ion molecule reactions are known to occur with high efficiency, the presence of $(C_5H_5)_2Fe^+$ in the mass spectrum can be understood.

$$CH_5^+ + (C_5H_5)_2Fe \rightarrow CH_3^{\cdot} + H_2 + (C_5H_5)_2Fe^+,\ \Delta H^o = -27.6 kcal/mol \quad 4.8$$

$$C_2H_5^+ + (C_5H_5)_2Fe \rightarrow C_2H_5^{\cdot} + (C_5H_5)_2Fe^+,\ \Delta H^o = -34.6 kcal/mol \quad 4.9$$

$$C_3H_7^+ + (C_5H_5)_2Fe \rightarrow C_3H_7^{\cdot} + (C_5H_5)_2Fe^+,\ \Delta H^o = -20.2 kcal/mol \quad 4.10$$

When CH_4/3-ClPy/ferrocene gas mixtures were investigated at high ferrocene concentrations, the observed ferrocene cation intensities were much greater (approximately 10 times) than those of the protonated ferrocene ion. To evaluate the equilibrium constant K_4 one needs the intensities of $(C_5H_5)_2FeH^+$ and 3-ClPyH$^+$. However the isotopic peak of $(C_5H_5)_2Fe^+$ at m/e 187 interfered with that of $(C_5H_5)_2FeH^+$ (also at m/e 187) and the establishment of equilibrium conditions between $(C_5H_5)_2FeH^+$ and 3-ClPyH$^+$ as they appeared from the time dependence ion profiles was not well identified. For this reason, in order to make equilibrium studies possible for reaction 4.4, the intensity of $(C_5H_5)_2Fe^+$ in the mass spectrum had to be decreased considerably so as to be able to subtract the isotopic portion of the $(C_5H_5)_2Fe^+$ ion intensity from the $(C_5H_5)_2FeH^+$ ion intensity at m/e 187.

The above difficulty was overcome by adding H_2O to the reagent gas. Under these conditions the CH_5^+, $C_2H_5^+$ and $C_3H_7^+$ engage in proton transfer to water and are removed. The resulting H_3O^+ and $H_3O^+(H_2O)_n$ do not engage in formation of $(C_5H_5)Fe^+$ because the reaction 4.11 is endothermic.

$$H_3O^+ + (C_5H_5)Fe \longrightarrow H_2O + H^\cdot + (C_5H_5)Fe^+,\ \Delta H^o = 7.0\,\text{kcal/mol} \qquad 4.11$$

A typical spectrum of a CH_4/H_2O/3-ClPy/ferrocene mixture is shown in Figure 4.4. The intensity of the $(C_5H_5)_2Fe^+$ peak is found to be fairly low, i.e. considerably lower than that of the $(C_5H_5)_2FeH^+$.

Further experiments indicated that the problem of $(C_5H_5)_2Fe^+$ formation would have been totally eliminated if neat water was used as reagent gas. Unfortunately under these conditions the 3-ClPyH$^+$/H_2O clusters became very strong and interfered with the measurements particularly at low ion source temperatures. After many trials it was established that a 1:1 CH_4/H_2O mixture was the most suitable reagent gas for low $(C_5H_5)_2Fe^+$ and 3-ClPyH$^+$/H_2O cluster ion currents in the temperature region between 425 K and 550 K.

To evaluate the equilibrium constant K_5 all three ions $(C_5H_5)_2Fe^+$, $(C_5H_5)_2FeH^+$, 3-ClPyH$^+$ had to be collected while keeping all experimental conditions constant during collection. Data from a typical run are shown in Figure 4.10. In all cases the $(C_5H_5)_2FeH^+$ ion currents had to be corrected for the isotopic contribution of $(C_5H_5)_2Fe^+$ at m/e 187. The percent abundance of the ferrocene cation at m/e 186 was calculated to be equal to 82.1% and 13.3% at m/e 187. This means that 16.1% of the ion current at m/e 187 is due to isotopic abundance of $(C_5H_5)_2Fe^+$, therefore 16.1% of the $(C_5H_5)_2Fe^+$ ion intensity at m/e 186 had to be subtracted from the $(C_5H_5)_2FeH^+$ ion intensity at m/e 187 in order to get the actual representation of the protonated ferrocene ion current $I^{corr}((C_5H_5)_2FeH^+)$. Equilibrium constant K_5 evaluated by the above procedures was used in the van't Hoff plot, shown in Figure 4.9 while the resulting ΔH^o and ΔS^o values are given in Table 4.1

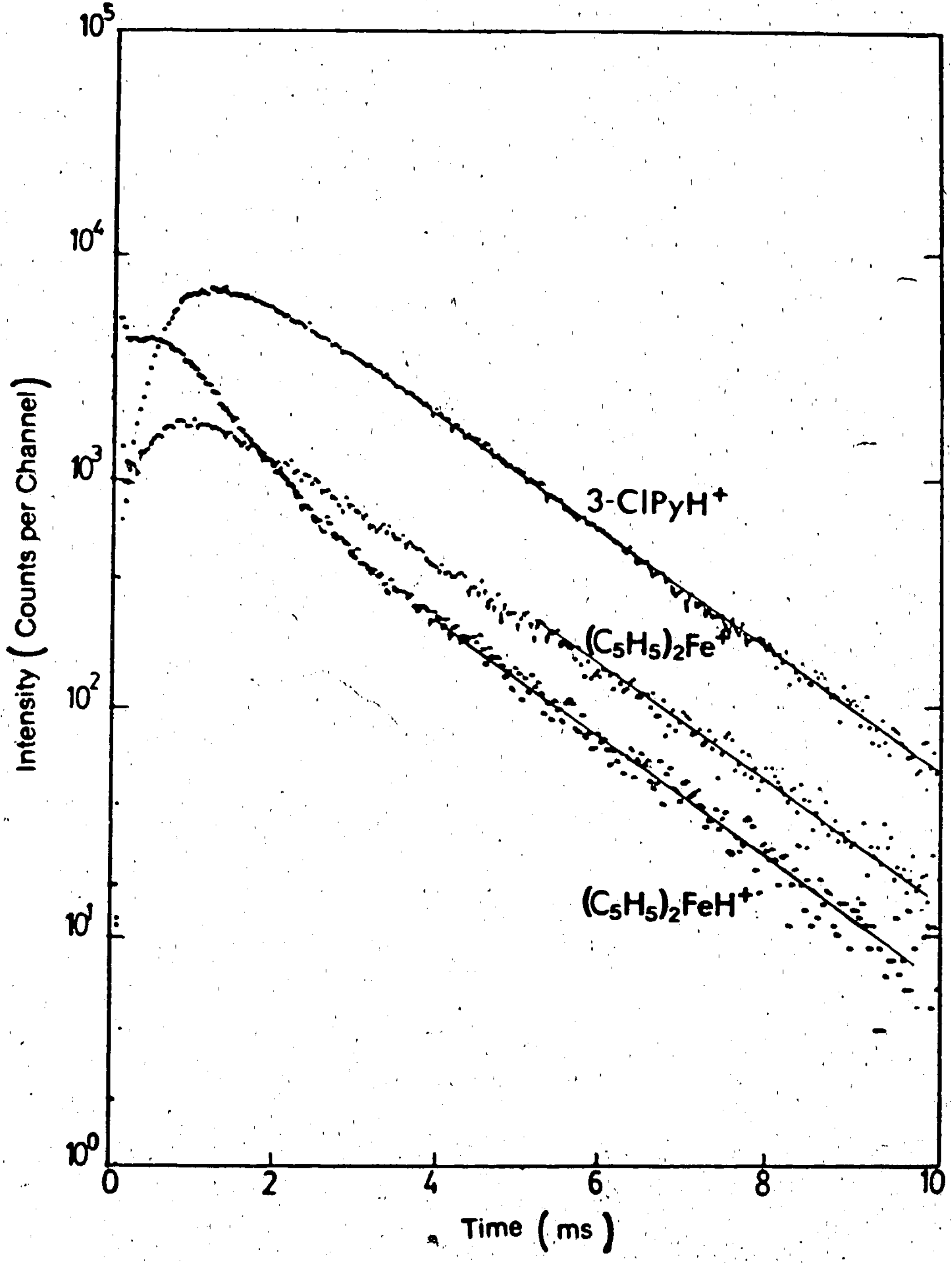

Figure 4.10. Time dependence of ion currents with achievement of equilibrium, as observed with the multichannel scaler. Gaseous mixture in the ion source: CH_4 plus H_2O at 6.0 Torr, ferrocene at 8.16 mTorr, and 3-ClPy at 0.42 mTorr. Temperature 536 K.

C. Comparisons of Gas Phase Basicities at Different Temperatures.

The gas phase basicity, GB, of a molecule M is defined as $-\Delta G^{o}$ for the protonation reaction 4.12.

$$M + H^{+} \longrightarrow MH^{+} \qquad 4.12$$

The gas phase basicity is a function of temperature, since the entropy change ΔS^{o} for reaction 4.12 is usually large. There are two contributions to this entropy change (ΔS^{o}). First, the proton in reaction 4.12 has a significant translational entropy of about -26 cal K^{-1} mol^{-1} at 300 K (23) which is lost on formation of MH^{+}. Second, there is an "internal" entropy change, ΔS°_{int}, associated with the geometry and vibrational and rotational changes for the formal half reaction:

$$M \longrightarrow MH^{+} \qquad 4.13$$

As is well documented in the literature (23) ΔS°_{int} is usually quite small, less than a few cal K^{-1} mol^{-1}, and can often be ignored. Nevertheless, care must be taken to use consistent data when calculating gas phase basicity differences. This is so when the gas phase basicity of a reference base B (reported in the literature at 300 K), and the free energy associated with the equilibrium reaction

4.14 (reaction performed at temperature T), are to be combined for evaluation of the gas phase basicity of M.

$$BH^+ + M \rightleftharpoons MH^+ + B \qquad 4.14$$

In order to obtain the absolute GB value for M, the absolute GB value of the reference base has to be adjusted to the experimental temperature. The adjustment which is most relevant here is related to the entropy of the proton with respect to temperature. The literature GB and the adjusted GB_T values for a particular base can be related by the following equation:

$$GB_T = GB_{300K} - (300\ K)S^\circ_{300K}(H^+) + T*S^\circ_T(H^+) \qquad 4.15$$

This equation only takes into account the contribution of the entropy change of the proton into the GB_T value of the base as a function of temperature. $S^\circ_T(H^+)$ is accurately calculated from the Sackur-Tetrode equation (4.16) at standard state (1 atm.) (95).

$$S^o = R((5/2)\ln T + 3/2(\ln(M/amu)) - 1.164) \qquad 4.16$$

R is the gas constant (1.987 cal mol^{-1} K^{-1}), T is the reaction temperature in K, and M is the weight of the gas molecule in amu.

In this thesis, the GB values of all reference bases used have been utilized consistently, i.e. the entropy change of the proton has been incorporated into the GB_T value when the proton transfer reaction was performed at a temperature other than 300 K.

As previously mentioned, the gas phase basicity of ferrocene was evaluated in accordance with the gas phase basicity of the reference bases and with the free energy change associated in each of the reactions 4.2-4.5. The GB values for the reference bases were available from the Lias compilation at 300 K, but since all proton transfer equilibrium reactions 4.2-4.5 were studied at 500 K, adjustments in these literature GB values were applied.

According to the Sackur-Tetrode equation, the entropy of the proton $S^o(H^+)$ at 300 K is 26.01 cal K^{-1} mol^{-1} and 28.56 cal K^{-1} mol^{-1} at 500 K. Thus, the $T{\times}S^o$ term of equation 4.15 amounts to 7.80 kcal mol^{-1} at 300 K and 14.28 kcal mol^{-1} at 500 K, and the free energy change associated with the proton is 6.48 kcal mol^{-1} when the temperature is increased from 300 K to 500 K. Finally, the adjusted GB value of a base at 500 K can be obtained by subtracting 6.48 kcal mol^{-1} from the GB value reported in Lias, i.e. by utilizing equation 4.15. The literature and the adjusted GB values for the four reference bases used in the ferrocene proton transfer equilibrium measurements are given in Table 4.2

TABLE 4.2 Literature[a] and Adjusted GB Values for $C_6H_5COHCH_3$, C_4H_5N, DMF, and 3-ClPy.

BASE	GB[a,b]	GB(Adj)[b,c]
$C_6H_5COHCH_3$	197.4	190.9
C_4H_5N	200.3	193.8
DMF	203.6	197.1
3-ClPy	207.0	200.5

[a] From Lias et. al. (23) at 300 K.

[b] In units of kcal-mol^{-1}.

[c] As calculated from equation 4.15 using $S^\circ_{300K}(H^+)=26.01$ e.u., $S^\circ_{500K}(H^+)=28.56$ e.u., and T=500 K.

Adjustment for the "internal" entropy change associated with the protonation of the reference base itself was not applied, but it is commonly assumed to be small (23,65a) However, if the ΔS^{o} value associated with the proton transfer equilibrium reaction of the reference base was available, this adjustment would have been possible.

At this point it is important to mention that in the Lias et al (23) GB tables, a different method has been used for compiling GB values. In this method the GB values are adjusted to 300 K by [illegible]tting the $T \times S^{o}$ term associated with the proton to 7.8 Kcal mol^{-1} at all temperatures. Such adjusted gas phase basicity values can be seen as the $-\Delta G^{o}_{T}$ for the reaction:

$$M_{T(K)} + H^{+}_{300K} \rightleftharpoons MH^{+}_{T(K)} \qquad 4.17$$

Again, with this method there has not been any adjustment in the GB values related to the internal entropy change of M upon protonation. It is assumed to be very small.

D. The Gas Phase Basicity Ladder. Evaluation of the Gas Phase Basicity, at 500 K, and Proton Affinity of Ferrocene.

The equilibrium constants and consequently the free energy changes associated with each of the four proton transfer equilibrium reactions 4.2 to 4.5 were determined at

500 K. A higher reaction temperature was chosen so as to avoid interference from the formation of protonated dimers of the reference bases (B). These dimer ions become the major ions at lower temperatures if the reference base is oxygen or nitrogen protonated (positive charge localized in a few hydrogens), as in the case of acetophenone and DMF.

The gas phase basicity of ferrocene was determined by obtaining a continuous "ladder" (Figure 4.11) of overlapping proton transfer free energy changes associated with each of the four reactions 4.2 to 4.5. The free energy (ΔG°_{500}) value for a given reaction obtained by direct measurements is shown beside the arrow linking ferrocene with the appropriate base (Figure 4.11). Four thermodynamic cycles connect ferrocene to the other bases. The multiplicity of the thermodynamic cycles was necessary for increasing the confidence of the results obtained. The consistency of the basicity measurements is demonstrated in Figure 4.11. By inspection of the ΔG°_{500} values given in the Figure, one can verify that the internal consistency is less than 1.0 kcal mol^{-1}. The four independent measurements lead to a value of $\underline{195.35 \pm 0.5 \text{ kcal mol}^{-1}}$ for the gas phase basicity of ferrocene at 500 K.

The proton affinity, PA, of a molecule M is defined as $-\Delta H^{\circ}$ for the reaction:

$$MH^{+} \rightleftharpoons M + H^{+} \qquad 4.18$$

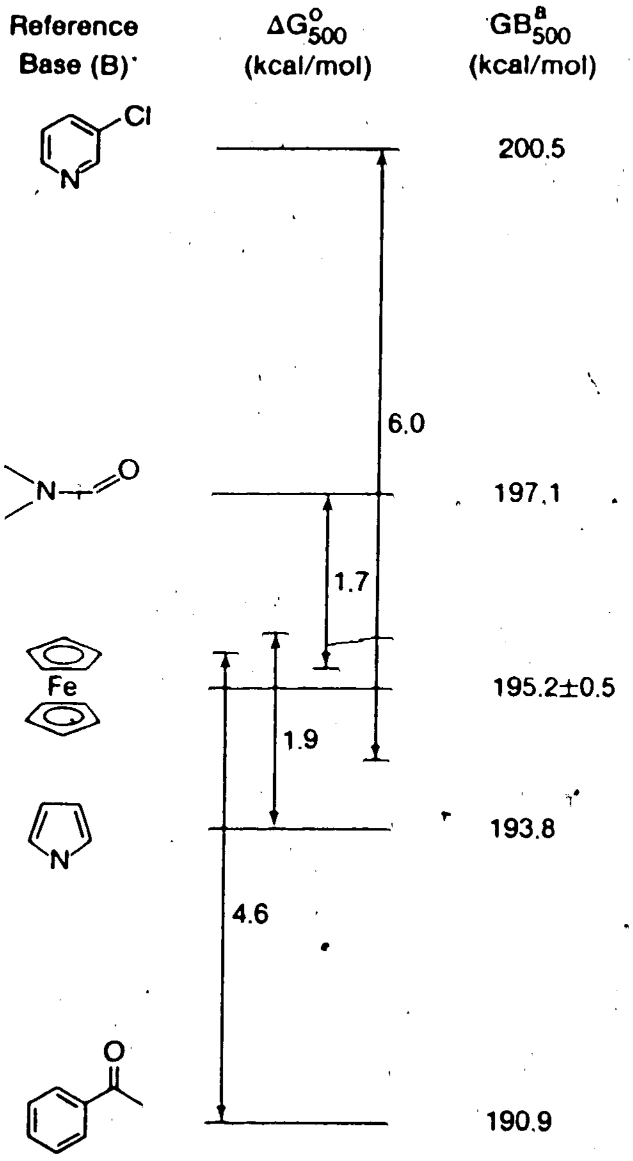
Reference Base (B)'
ΔG^{o}_{500} (kcal/mol)
GB^{a}_{500} (kcal/mol)
Cl
N
200.5
6.0
N
O
197.1
1.7
Fe
195.2±0.5
1.9
N
193.8
4.6
O
190.9

Figure 4.11. Gas-phase basicity ladder based on measurements of equilibrium constants K for equilibria,: $BH^{+} + (C_5H_5)_2Fe \rightleftharpoons (C_5H_5)_2FeH^{+} + B$, at 500 K. Values given between double arrows connecting reference base B and ferrocene, correspond to ΔG^{o} of the above reaction. The four determinations lead to a GB value of ferrocene which is consistent within less than 1 kcal mol^{-1}. [a] Adjusted GB values of the reference bases as outlined in Table 4.2.

which can also be expressed in terms of ΔG^o (or GB) and ΔS^o by the following equation:

$$GB = PA - T*\Delta S^o \quad 4.19$$

where $\Delta S^o = S^o(H^+) + S^o(M) - S^o(MH^+)$, but since $S^o(M) - S^o(MH^+) = -\Delta S^o_{INT}$ for M, equation 4.19 can be rearranged as follows:

$$PA = GB - T\Delta S^o_{INT} + TS^o(H^+) \quad 4.20$$

For many organic molecules only approximate proton affinity values have been reported in the literature. This is mainly because they have been obtained from the ΔG^o values resulting from GB ladders, while neglecting the $T\times\Delta S^o$ term in equation 4.19 since it is most often not known and it is thought to be very small. However, with ferrocene ΔS^o_{INT} is not small. The van't Hoff plots associated with the proton transfer reactions 4.2 and 4.5 show a fairly large entropy change upon protonation of ferrocene.

The proton affinity of ferrocene was determined by utilizing equation 4.20. As ΔS^o_{INT} an average value of $\underline{9.3 \pm 2.0 \text{ cal mol}^{-1} \text{ K}^{-1}}$ was used from the two values reported in Table 4.1. GB was obtained from the GB ladder while a value of 14.28 kcal mol^{-1} was assigned to $TS^o(H^+)$ term at 500 K. Thus, the proton affinity of ferrocene was calculated to be 204.9 ± 2.0 kcal mol^{-1} i.e. (P.A. = 195.3 ± 0.5 - 500(9.3 ± 2.0) + 14.28)

4.3.1 Discussion Related to the Entropy Change Upon Protonation of Ferrocene.

As mentioned above, an average value of ΔS^o = 9.3 ± 2.0 cal K^{-1} mol^{-1} representing the entropy change of ferrocene upon protonation, resulted from the two van't Hoff plots of the acetophenone/ferrocene and 3-ClPy/ferrocene systems (Figure 4.9).The internal entropy changes upon protonation of 3-chloropyridine and of acetophenone should be small, because there are no changes in symmetry. Neither are any large changes in molecular structure expected for these molecules. The experimental entropy change of 9.3 cal K^{-1} mol^{-1} can therefore be solely attributed to an increase of the internal entropy of ferrocene upon protonation. The value is unusally large for a proton transfer reaction.

The difference in entropy between ferrocene and protonated ferrocene can be estimated and compared to the experimental value quoted above. A significant contribution to the entropy difference derives from the rotational entropy change, Eq. 4.21.

$$\Delta S^o_{INT} = R * \ln(\sigma_{FH}/\sigma_F) \qquad 4.21$$

Ferrocene has a symmetry factor, σ_F; of 10. The symmetry factor for protonated ferrocene, σ_{FH}, depends on its structure. If protonation occurs on the iron atom (96), the symmetry factor is 2. The rotational contribution to the entropy would thus be R*ln(10/2) = 3.2 cal K^{-1} mol^{-1}.

In addition to the changes in symmetry, the molecular structure of ferrocene is also changed upon protonation. Vibrational analysis has shown that the cyclopentadiene (Cp) rings in protonated ferrocene are tilted and that there is a significant loosening of the iron ring bonds (91). For example, the asymmetric ring-metal strech frequency decreased from 478 cm^{-1} (97) in ferrocene to 435 cm^{-1} (91) in the protonated molecule. The entropy of gaseous ferrocene has been determined both by low temperature calorimetry (98,99) and calculated from molecular spectra (97). When the latter calculation is repeated using Pavli'K's (91) vibrational frequencies for protonated ferrocene it is found that the entropy is 2.0 cal K^{-1} mol^{-1} higher than for ferrocene.

The total entropy change upon protonation of ferrocene is thus estimated to be 5.2 cal K^{-1} mol^{-1}. Of these 3.2 cal K^{-1} mol^{-1} is attributed to the rotational entropy and 2.0 cal K^{-1} mol^{-1} to a weakening of the metal ring bonding. The experimental value is 4.0 cal K^{-1} mol^{-1} larger. However, from experience, the uncertainty in experimental entropy values is ± 3-4 cal K^{-1} mol^{-1}. There are also uncertainties in the entropy estimate, and the discrepancy between the experimental entropy value and the estimated value is not really serious.

The present PA value of 204.9 kcal mol^{-1} is outside the error limits quoted by Beauchamp, 213 ± 5 kcal mol^{-1} (88). The discrepancy is mainly due to the internal entropy change of ferrocene upon protonation, which value was of course unknown to the previous authors. Thus, the proton affinities and entropy values obtained in the present work is in fair agreement with the bracketing results of reference (88).

4.4 Kinetic and Rate Constants Associated with the Protonation of Ferrocene.

The rates of exothermic ion-molecule reactions leading to proton transfer in the gas phase are usually fast and the rate constants are very close to the theoretically calculated Langevin or ADO orbiting collision rates (100). These depend on reduced mass, polarizability, and dipole moment, and are always close to $k_L = 10^{-9}$ $molec^{-1}$ cm^3 sec^{-1}. Furthermore, only a weak temperature dependence is predicted for k_L (100) and this what is generally experimentally observed.

In the case of ferrocene, this general statement does not seem to apply. From the acetophenone/ferrocene experiments conducted for the evaluation of the GB value of ferrocene, it was realized that the rates associated with the proton transfer reaction 4.2 were generally slow, and also show strong temperature dependence. For this reason, it was thought that a thorough investigation of the kinetics of the ferrocene protonation would provide data of interest.

The kinetics related to protonation of ferrocene were investigated using a number of ring protonated [Benzene (BEN), Toluene (TOL), o-Xylene (XYL), Anisole (ANI) (101), Hexamethylbenzene (HMB), 3-ClPy], and oxygen protonated (Acetone, Acetophenone) reagent ions (BH^+).

The proton transfer rate constant for the eight reaction systems (4.2, 4.5 and 4.22-4.27) was measured at 500 K.

$$BENH^+ + (C_5H_5)_2Fe \rightleftharpoons (C_5H_5)_2FeH^+ + BEN \qquad 4.22$$

$$TOLH^+ + (C_5H_5)_2Fe \rightleftharpoons (C_5H_5)_2FeH^+ + TOL \qquad 4.23$$

$$o\text{-}XYLH^+ + (C_5H_5)_2Fe \rightleftharpoons (C_5H_5)_2FeH^+ + o\text{-}XYL \qquad 4.24$$

$$ANIH^+ + (C_5H_5)_2Fe \rightleftharpoons (C_5H_5)_2FeH^+ + ANI \qquad 4.25$$

$$HMBH^+ + (C_5H_5)_2Fe \rightleftharpoons (C_5H_5)_2FeH^+ + HMB \qquad 4.26$$

$$(CH_3)_2COH^+ + (C_5H_5)_2Fe \rightleftharpoons (C_5H_5)_2FeH^+ + (CH_3)_2CO \qquad 4.27$$

In addition, the temperature dependence of the forward rate constants for the systems 4.2 and 4.24 - 4.27 were also investigated as outlined in the next section.

4.4.1 Treatment of Experimental Data for Evaluating the Forward Rate Constant for the Reaction $BH^+ + (C_5H_5)_2Fe \rightleftharpoons (C_5H_5)_2FeH^+ + B$

For all the kinetic experiments conducted in this study, the ion intensities of the ions under investigation were displayed in the normalized mode. Since the normalization procedure involves expressing the ion intensity of a given ion at a given time, t, as the percentage of the total ion intensity at time t, it represents the variation of ion intensities in the ion source in which the total ionization is constant. This ammounts to the assumption that the diffusion coefficient of all the ions are the same, an assumption that is approximately true (66).

Depending on the complexity of the results obtained from each of the systems, 4.2, 4.5, and 4.22-4.27, using the normalized ion intensities, different methods were applied for evaluating the forward rate constant leading to protonation of ferrocene. The methods applied and the resulting rate constant values for each of the systems at 500 K are summarized in Table 4.3.

A. **Method I** Irreversible Proton Transfer to Ferrocene from Reference Base B.

In order to illustrate this method, experimental data from the benzene/ferrocene system will be used. The same

TABLE 4.3. Rate Constants for the proton transfer reaction.

$$BH^{+} + (C_5H_5)_2Fe \underset{k_R}{\overset{k_F}{\rightleftharpoons}} (C_5H_5)_2FeH^{+} + B$$

Equation No.	B^a	$k_F^b \times 10^{-10}$	Method^g	$\Delta GB^{c,d}$
4.1	$C_6H_5COCH_3$^{e}	3.0	I,II	-4.3
4.4	3-ClPy^f	0.0035	IV	+5.3
4.22	BEN^f	17.6	I	-27.1
4.23	TOL^f	9.66	I	-19.7
4.24	O-XYL^f	6.26	I	-15.6
4.25	ANI^f	0.57	I	-9.2
4.26	HMB^f	0.09	I	-1.7
4.27	$(CH_3)_2CO$^{e}	11.2	III	-12.8

[a] Reference base used.

[b] Forward rate constant at 500°K (cm^3 molecul^{-1} s^{-1}).

[c] Differences in gas phase basicities between ferrocene and the reference base. All GB values obtained from Lias (23) except for that of ferrocene

[d] ΔGB values refer to the difference in GB between ferrocene and reference base B.

[e] Oxygen protonated base.

[f] Ring protonated base.

[g] Different methods in evaluation k_F at 500°K. All methods are outlined in the text.

procedure, was also applied for the evaluation of the proton transfer rate constants (k_F) for the following systems:

Toluene/Ferrocene, (k_F evaluation at all temperatures)

o-Xylene/Ferrocene, (k_F evaluation at all temperatures)

Anisole/Ferrocene, (k_F evaluation at all temperatures)

HBM/Ferrocene, (k_F evaluation at all temperatures)

Acetophenone/Ferrocene, (evaluation of k_F for experiments conducted above 500 K with the acetophenone dimer not present).

Shown in Figure 4.12 are the experimentally obtained normalized ion intensities for four different experimental conditions from the benzene/ferrocene system. A decrease of protonated benzene and a concomintant increase of protonated ferrocene is observed. This change is due to proton transfer reaction 4.22. The rate of the reaction increases as the ferrocene concentration is increased. Close inspection of all the runs in this Figure reveals the existence of $(C_5H_5)_2FeH^+$ ion concentrations at zero time (right after the electron pulse). This is because an ion repeller (quench) pulse was not applied after each reaction cycle, therefore ions were still present in the ion source when the subsequent electron pulse was applied.

The data of the benzene/ferrocene system will be analyzed here but much of the discussion is applicable to the general proton transfer reaction 4.1 for evaluating k_F. The latter statement applies only when the reacting system is free from any apparent side reactions as will be

Figure 4.12. Time dependence of the normalized ion intensities after the ionizing electron pulse. Decrease of $BENH^+$ and concomintant increase of $(C_5H_5)_2FeH^+$ is due to proton transfer reaction (4.22). Pressures: CH_4, 4.25 Torr (reagent gas); ferrocene, 0.077 mTorr, benzene, 5.0 mTorr in A; ferrocene, 0.157 mTorr, benzene, 7.0 mTorr in B; ferrocene, 0.259 mTorr, benzene, 9.36 mTorr in C; ferrocene, 0.388 mTorr, benzene, 12.4 mTorr in D. Temperature 500 K.

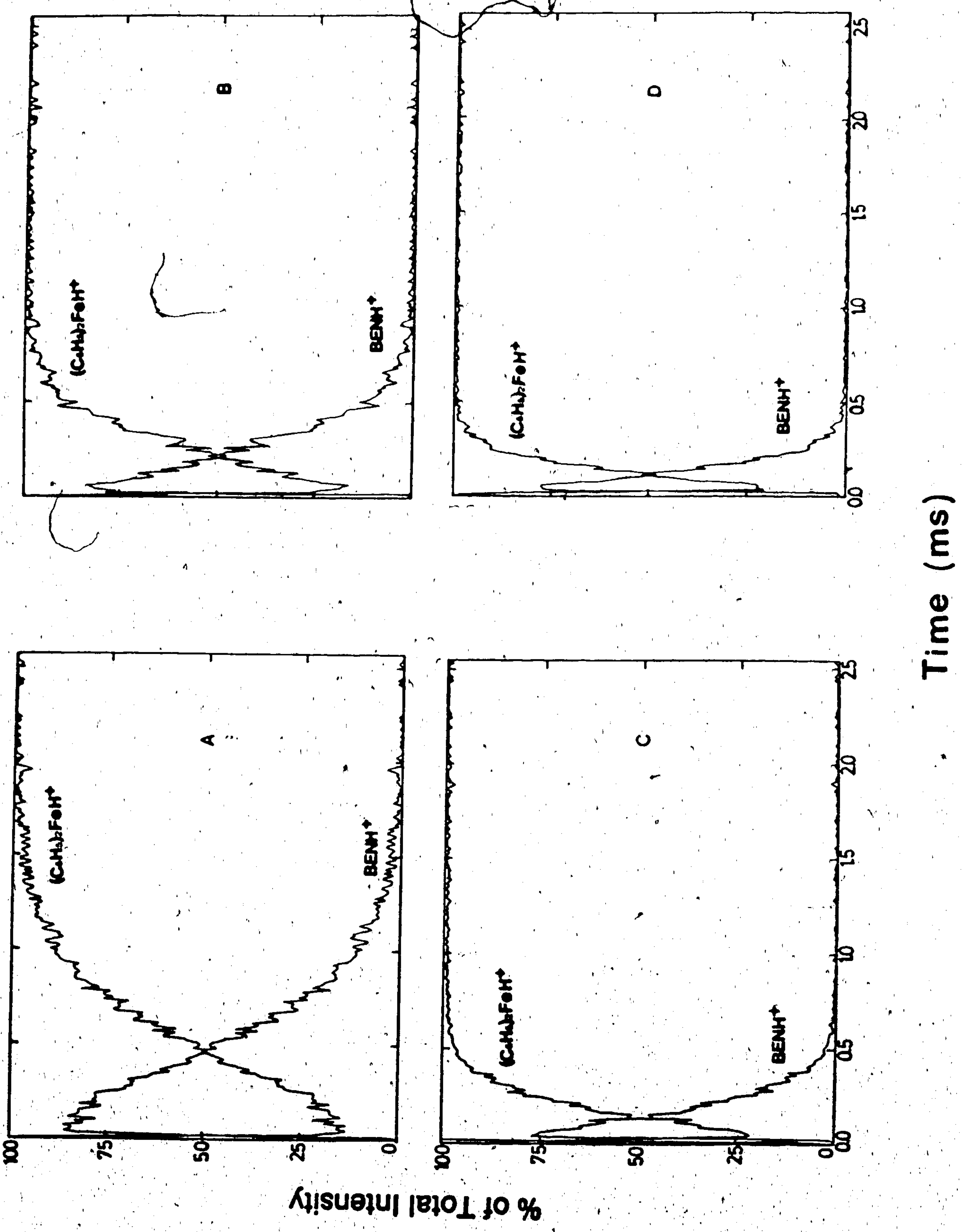
A
B
C
D
$(C_5H_5)_2FeH^+$
BENH$^+$
% of Total Intensity
Time (ms)
100
75
50
25
0
0.0
0.5
10
15
20
25

illustrated in the following sections. The forward rate constant for the general reaction can be calculated from

$$-d(I^t(BH^+)/dt = k_F[(C_5H_5)_2Fe] \times I^t(BH^+) \qquad 4.28$$

where $I^t(BH^+)$ is the intensity of BH^+ at time t. Since the concentration of the ions is many orders of magnitude lower than the concentration of the neutrals, the concentration of the neutrals can be considered as constant. Reaction 4.1 is therefore first order and depends on the pseudo-first order rate constant (reaction frequency), ν_F, where $\nu_F = k_F[(C_5H_5)_2Fe]$. Therefore,

$$d(I^t(BH^+))/dt = -\nu_F \times I^t(BH^+) \qquad 4.29$$

after rearrangement and integration

$\ln(I^t(BH^+)/I$[illegible]$BH^+)) = -\nu_F x t$ 4.30

where $I^o(BH^+)$ is the concentration of BH^+ at time t=0. Therefore plotting the natural logarithm of the normalized intensity of BH^+ vs. time should lead to a straight line whose slope is equal to $-\nu_F$. Another way of obtaining ν_F values is also possible via the half life equation $t_{1/2} = (\ln 2)/\nu_F$ (102).

Plots of $\ln I^t(BH^+)$ vs. time for the benzene/ferrocene system are shown in Figure 4.13. Plots A,B,C, and D have resulted from the data in Figure 4.12 A,B,C, and D respectively. The pseudo-first order rate constants in each case were obtained from the slope of the lines. A plot of ν_F vs. ferrocene pressure for this particular system is given in Figure 4.14 (see points designated by (o)) for a reaction temperature of 500 K. The plot shows a linear dependence, which confirms that $\nu_F = k_F[(C_5H_5)_2Fe]$ as assumed above. Therefore the rate constant can be obtained from equation 4.31.

$$k_F = \nu_F/[(C_5H_5)_2Fe] \qquad 4.31$$

Similar plots of ν_F vs. $P((C_5H_5)_2Fe)$ observed with other BH^+ reagents are given in Figures 4.14 and 4.15. ν_F values for these plots at 500 K were obtained in exactly the same way as discussed for the benzene/ferrocene system. Figures 4.14 and 4.15 clearly illustrate the dependence of ν_F on ferrocene pressure for each of the systems. k_F values resulting from the slopes of the individual lines for a particular system, are summarized in Table 4.3. The k_F values are reported in $molecule^{-1}cm^3sec^{-1}$. These units were obtained by converting the gas pressures to $molecule\ cm^{-3}$ units via the ideal gas law equation and Avogadros number.

The temperature dependence of the rate constant for three of the reactions (4.24-4.26) involving exothermic

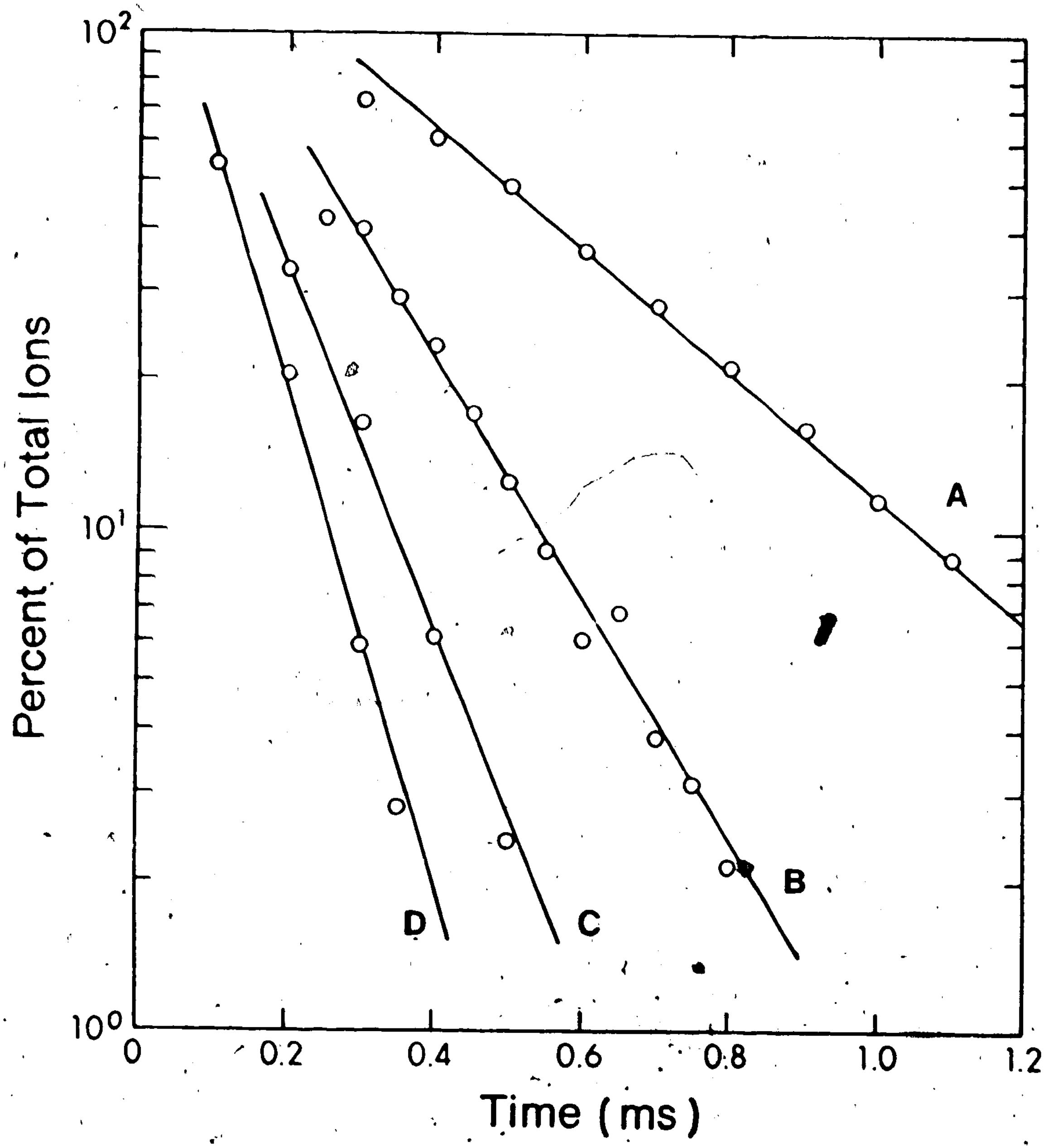

Figure 4.13. Logarithmic plot of normalized ion intensity of $BENH^+$ versus time for the diffenect experiments shown in Figure 4.12. Letters beside the lines represent the corresponding experiment in Figure 4.12. The slope of each of these lines leads to evaluation of the reaction frequency ν_F under the specified experimental conditions.

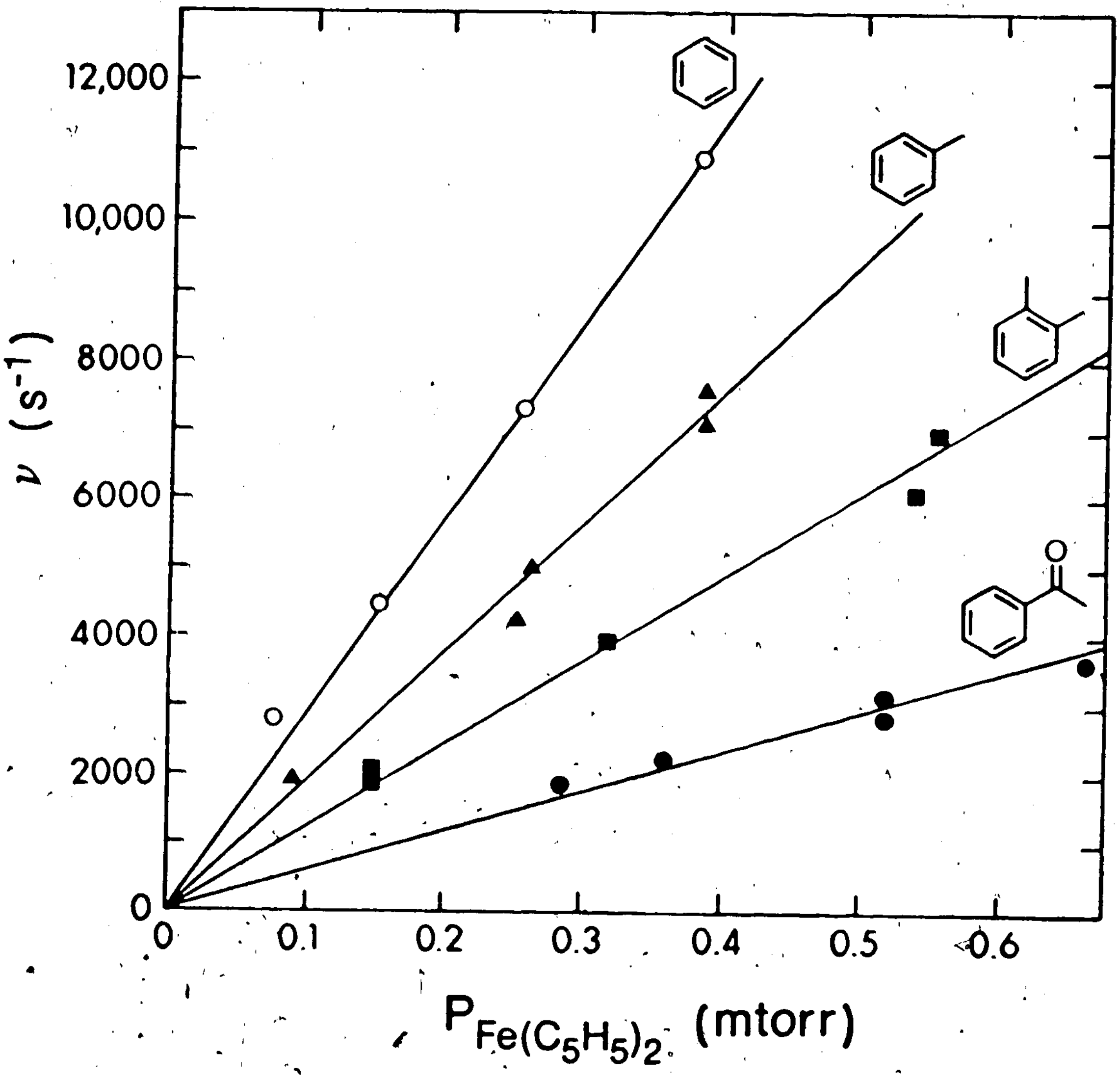

Figure 4.14. Plots of reaction frequency ν_F versus ferrocene pressure (mTorr). The slope of each line equals the rate constant k_F for the proton transfer reaction $BH^+ + (C_5H_5)_2Fe \longrightarrow (C_5H_5)_2FeH^+ + B$, at 500 K. The different reference bases, (B), used to obtain the individual plots are shown next to the lines.

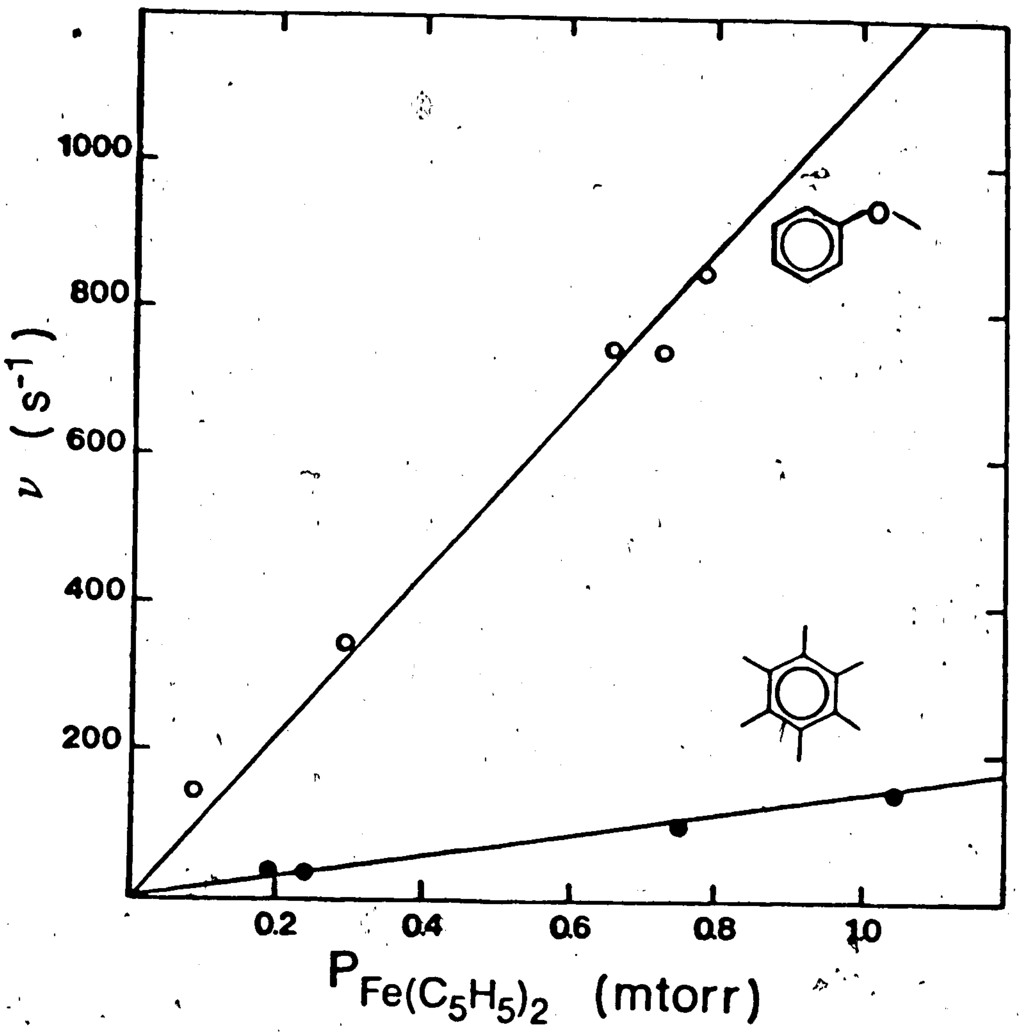

Figure 4.15. Plot of ν_F vs. ferrocene pressure. The slpoe of each line equals the rate constant k_F for the proton transfer reaction: $BH^+ + (C_5H_5)_2Fe \longrightarrow (C_5H_5)_2FeH^+ + B$ at 500 K. The different reference bases, (B), used to obtain the individual plots are shown next to the lines.

proton transfer to ferrocene, were also determined in a series of experiments. Arrhenius type plots (log k_F vs. 1/T) of these results are shown in Figure 4.16. These data show that the rate constants decrease with increase of temperature i.e. the rates have negative temperature dependence. The o-xylene/ferrocene reaction, being the most exothermic of the three, shows a negative temperature dependence in the high temperature region, while in the low temperature region it reaches collision rate efficiency. The rate constant in this second temperature region follows the expected very slight temperature dependence for k_L (Langevin - ADO rates, k_L ca. 10^{-9} molecule^{-1} cm^3 sec^{-1} (100)). The other two systems (ANI/ferrocene, HMB/ferrocene) undergo proton transfer reactions with gradually decreasing exothermicity relative to o-xylene. For these two systems the rate constants are much lower, and a constant negative temperature dependence is observed over the entire temperature region, Figure 4.16. The slopes of these straight line plots lead to evaluation of the exponential term E/R with $E = -1.63$ kcal mol^{-1} for anisole and -3.55 kcal mol^{-1} for HMB (preexponential factor $A = 0.095 \times 10^{-10}$ molecule^{-1} cm^3 sec^{-1}). The meaning of these results, together with those for the acetone/ferrocene and acetophenone/ferrocene systems will be examined in section 4.4.2 of this chapter.

The same method was also applied to the evaluation of rate constants for the acetophenone/ferrocene reactions

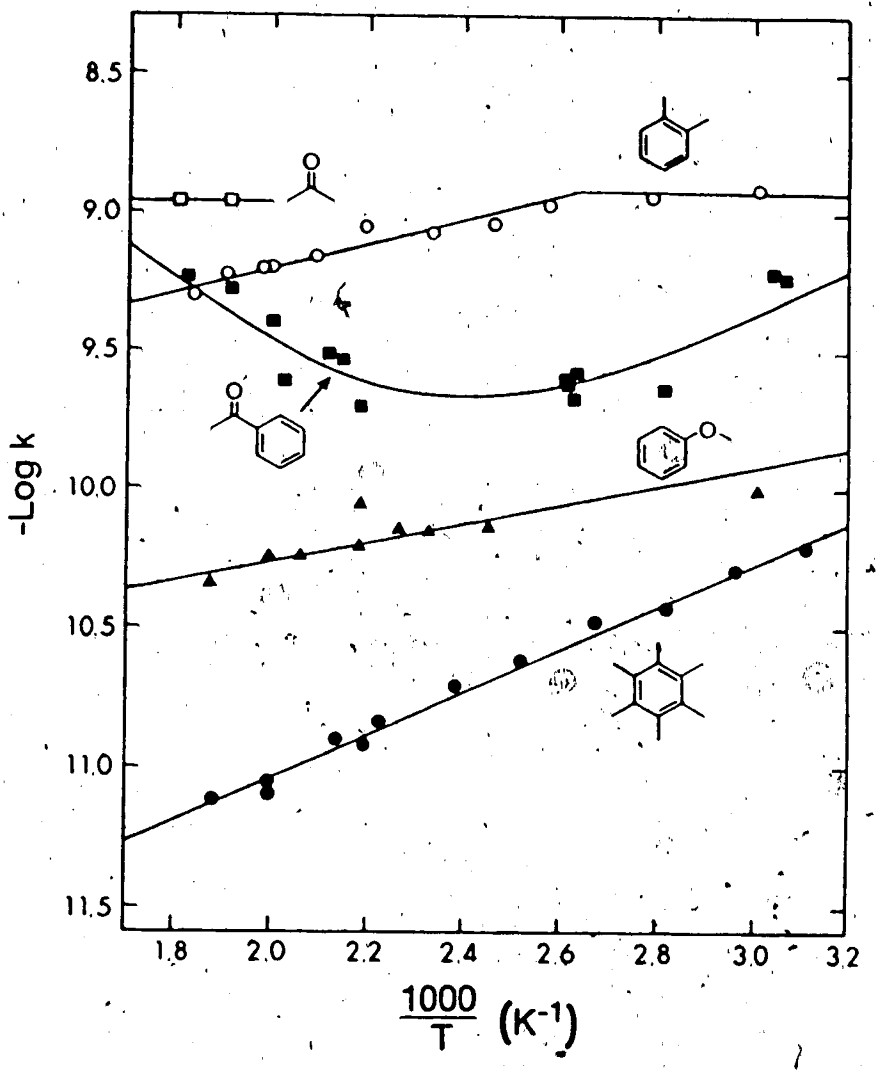

Figure 4.16. Arrhenius-type plots illustrating the temperature dependence of k_F associated with the proton transfer reaction: $BH^+ + (C_5H_5)_2Fe \longrightarrow (C_5H_5)_2FeH^+ + B$. Reference bases, (B), used in each case are specified next to the lines. The slope of the straight lines leads to evaluation of the activation energy (Ea) associated with each reaction.

studied at temperatures above 500 K where the acetophenone dimer was not present. An Arrhenius-type plot for this system is also given in Figure 4.16. k_F values at temperatures lower than 500 K were obtained via methods II, III, and IV described bellow.

B. Method II Reversible First Order Proton Transfer.

Data from the acetophenone/ferrocene system (reaction 4.2) will be used here to demonstrate this method but much of the discussion will be applicable to the general equation 4.1. Most proton transfer reactions at suitable concentration and temperature conditions become reversible. With reversible reactions, the rate of the reverse reaction only becomes apparent at long reaction times when the product ion has grown appreciably. The reverse reaction can be detected by the approach of equilibrium of the ions under investigation at long reaction times. Figure 4.17 illustrates such a situation for the acetophenone/ferrocene system, when the kinetic stage lasts for about 1.0 msec. After this time the ion intensity ratio $(C_5H_5)_2FeH^+$/ $[C_6H_5COHCH_3]^+$ becomes constant and remains so for the whole period of observation (ca 2.5 msec). In order to evaluate the forward rate constant from this set of data, equation 4.32, (103), was applied.

$$(k_F + k_R)t = \ln \frac{I^o(BH^+) - I^e(BH^+)}{I^t(BH^+) - I^e(BH^+)} \qquad 4.32$$

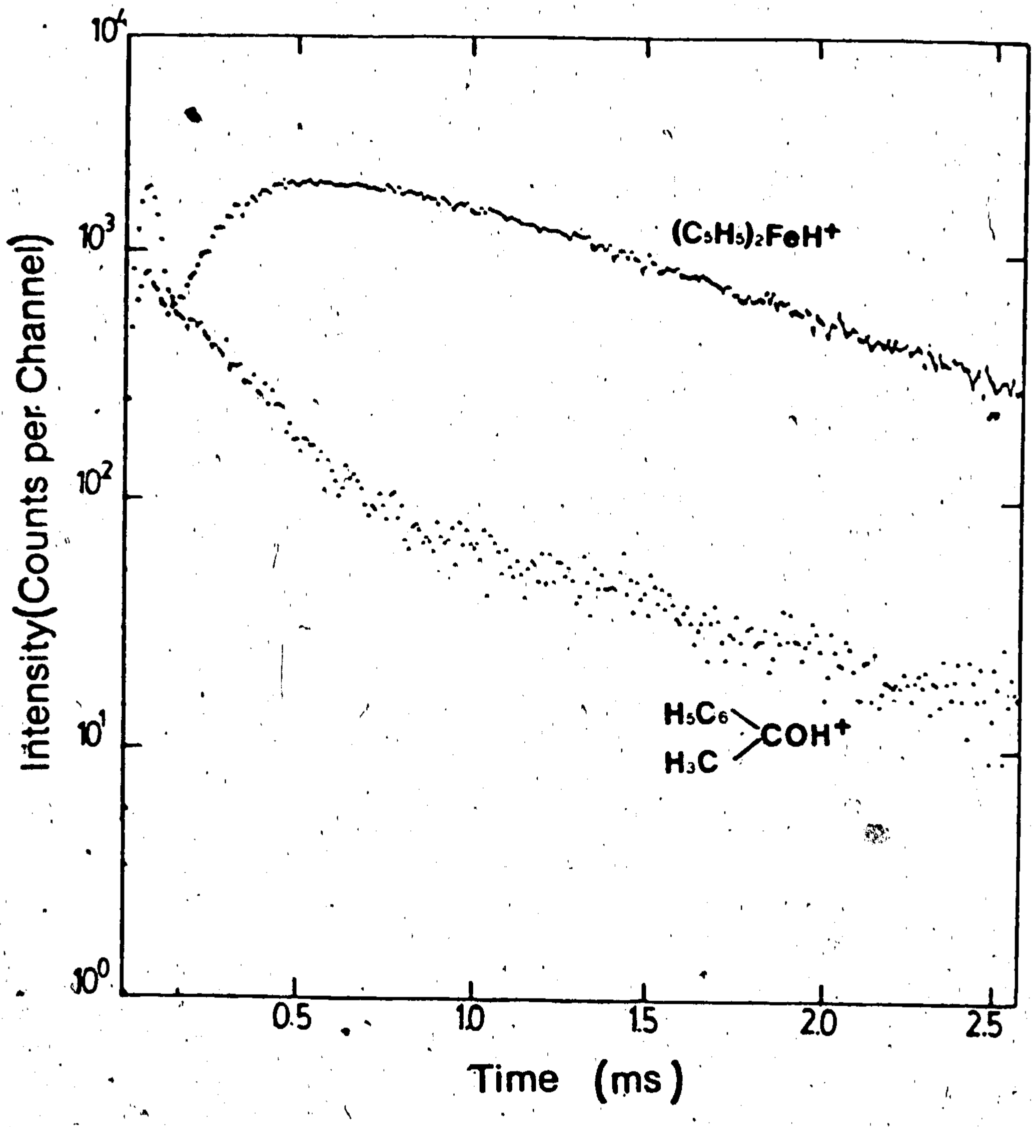

Figure 4.17. Time dependence of ion currents with rather slow achievement of equilibrium. Gaseous mixture in ion source: CH_4 at 5.0 Torr, $C_6H_5COCH_3$ at 2.90 mTorr, and $(C_5H_5)_2Fe$ at 0.68 mTorr. Temperature 550 K.

k_F and k_R are the forward and reverse rate constants for the reaction $I^o(BH^+)$, $I^e(BH^+)$, and $I^t(BH^+)$ are the normalized intensities of the reference base at the start of the reaction (t=0), at equilibrium, and at some time t after the start of the reaction, respectively. This equation applies only if $I((C_5H_5)_2FeH^+) = 0$ at t=0.

Considering that $K_{eq} = k_F/k_R$ (equation 4.36), $k_F = \nu_F/[(C_5H_5)_2Fe]$ (for pseudo-first order), $k_R = \nu_R/[B]$ (by expressing the rate of reaction 4.1 in terms of reverse rate constant), and $\nu_F/\nu_R = I^t((C_5H_5)_2FeH^+)/I^t(BH^+)$, (assuming equilibrium conditions), then by rearrangement of equation 4.32, ν_F can be expressed in terms of equation 4.33

$$\nu_F = \frac{d\,\mathrm{Ln}(I^t(BH^+) - I^e(BH^+)/dt}{(1-I^e(BH^+)/I^e((C_5H_5)_2FeH^+))} \qquad 4.33$$

A numerical value for the nominator term of this equation was obtained by using the slope of a plot of $\ln(I^t(BH^+) - I^e(BH^+))$ vs. time, see Figure 4.18, while values for $I^e(BH^+)$ and $I^e((C_5H_5)_2FeH^+)$ were obtained directly from the normalized spectra (time profiles), which resulted from this particular system. Then similarly as in method I, k_F values were obtained from the slope of the line from plots of ν_F (now obtained via equation 4.33) vs. ferrocene concentration. This method was used to evaluate rate constants for the acetophenone/ferrocene system at temperatures above 500 K and where the kinetic stage for the proton transfer reaction was short lived.

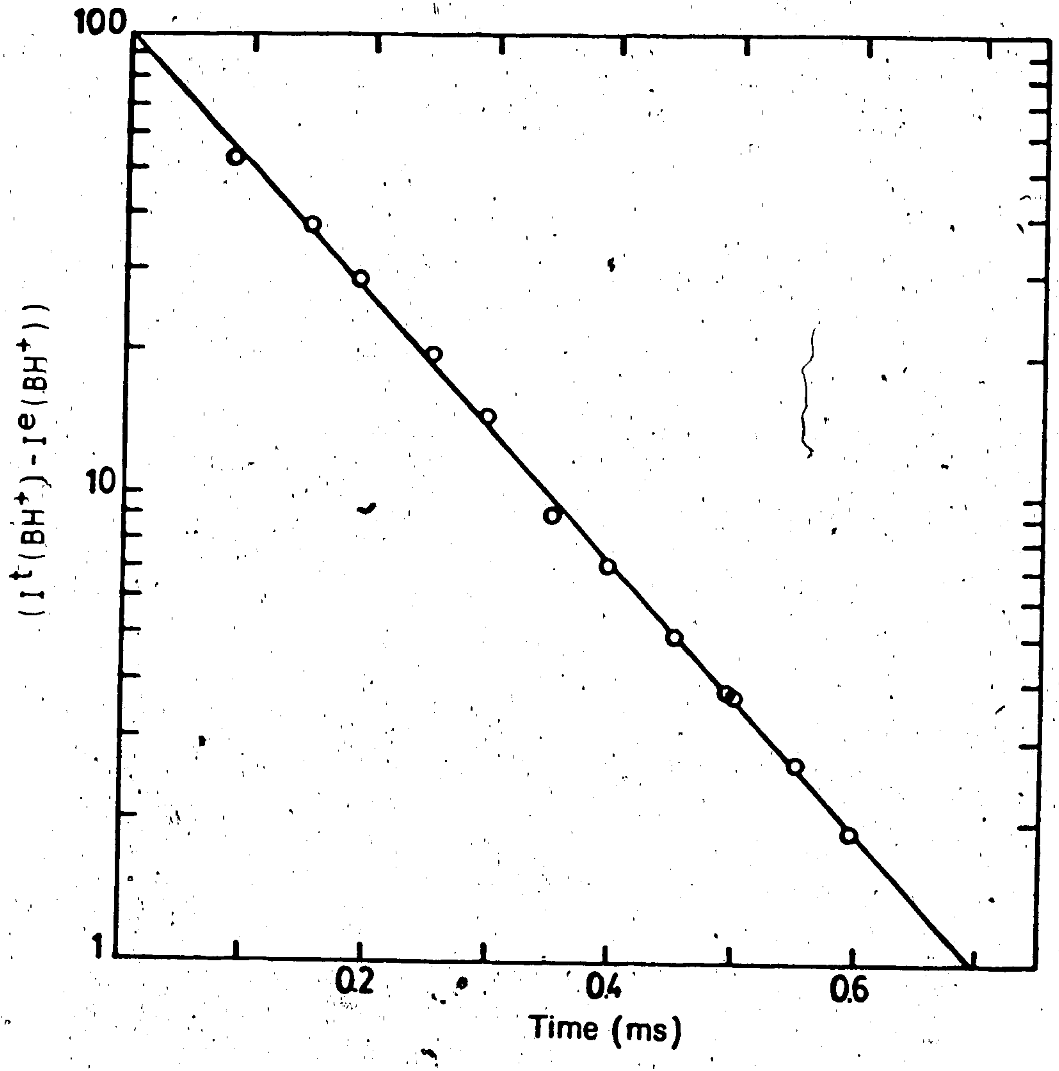

Figure 4.18. Logarithmic plot of normalized ion intensities of $(I^t(BH^+)-I^e(BH^+))$ vs. time for the data presented in Figure 4.17 where B = $C_6H_5COCH_3$. This plot leads to evaluation of ν_f for the reversible proton transfer reaction 4.2.

C. Method III Reference Base Dimerization and its Effect on the Rate Constant for the Protonation of Ferrocene. Analog Computer Analysis of Experimental Data.

This is the case where protonated base B undergoes dimerization (equation 4.34) apart from proton transfer to ferrocene (equation 4.1).

$$BH^+ + B \rightleftharpoons B_2H^+ \qquad 4.34$$

Dimerization reactions are in general third body dependent in the pressure range used with HPCI mass spectrometry and thus are considered slower than proton transfer reactions. Based on this general rule, it was thought that the rate of fonmation of B_2H^+ should have no effect on the rate constant of the proton transfer reaction 4.1, and in that case, k_F for the protonation reaction could be evaluated via method I. However, this assumption did not seem to apply with the acetophenone/ferrocene, acetone/ferrocene, and anisole/ferrocene systems because under certain ranges of concentration and temperature conditions the dimerization reaction associated with each of these reference bases appeared to be faster than the proton transfer reaction. This was first realized by inspection and analysis of the normalized time dependence profiles of all the major ions associated with a particular system, i.e. BH^+, B_2H^+, and $(C_5H_5)_2FeH^+$.

In order to investigate to what extent the dimerization reaction is affecting the forward rate of reaction 4.1, an analog computer analysis was applied to a set of data obtained from the acetone/ferrocene experiments (B:acetone). This system was chosen to illustrate this method, because the presence of the acetone dimer was most pronounced among all the systems studied at the temperature range used.

The computer was programmed to reproduce the normalized ion profiles of the ions which resulted from the reaction systems 4.27 and 4.34 (see Figure 4.19 solid lines), with each step being reversible and pseudo-first order for the given ferrocene pressure. The reaction frequencies ν_F, ν_R, ν_1, and ν_{-1} were treated as variable parameters, and were changed until a best fit of the experimental curves was obtained. Figure 4.19 (dashed lines) illustrates the type of fit that could be obtained.

Once the experimental curves had been reproduced, the variable parameter ν_1 was set to zero while all others were kept constant. This caused the elimination of the $((CH_3)_2CO)_2H^+$ ion profile from the normalized spectra and considerable changes in the $(CH_3)_2COH^+$ and $(C_5H_5)_2FeH^+$ ion profiles. The resulting time dependence spectra of these two ions represent the normalized ion intensities of reaction 4.27 in the absence of dimerization reaction, 4.34, and are shown in Figure 4.20

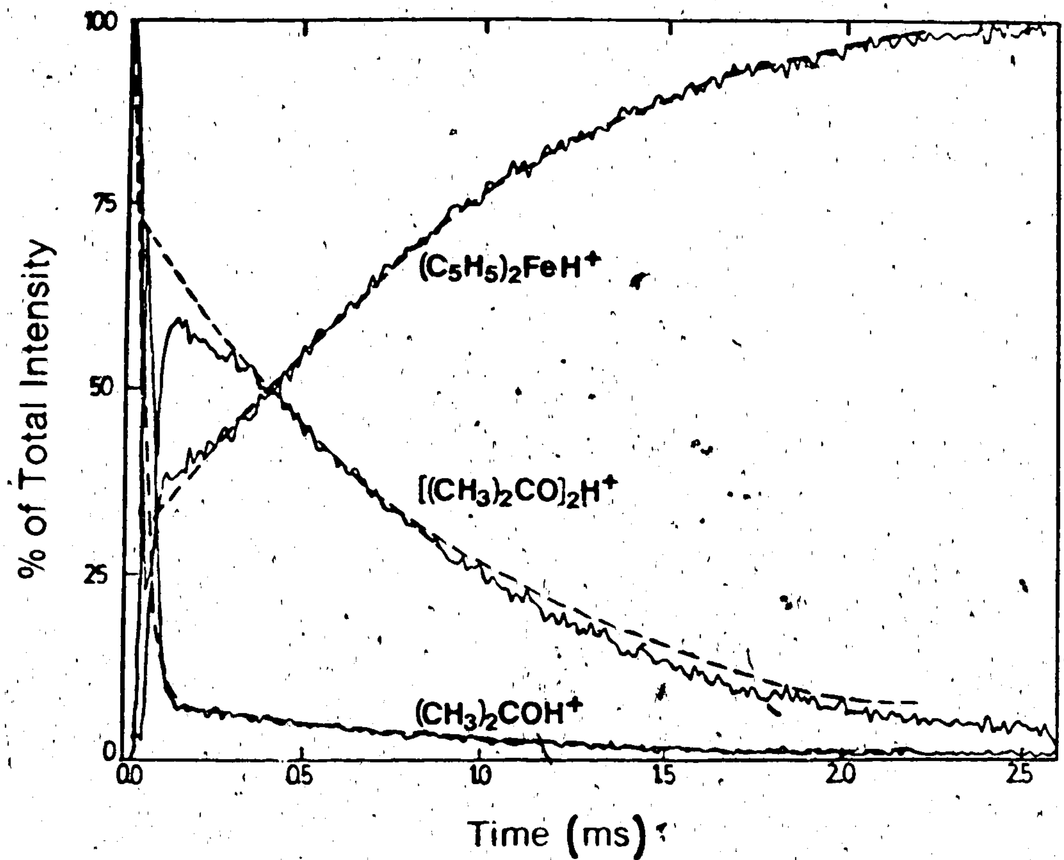

Figure 4.19. Time dependence of normalized ion intensities after the ionizing electron pulse resulting from the acetone/ferrocene system. Solid lines correspond to experimental observations ($P_{methane}$=5.2 Torr, $P_{acetone}$=4.54 mTorr, $P_{ferrocene}$=0.67 mTorr, Temperature=523 K), dashed lines correspond to analog computer fits, calculated on the basis of reaction systems 4.1 and 4.34 with B = acetone. The discrepancy between experimental and computer fit lines at times below 0.5 msec is due to initial concentrations of $(CH_3)_2CO]H^+$ and $(C_5H_5)_2FeH^+$ in the ion source, because an ion quench pulse was not applied at the end of each experiment.

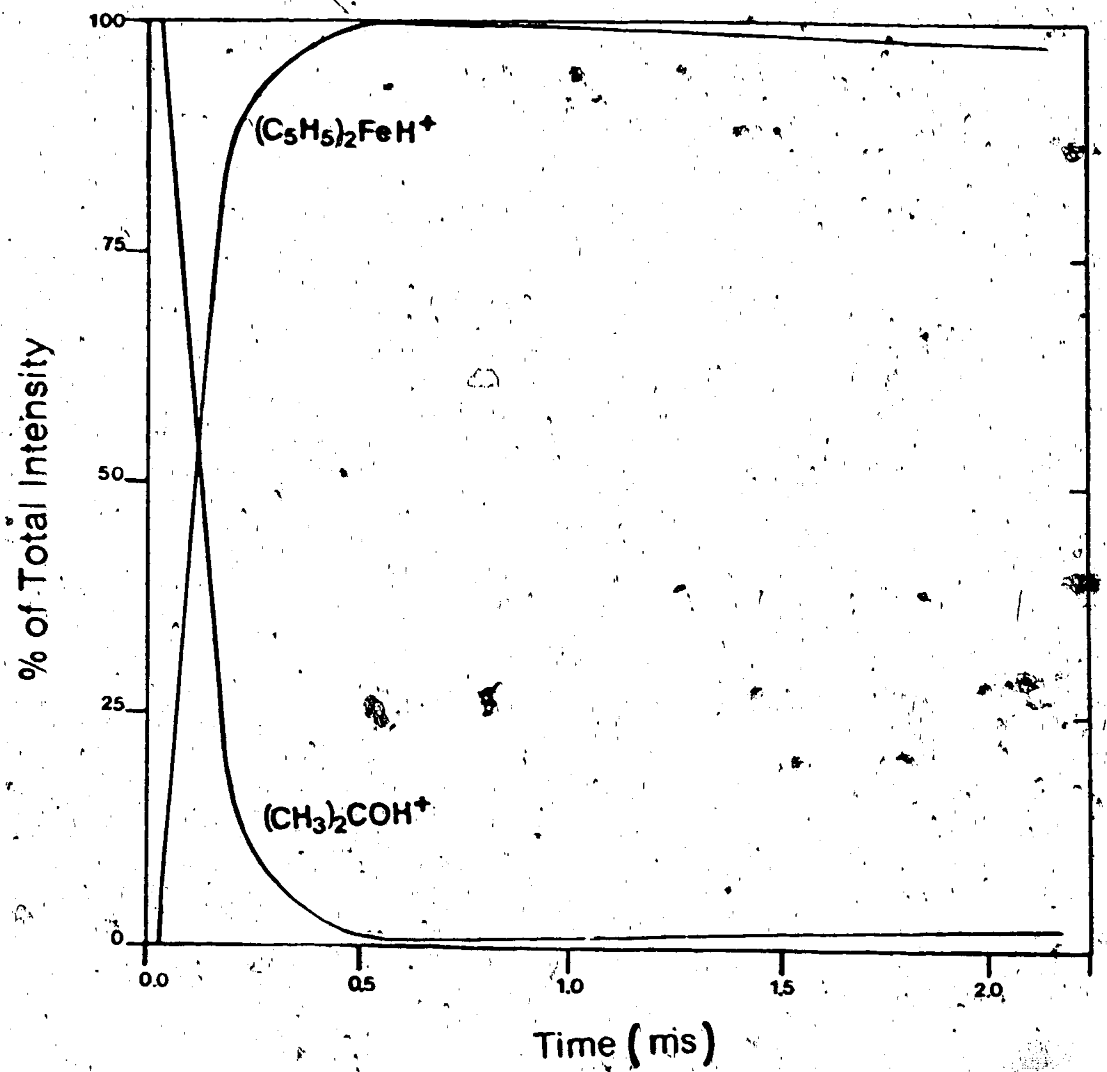

Figure 4.20. Time dependence of normalized ion intensities resulting from the data in Figure 4.19 when the acetone dimerization reaction was taken out of the overall reaction scheme, i.e. the programmable parameter corresponding to ν_1 at the analog computer analysis was set to zero.

Using the $(CH_3)_2COH^+$ time dependence ion intensity, reported in Figure 4.20, the reaction frequency (ν_F) for the reaction 4.27 was determined via the standard procedure (see method I). The resulting numerical value for ν_F was found to be 5-10 times greater than ν_F^{exp}. ν_F^{exp} represents the reaction frequency for reaction 4.27 when obtained through utilization of experimental $(CH_3)_2COH^+$ time dependence ion intensities (Figure 4.19) with all three ions $(CH_3)_2COH^+$, $[(CH_3)_2CO]_2H^+$, and $(C_5H_5)_2FeH^+$ being collected and normalized under the same experimental conditions.

A number of experimental data sets from the three systems mentioned above were computer analyzed and ν_F and ν_F^{exp} values for each set were obtained through this procedure. On the whole, there was a good agreement in the results obtained. ν_F values were always greater than ν_F^{exp} by a factor which seemed to vary, depending on the data set and system studied. It was empirically established that these two values can be linked together through equation 4.35.

$$\nu_F = \nu_F^{exp} \left(\frac{I^t(BH^+) + I^t(B_2H^+)}{I^t(BH^+)} \right), \text{ provided } I^t(B_2H^+) > I^t(BH^+) \qquad 4.35$$

where $I^t(BH^+)$ and $I^t(B_2H^+)$ are the normalized intensities of the protonated monomer and proton bound dimer of the reference base, respectively, at time, t, after the electron pulse.

This equation permitted evaluation of the reaction frequency ν_F by direct utilization of experimental data and without the need of computer fits. Agreement between ν_F values obtained via equation 4.35 and computer analyzed data established the reliability for applying equation 4.35 to all systems studied, where the protonated reference base formed proton bound dimers much faster than proton transfer to ferrocene. In the cases where the decay of the monomer was too fast (at low temperatures) the normalized dimer time dependence ion profile was used for evaluation of ν_F^{exp} providing that all ions BH^+, B_2H^+, and $(C_5H_5)_2FeH^+$ had been collected and normalized under identical experimental conditions. Rate constant values (k_F) were obtained via equation 4.35. The concentration of the neutral species was known.

The rate constants for the acetone/ferrocene system were determined by utilization of this method for the temperature range studied. They turned out to be close to Langevin-ADO rates with the expected (104) slight temperature dependence (see corresponding plot in Figure 4.16).

This method was also used to evaluate rate constants for the acetophenone/ferrocene and anisole/ferrocene systems, at temperatures between 430-500 K for the first, and below 355 K for the second, where the dimer formation of the corresponding reference bases was very strong.

D. Method IV Evaluation of k_F Leading to Protonation of Ferrocene Via K_{eq} and k_R.

This method was used to calculate the forward rate constant by utilizing the measurement of the equilibrium and the reverse rate constant for the reaction 4.1

$$BH^+ + (C_5H_5)_2Fe \underset{k_R}{\overset{k_F}{\rightleftharpoons}} (C_5H_5)_2FeH^+ + B \qquad 4.1$$

where $K_{eq} = k_F/k_R$ 4.36

The reverse rate constant for reaction 4.1 can be calculated using equation 4.37.

$$\frac{dI^t((C_5H_5)_2FeH^+)}{dt} = k_R I^t((C_5H_5)_2FeH^+) \times [B] \qquad 4.37$$

Here $I^t((C_5H_5)_2FeH^+)$ is the intensity of protonated ferrocene at time t. Since reaction 4.1 is pseudo-first order (see method I), it can be described by the pseudo-first order rate constant, ν_R, where

$$\nu_R = -k_R[B] . \qquad 4.38$$

Substitution of equation 4.38 into 4.37 followed by integration of the resulting relationship leads to equation 4.39.

$$\ln \frac{I^t((C_5H_5)_2FeH^+)}{I^o((C_5H_5)_2FeH^+)} = -\nu_R \cdot t \qquad 4.39$$

Then, the reaction frequency ν_R is obtained from the linear section of the semilogarithmic plot of the normalized $(C_5H_5)_2FeH^+$ intensity vs. time. Since the concentration of B was known k_R was calculated using equation 4.38.

In the cases where k_R and K_{eq} had been experimentally obtained at the same temperature, k_F was then calculated via equation 4.36.

This method was applied to evaluate the forward rate constant for the 3-ClPy/ferrocene system at 500 K and the acetophenone/ferrocene system at temperatures below 430 K. In the acetophenone/ferrocene case, even though the reverse process of equation 4.2 is endothermic, the reverse rate was boosted by using very large concentrations of acetophenone.

4.4.2 Discussion of Results. The Kinetics of Proton Transfer Reactions to Ferrocene.

The proton transfer rate constants for all bases, obtained from the plots in Figures 4.14, 4.15, at a reaction temperature of 500 K are plotted against the exothermicity of the reaction in Figure 4.21. It is seen in the figure that the majority of the reactions are indeed slow. There is also a clear correlation between exoergicity and rate constant for the ring protonated species. Only if the reaction is exoergic by more than ca 25 kcal mol^{-1} is the rate constant close to the collision limit. Similar

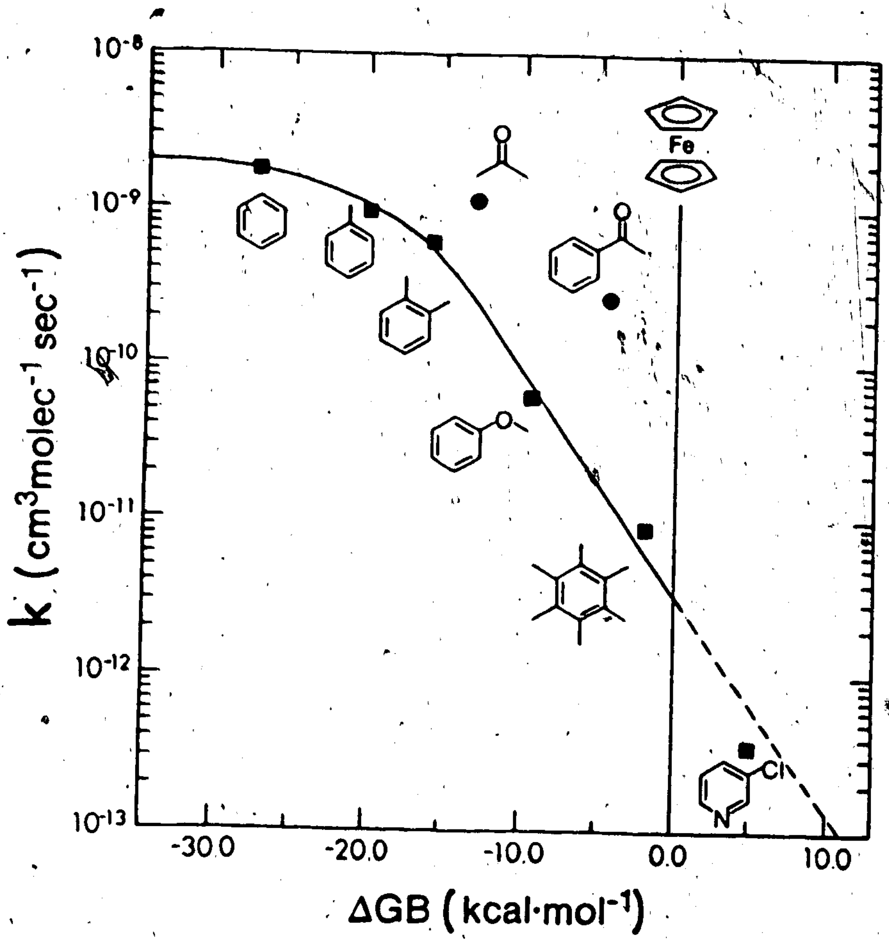

Figure 4.21. Rate constants of reactions:
$BH^+ + (C_5H_5)_2Fe \longrightarrow (C_5H_5)_2FeH^+ + B$, plotted against the difference in gas phase basicity, GB, between ferrocene and reference base B at 500 K. Compounds B are identified next to the points in the figure. The gas phase basicity of ferrocene is indicated by the vertical line. The rate constant for 3-Chloropyridine was calculated from the measured rate constant for the reverse reaction and the equilibrium constant.

relationships have earlier been established for the hydride transfer reactions (87).

The slow proton transfer to ferrocene could be due to an internal energy barrier. Some results from solution studies are relevant in this regard. Ferrocene has two proton acceptor sites, the metal atom (105, 96) and the cyclopentadiene rings (106, 107). It has been shown by NMR that in strongly acidic media ferrocene is protonated on the metal (96).

Beauchamp (88) has assumed that in the gas phase ferrocene is protonated on the Fe atom. It was pointed out, in the introduction to this chapter, that protonated ferrocene in solution is bent (91). Assuming that the protonation in the gas phase is at the Fe atom, the barrier to protonation could be sought in the geometry change on protonation, and the steric repulsions associated with the approach of the reagent ion BH^+ to ferrocene.

The results in Figure 4.21 show that there is a significant difference between the rate-exothermicity relationship between the oxygen protonated reagent ions BH^+ (B = acetone, acetophenone) and the ring protonated BH^+ (B = benzene, toluene, xylene, anisole, hexamethylbenzene), the rates for equal exothermicity being much slower for the ring protonated compounds.

The reaction coordinates associated with ion-molecule reactions are very different from those observed for reactions occurring in solution or those involving the reaction of two neutral molecules in the gas phase.

A typical (85) gas phase ion-molecule reaction coordinate is shown in Figure 4.22. Because of the attractive ion-polarizable molecular forces which act at long range, the potential energy decreases as the ion A^+ and molecule B approach. At closer range, more specific bonding between the ion and the molecule can lower the energy further and lead to a stable adduct $A^+.B$. For example, when A^+ is a protonated ion, such as protonated acetone, and B is an oxygen base, $A^+.B$ will be held by a strong hydrogen bond. The internal barrier, $E^‡$, is due to the energy change connected with the formation of the transition state. Typically, in gas phase ion-molecule reactions, the energy of the transition state lies much below the energy level of the reactants $A^+ + B$, see Figure 4.22. This situation leads to the high rates (collision rates) commonly observed for ion-molecule reactions. Thus, for proton transfer between two oxygen bases the barrier $E^‡$ is very low and proton transfer proceeds at collision rates, even at very low exothermicity (108). These fast rates are essential to CI analysis leading to the quasi molecular protonated ion of the analyte. Ion-molecule reactions for which the internal barrier, $E^‡$, is high, such that it protrudes above the energy level of the reactants are exceedingly slow and have rates that increase with increasing temperature (positive temperature dependence)

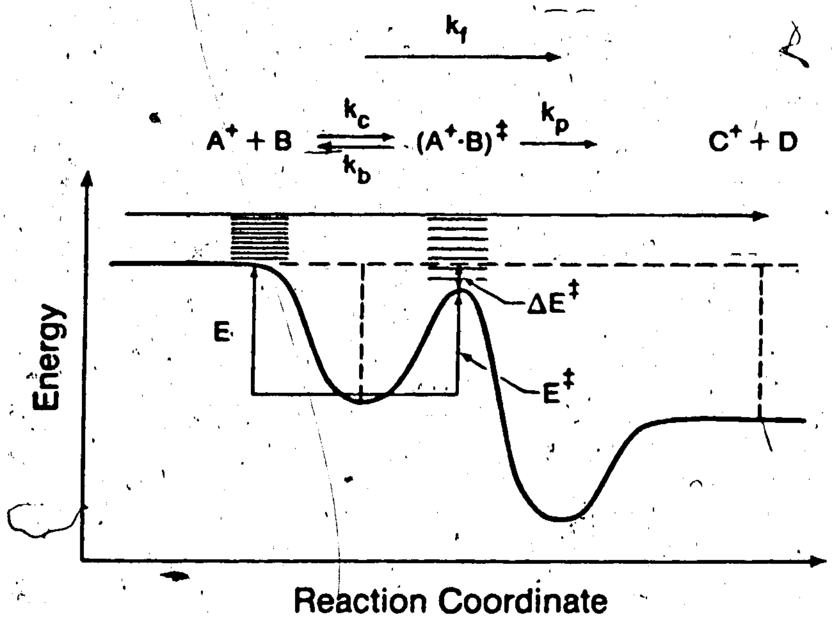

k_f
$A^+ + B \underset{k_b}{\overset{k_c}{\rightleftharpoons}} (A^+ \cdot B)^\ddagger \xrightarrow{k_p} C^+ + D$
E
$\Delta E^\ddagger$
$E^\ddagger$
Energy
Reaction Coordinate

Figure 4.22. Reaction energy coordinate diagram for slow ion molecule reactions with negative temperature dependence. The orbiting transition state occurring over E and $E^\ddagger$ are loose transition states. The product forming transition state $(A^+.B)^\ddagger$ is a tight state.

(109), i.e. they show the conventional temperature dependence observed in "normal" chemical reactions.

The temperature dependence of the present proton transfer reactions was determined, see Figure 4.16. The fast reaction involving protonated acetone, which proceeds at collision rates, has no temperature dependence. This is typical for reactions with a very small internal barrier (85, 109). The other reactions, B = xylene, anisole, and hexamethylbenzene, which are progressively slower have rate constants that decrease as the temperature is increased (negative temperature dependence). Such a behaviour has been observed before (83, 84, 109). For such reactions, it has been assumed (85, 109) that the barrier is fairly high, but still lies below the energy level of the reactants $A^+ + B$. The reactions will be slow even though there is no positive energy barrier above the level of the reactants, if there is a positive free energy barrier, which for the case considered, means an entropy of the transition state $(AB^+)^\ddagger$ that is very unfavorable (85). Such a transition state is called a "tight" complex. The most common cause for "tightness" is loss of rotation in the transition state of otherwise freely rotating groups (85, 109).

Negative temperature dependence and increase of rate with increasing exothermicity in a related reaction series has been observed for such reactions (87, 109).

The slow rates observed for the proton transfer to ferrocene, the negative temperature dependence, and the dependence on the exothermicity, Figure 4.16 and 4.21, could be explained by the same model. While proton transfer generally does not involve a high energy barrier (108) (oxygen and nitrogen bases in the transition state) proton transfer to ferrocene could be different. The presence of the two cyclopentadiene groups, which tilt on protonation might be one factor leading to a larger barrier. Another factor could be the type of bonding in the $A^+.B$ complex, i.e. $BH^+(C_5H_5)_2Fe$ complex formed. Weak bonding in the complex will lead to a high lying top of the transition state $(B...H...(C_5H_5)_2Fe^+)^{\ddagger}$ relative to the energy level of the reactants, even in the presence of a modest barrier, i.e. even in the presence of a modest increase of energy between $BH^+.(C_5H_5)_2Fe$ and $(B...H...(C_5H_5)_2Fe^+)^{\ddagger}$, see Figure 4.22.

Weak bonding in $BH^+.(C_5H_5)_2Fe$ is expected when the charge in BH^+ is not concentrated on the proton but is delocalized over B. This is exactly the case for the ring protonated BH^+ (benzene and substituted benzenes), see resonance structures for the protonated benzene shown below.

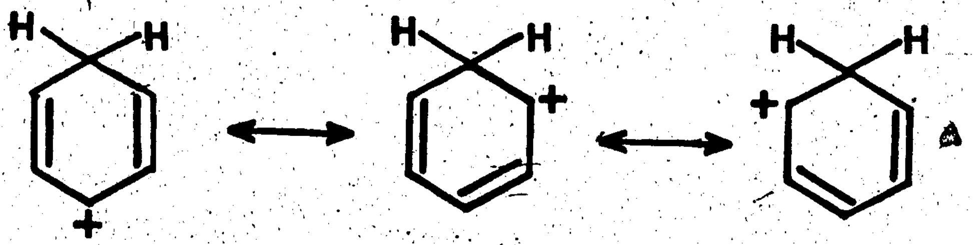

These reagent ions were found to lead to significantly lower rates than the oxygen protonated reagents at equal exothermicity, for proton transfer, see Figure 4.21. This is in line with the expected weaker bonding of these reagent ions $BH^+.(C_5H_5)_2Fe$, relative to that for the oxygen acids BH^+, in which most of the charge is located on the oxygen.

The tightness of the complex, required by the model, could result from loss of rotation in the transition state caused by the bulky cyclopentadiene and B groups.

The change from negative to positive temperature dependence found for B protonated acetophenone at 420 K, see Figure 4.16, is unusual. The negative temperature dependence below 420 K is similar to that observed for the three bases in Figure 4.16. The larger slope observed for acetophenone may not be significant, considering the large scatter of the data. Curved Arrhenius plots have been observed, also, in other ion-molecule reactions (109). While such curved plots are not unexpected on the basis of theory (109), the interpretation is too involved and uncertain, and will not be considered here.

Reagent ions, like the protonated benzenes, are seldom used in routine CI measurements and the finding that such reagent ions may lead to unusually low sensitivities for the detection of ferrocene, may be considered of no analytical significance. However, this is not the case.

Recent results from APCI experiments with ferrocene in this laboratory, using a TAGA triple quadrupole mass spectrometer, have shown that the sensitivity for detection of ferrocene is very low in the APCI mass spectra, when compared to that for nitrogen bases of similar gas phase basicity. This result can be interpreted at least in part on the basis of the present findings.

The major reagent ions in the TAGA are protonated water clusters $H_3O^+(H_2O)_n$. The positive charge in these clusters is quite delocalized over the various water molecules and one expects the energy lowering of formation of the $(H_2O)_nH_3O^+$:Fe adduct to be quite small. This situation is similar to that observed above for the charge delocalized protonated benzenes which led to low protonation rates for ferrocene. The low sensitivity for protonation of ferrocene in the TAGA is thus in line with the insights provided by the present study.

REFERENCES

1. Munson, M.S.B.; Field, F.H. J. Am. Chem. Soc. 1966,88,2621.
2. Munson, M.S.B.; Field, F.H. J. Am. Chem Soc. 1966, 88, 4337.
3. Field, F.H.; Munson, M.S.B.; Becked, D.A. Advan. Chem Ser. 1966, 58, 167.
4. Munson, M.S.B.; Field, F.H. J. Am. Chem. Soc. 1967, 89, 1047.
5. Field, F.H.; Munson, M.S.B. ibid., p 4272.
6. Field, F.H.; "Advances in Mass Spectrometry"; Kendrick, E., Ed.; Institute of Petroleum: London, 1968.
7. Field, F.H. J. Am. Chem. Soc. 1969, 91, 2827.
8. Munson, B. Anal. Chem. 1971, 43, 28A.
9. Harrison, A.G. "Chemical Ionization Mass Spectrometry"; CRC Press, Inc.: Boca Raton, Florida, 1983.
10. Beggs, D.; Vestal, M.L.; Fales, H.M.; Milne, G.W.A. Rev. Scient. Instr., 1971, 42, 1578.
11. Meot-Ner (Mautner), M. In "Gas Phase Chemistry"; Bowers, M.T., Ed.; Academic Press: New York, 1979; Vol. 1, p197.
12. Burlingame, A.L.; Kimble, B.J.; Derrick, J.P. Anal. Chem. 1976, 48, 368R.

13. Burlingame, A.L.; Shackleton, C.H.L.; Howe, I.; Chizhov, O.S. Anal. Chem. 1978, 50, 346R.
14. Jennings, K.R. In "Gas Phase Ion Chemistry"; Bowers, M.T., Ed.; Academic Press: New York, 1979, Vol. 2, p 123.
15. Hunt, D.F.; Sethe, S.K. In "High Performance Mass Spectrometry: Chemical Applications"; Gross, M.L., Ed.; ASC Symp. Series 70, ASC: Washington, D.C., 1978, p 150.
16. Burlingame, A.L.; Baillie, T.A.; Derrick, P.J.; Chizhov, O.S. Anal. Chem. 1980, 52, 215R.
17. Field, F.H.; Munson, M.S.B. J. Am. Chem. Soc., 1965, 87, 3289.
18. Stevenson, D.P.; Schissler, D.O. J. Chem. Phys. 1955, 23, 1353.
19. Stevenson, D.P.; Schissler, D.O. J. Chem. Phys. 1958, 29, 282.
20. Talrose, V.L.; Lyubimova, A.K. Dolk. Acad. Nauk SSSR 1951, 86(5), 209.
21. Field, F.H.; Lampe, F.W. J. Am. Chem Soc. 1956, 78, 5697.
22. Field, F.H.; Franklin, J.L.; Lampe, F.W. J. Am. Chem. Soc. 1957, 79, 6132.
23. Lias, S.G.; Liebman, T.F.; Levin, R.D. Phys. Chem. Ref. Data 1984, 13, p 695-808.
24. Cunningham, A.J.; Payzant, J.D.; Kebarle, P. J. Am. Chem. Soc. 1972, 94, 7627.

25. Dunkin, F.C.; Feshenfeld, F.C.; Schmeltekopf, A.L.; Ferguson, E.E. J. Chem. Phys. 1968, 49, 1365. Feschenfeld, F.C. Int. J. Mass Spectrom. Ion Phys. 1975, 16, 151.

26. Bohme, D.K. In "Interactions Between Ions and Molecules"; Ansloos, P., Ed.; Plenum: New York, 1975, p 489.

27. Bowers, M.T.; Aue, D.H.; Webb, H.M.; McIver, R.T. J. Am. Chem Soc. 1971, 93, 4314.

28. Camisarow, M.B.; Marshall, A.G. Chem. Phys. Lett. 1974, 25, 282.

29. Searls, S.K.; Kebarle, P. Can. J. Chem. 1969, 47, 2620.

30. Dzidic, I.; Kebarle, P. J. Phys. Chem. 1970, 74, 1466.

31. Davidson, W.R.; Kebarle, P. J. Am. Chem. Soc. 1976, 98, 6125.

32. Solomon, J.J.; Field, F.H. J. Am. Chem. Soc. 1975, 97, 2625.

33. Meot-Ner, M.; Field, F.H. J. Chem. Phys. 1976, 64, 277.

34. Tang, I.N.; Castleman, A.W. J. Chem. Phys. 1972, 57, 3638.

35. Reed, R.I. In "Mass Spectrometry"; Reed, R.I., Ed.; Academic Press: London, 1965, p 401.

36. Hogg, A.M. Anal. Chem. 1972, 44, 227.

37. Baldwin, M.A.; McLafferty, F.W. Org. Mass Spectrom. 1973, 7, 1353.

38. Ohashi, M.; Tsujimoto, K.; Yasuda, A. Chem. Lett. (Japan), 1976, 439.

39. Hunt, D.F.; Shabanowitz, J.; Botz, F.K.; Brent, D.A. Anal. Chem. 1977, 1160, 49.

40. Hansen, G.; Munson, B. Anal. Chem. 1978, 50, 1130.

41. Cotter, R.J. Anal. Chem. 1979, 51, 317.

42. Thenof, J.P.; Nowlin, J.; Carroll, D.I.; Montgomery, F.E.; Horning, E.C. Anal. Chem. 1979, 51, 1101.

43. Cotter, R.J. Anal. Chem. 1980, 52, 1589A.

44. Jamieson, G.C.; Reuter, C.C., Fitch, W.L. Anal. Chem. 1985, 57, 121.

45. Strausz, O.P.; Barton, S.C.; Duholke, W.K.; Gunning, H.E.; Kebarle, P. Can. J. Chem. 1971, 49, 2048.

46. Dushman, S. "Scientific Foundations of Vacuum Technique"; John Wiley and Sons, Inc.: New York, 1958.

47. Kebarle, P. "Interactions Between Ions and Molecules"; P. Ausloos, Ed.; Plenum Press: New York, 1975.

48. Durden, D.A. Ph.D. Thesis, Department of Chemistry, University of Alberta, Edmonton, Alberta, 1968.

49. Beynon, J.H. "Mass Spectrometry ans its Applications to Organic Chemistry"; Elsevier Publishing Company: New York, 1960.

50. "Handbook of Chemistry and Physics"; 54th ed.; Chemical Rubber Company Press: 1973.

51. Penning, F.M. "Electrical Discharges in Gases"; Macmillan: New York, 1957.

52. Futrell, J.H. Rev. Scien. Instr. 1971, 42, 244. And references within.

53. Beggs, D.; Vestal, M.L.; Fales, H.M.; Milne, G.W.A. Rev. Scien. Instr. 1971, 42, 1578.

54. Arshadi, M.R. Ph.D. Thesis, Department of Chemistry, University of Alberta, Edmonton, Alberta, 1969.

55. Collins, J.G. Ph.D. Thesis, Department of Chemistry, University of Alberta, Edmonton, Alberta, 1966.

56. McDowell, C.A. "Mass Spectrometry"; McGraw-Hill: New York, 1963, p 11.

57. Hogg, A.M. "A Digital Mass Readout for Magnetic Sector Mass Spectrometers". Paper presented at the 23rd Annual Conference on Mass Spectrometry and Allied Topics, Houston, TX, 1975.

58. Bell, J.; Chung, J.L.; Gavnett, ~~T.~~K. Gregor; Guilhaus, M. J. Phys. E. Sci. Instrum. 1979, 12, 683.

59. Freeman, J.P.; Mitchum, R.K. In "32nd Annual Conference on Mass Spectrometry and Allied Topics, San Antonio, TX"; ASMS, Ed.; East Lansing, MI, 1984, p 669.

60. Potter, W.E.; Mauersberger, K. Rev. Sci. Instrum. 1972, 43, 1327.

61. Stanton, H.E.; Chupka, W.A.; Ingrham, M.G. Rev. Sci. Instrum. 1956, 27, 109.

62. Walker, G.W.; Klettke, B.D.; Graves, P.W. Rev. Sci. Instrm. 1970, 41, 724.

63. McDaniel, E.W. "Collision Phenomena in Ionized Gases"; John Wiley and Sons: New York, 1964.

64. Lau, Y.K. Ph.D. Thesis, Department of Chemistry, University of Alberta, Edmonton, Alberta, 1979.

65. Kebarle, P. Ann. Rev. Phys. Chem. 1977, 28, 445.

66. Durden, D.A.; Kebarle, P.; Good, A. J. Chem. Phys. 1969, 50, 805.

67. Payzant, J.D. Ph.D. Thesis, Department of Chemistry, University of Alberta, Edmonton, Alberta, 1973, p 45.

68. Searls, S.K.; Kebarle, P. J. Phys. Chem. 1968, 72, 742.

69. Hogg, A.M.; Haynes, R.M.; Kebarle, P. J. Am. Chem Soc. 1966, 88, 28.

70. Hogg, A.M.; Kebarle, P. J. Chem Phys. 1965, 43, 449.

71. French, M.A. Ph.D. Thesis, Department of Chemistry, University of Alberta, Edmonton, Alberta, 1979.

72. Kebarle, P.; Searls, S.K.; Zolla, A.; Scarborough, J.; Arshadi, M. J. Am. Chem. Soc. 1967, 89, 6393.

73. Cunningham, A.J.; Payzant, J.D.; Kebarle, P. J. Am. Chem. Soc. 1972, 94, 7627.

74. Good, A.; Durden, D.A.; Kebarle, P. J. Chem. Phys. 1970, 52, 222.

75. Meot-Ner, M.; Field, F.H. J. Am. Chem Soc. 1977, 99, 998. Field, F.H. ibid. 1969, 91, 2827.

76. Young, C.D.; Edelson, D.; Falconer, W.E. J. Chem. Phys. 1970, 53, 4295.

77. Lau, Y.K.; Ikuta, S.; Kebarle, P. J. Am. Chem. Soc. 1982, 104, 1462.

78. Greenstein, J.P.; Winilz, M. "Chemistry of Amino Acids"; Wiley: New York, 1961, Vol. 1.

79. Hogg, A.M.; Nagabhushan, T.L. Tetrahedron Lett. 1972, 47, 4827.

80. Meot-Ner (Mautner), M.; Hunter, E.P.; Field, F.H. J. Am. Chem. Soc. 1979, 101, 686.

81. Locke, M.J.; Hunter, R.L.; McIver, R.T., Jr. J. Am. Chem. Soc. 1979, 101, 272.

82. Locke, M.J.; McIver, R.T., Jr. J. Am. Chem. Soc. 1983, 105, 4226.

83. Magnera, T.F.; Kebarle, P. In "Ionic Processes in the Gas Phase"; Ferreira, A. Ed.; Reidel Publishing Co.: Dortrecht, 1984, p 135.

84. Brauman, J.I. In "Kinetics of Ion Molecule Reactions"; Ausloos, P., Ed.; Plenum Press: New York, 1979.

85. Farneth, W.E.; Brauman, J.I. J. Am. Chem. Soc. 1976, 98, 7891.

86. Jasinski, J.M.; Brauman, J.I. J. Am. Chem. Soc. 1980, 102, 2906.

87. Meot-Ner, M.; Field, F.H. J. Am. Chem. Soc. 1978, 100, 1356.

88. Foster, M.S.; Beauchamp, J.L. J. Am. Chem. Soc. 1975, 97, 4814.

89. Corderman, R.R.; Beauchamp, J.L. Inorg. Chem. 1976, 15, 665.

90. Eyler, J.R.; Richardson, D.E. J. Am. Chem. Soc. 1985, 107, 6130.

91. Pavli'k, I.; Subrt, J. Collec. Czech. Chem. Comman. 1967, 32, 76.

92. Grimsrud, E.P.; Chowdury, S.; Kebarle, P. J. Chem. Phys. 1985, 83, 1059.

93. Andrews, J.T.S.; Westrum, E.F. Jr. J. Organomet. Chem. 1969, 17, 349.

94. (a) Wagnam, D.D.; Evans, W.H.; Parker, V.B.; Schumm, R.H.; Halow, I.; Bailey, S.M.; Churney, K.L.; Nuttall, R.L. J. Phys. Chem. Ref. Data 1982, 11, Suppl. 2. (b) Rosenstock, H.M.; Draxl, K.; Steiner, B.W.; Herron, J.T. J. Phys. Chem. Ref. Data 1977, 6, Suppl. 1. All thermochemical data obtained from Lias (Reference #23) were increased by 1.48 Kcal mol^{-1} (electron convention) in order to achieve consistancy with the other two thermochemical data compilations.

95. Rushbrooke, G.S. "Introduction to Statistical Mechanics"; Clarenton Press: Oxford, 1967, p 48.

96. Curphey, T.J.; Santer, J.O.; Rosenblum, M.; Richards, J.H. J. Am. Chem. Soc. 1960, 82, 5249.

97. Lippincott, E.R.; Nelson, R.D. J. Am. Chem. Soc. 1955, 77, 4990.

99. Ogasahara, K.; Sorai, M.; Suga, H. Mol. Cryst. Liq. Cryst. 1981, 71, 189.

98. Edwards, J.W.; Kington, G.L. Trans. Faraday Soc. 1962, 58, 1334.

100. Su, T.;Bowers, M.D. In "Gas Phase Ion Chemistry"; Bowers, M.D., Ed.; Academic Press: New York, 1971, Vol. 1.

101. Lau, K.Y.; Kebarle, P. J. Am. Chem. Soc. 1976, 98, 7452.

102. Benson, S.W. "The Fundamentals of Chemical Kinetics"; McGraw-Hill: New York, 1960, p 14-17.

103. Hammes, G.G. "Principles of Chemical Kinetics"; Academic Press: New York, 1978, p 9.

104. Su, T.; Bowers, M.T. Int. J. Mass Spectrom. Ion Phys. 1075, 17, 211.

105. Bitterwolf, T.E.; Ling, A.C. J. Organomet. Chem. 1972, 40, 197.

106. Floris, B.; Illuminati, G. Ortaggi, G. Tetrahedron Lett. 1972, 269.

107. Cericelli, G,; Illuminati, G. Ortaggi, G.; Guiliani, A.M. J. Organomet. Chem. 1977, 127, 357.

108. Bohme, D.K. In "Interactions Between Ions and Molecules"; Ausloos, P., Ed.; Plenium Press: New York, 1979, p 489-504.

109. Sen Sharma, D.K.; Kebarle, P. J. Am. Chem. Soc. 1982, 104, 19.